Quantifying and modeling methane emissions from the North Sea region with ICON-ART

Zur Erlangung des akademischen Grades eines

DOKTORS DER NATURWISSENSCHAFTEN (Dr. rer. nat.)

von der KIT-Fakultät für Physik des
Karlsruher Instituts für Technologie (KIT)

genehmigte

DISSERTATION

von

Christian Scharun
aus Bruchsal

Referent: Prof. Dr. Peter Braesicke

Korreferentin: Prof. Dr. Corinna Hoose

Tag der mündlichen Prüfung: 17.12.2021

Abstract

The release of greenhouse gases (GHG) like methane (CH_4) plays a key role in driving the climate change. With the optimization of atmospheric chemistry climate models, the accuracy in predicting future scenarios is improved, which is an important factor in our efforts to mitigate climate change.

The objective of this work is to introduce three methods for the quantification and adjustment of wrong or missing emissions in well-established GHG-inventories, which are used as input data for emissions in atmospheric chemistry transport or climate models. Beside a straight-forward upscaling method and a regridding method based on reported emission data, we present the WALLACE workflow, a new and efficient method to quantify GHG emissions based on satellite measurements. The overall goal of WALLACE is to highlight emission hotspots and it therefore includes spatiotemporal proxy data and a selection algorithm. For the North Sea as a show case region we apply WALLACE to quantify methane emission fluxes of oil and gas platforms.

The adjusted emissions are implemented as pointsources into the ICOsahedral Nonhydrostatic model with Aerosols and Reactive Trace gases (ICON-ART) and idealized simulations are performed to compare the three methods with reference simulations to derive their impact on the spatial distribution of methane and its global and regional budget. For all three adjustment methods our model reveals a distribution of methane on the northern hemisphere and an effect on the European continent. For a quantification of the impact we evaluate the influence of the adjusted North Sea platform emissions on the radiative forcing. Additionally, we take a look at the anti-correlation between methane and its main sink in the atmosphere, the hydroxyl radical (OH), which is implemented as a simple OH-chemistry mechanism into the routines of the model.

This work makes a new and innovative contribution to achieve an accurate quantification of environmentally harmful gases that drive man-made climate change.

Contents

1 Introduction

The latest report of the Intergrovernmental Panel on Climate Change (IPCC) emphatically clarifies, that the human influence on climate, especially the increase of greenhouse gas (GHG) emissions from anthropogenic sources, lead to global warming (IPCC, 2021). Methane (CH_4) causes about 20% of the pre-industrial global warming induced by GHGs with a warming potential even higher than carbon dioxide (CO_2) (Kirschke et al., 2013; Saunois et al., 2016a). The existence of CH_4 in the Earth's atmosphere has been proved in the 1940's (Migeotte, 1948) and it was listed under „non-variable components of atmospheric air" by Glueckauf (1951). As we know today, atmospheric methane is highly variable and determined by various sources and sinks that balance its global budget (Saunois et al., 2016b). Methane sources are e.g. the usage and production of fossil fuels, biomass burning or agriculture and waste management (GCP, 2016). About 90% of the atmospheric methane is depleted by its reaction with the hydroxyl radical which makes OH the main sink of tropospheric CH_4 (Kirschke et al., 2013). Although most of the sources and sinks have been specified in the past three decades, their relative contributions to the global budget are extremely uncertain (Dlugokencky et al., 2011; Kirschke et al., 2013). For those reasons the investigation and study of global methane emissions is becoming more and more important for a mitigation of global climate change in the future.

With the Kyoto Protocol, the international community of nations committed itself to reduce GHG emissions with the overall aim of protecting the global climate. Therefore every country is obliged to report its annual amount of GHG emissions to the United Nations (UN), resulting in national reports, which are the basis of well-established emission inventories like the Emission Database for Global Atmospheric Research (EDGAR) (e.g. Janssens-Maenhout et al., 2019). The expert council on climate issues in Germany draws the conclusion, that a minority of the data is based on real measurements, most of them being still provisional. A much larger proportion is based on estimates from different institutions with various additional assumptions that have to be taken (Expertenrat für

Klimafragen, 2021). This inevitably leads to systematic errors and uncertainties in the creation of inventories like EDGAR.

Atmospheric models with idealized experimental setups like ICON-ART (ICOsahedral Non-hydrostatic model - Aerosols and Reactive Trace gases, Zängl et al. (2015); Rieger et al. (2015)) offer the possibility to investigate the impact of GHG emissions on global and regional budgets. By awarding the 2021 Nobel Prize in Physics to the German Klaus Hasselmann and the Japanese Syukuro Manabe "for the physical modelling of Earth's climate, quantifying variability and reliably predicting global warming" (The Nobel Prize, 2021), the importance of climate research and atmospheric modeling in particular has been emphasized.

This work focuses on the development of methods for the adjustment of missing trace gas emissions in atmospheric inventories. Within this context the evaluation of hotspots in datasets of atmospheric model and measurement data is an important issue for the quantification of emission sources on regional scales. This has been shown by Liu et al. (2021) by a new divergence method to estimate methane emissions from observations of the TROPOspheric Monitoring Instrument (TROPOMI). For similar aims van Damme et al. (2018) use a nine year set average of ammonia data from the Infrared Atmospheric Sounding Interferometer (IASI) and Tu et al. (2021) uses a one year set of cloud-free methane total column data also delivered by TROPOMI. Furthermore, a subsampling of the data for sufficient quality could lead to small datasets that are not suited for an in depth evaluation. In addition, background noise in datasets of atmospheric trace gases is a big problem. Within this work we develop a new approach to decrease the background noise on the one hand and to avoid the loss of data on the other.

The show case area for this work is the North Sea which belongs to the Atlantic Ocean and is located in northern Europe surrounded by Denmark, Germany, the Netherlands, Norway and the United Kingdom. For this study we define the North Sea Region (NSR) as the area from 52° - 62° N and 0° - 8° E to taking a closer look on methane emissions from offshore oil and gas platforms. This definition of the NSR excludes most of the surrounding land surface for two main reasons. First, all the platforms are offshore and therefore the sea surface is more of a source region with local enhancements than the surrounding land. Second, land surface means generally higher anthropogenic emissions. If we would include these into our NSR definition, this would lead to inconsistent and distorted results due to the mathematical construction of the methods that are developed within this work.

In Chapter 2 we will focus on the theoretical background, explaining the climate system and the sources and sinks of methane that contribute to its global budget. Additionally, we will introduce the reporting guidelines of atmospheric emission inventories and present the dataset EDGAR, which constitutes an important part of this work. Following in Chapter 3 we introduce the atmospheric model ICON-ART. We will focus on modules of ICON-ART that are important for this work, like the emissions and the pointsource module, and the simple OH chemistry mechanism that has been implemented into the model. The three methods for the adjustment of emissions are presented in Chapter 4, including a straight-forward up-scaling method and the processing of a new gridded emission product. Finally, the workflow package WALLACE is introduced, a new and efficient method to quantify GHG emissions based on measurements from the Sentinel-5P satellite and the TROPOMI instrument. Within Chapter 5 simulations with adjusted emissions are compared to reference simulations and their impact on the global and regional methane budget is evaluated. Furthermore, we compare our results to spatially higher resolved simulations and take a look at the influence of GHG emissions on radiative forcing. Additionally, we provide an analysis of the computing time and the sustainability of this work and climate modeling in general. In Chapter 6 we draw a conclusion from the results of this work and discuss further activities and applications.

2 Theoretical Background

2.1 The climate system

The Sixth Assessment Report (AR6) of the Intergovernmental Panel on Climate Change (IPCC) was released in August 2021. Its message is clear: "It is unequivocal that human influence has warmed the atmosphere, ocean and land. (...) Human-induced climate change is already affecting many weather and climate extremes in every region across the globe" (IPCC, 2021). Both, weather and climate, have a significant influence on our life on Earth and for a better understanding of atmospheric states, we need to learn more about the climate system and the processes that cause climate change (Baede et al., 2001). While *weather* is more about the current state of temperature, wind, precipitation or clouds around us, *climate* is defined as a long term mean of the weather and its variability over a time-span of at least 30 years in a certain area (Buchal and Schönwiese, 2016). The main climate factors are solar radiation, the influence of oceans, ice areas, land masses, mountains and volcanoes, but also the role of plants and animals. This leads us to the definition of the climate system as a complex structure that consists of five components: The atmosphere, the biosphere, the cryosphere, the hydrosphere and the land surface (Baede et al., 2001; Buchal and Schönwiese, 2016). The latter plays an important role because vegetation and soils on the land surface control how solar energy is "returned" to the atmosphere. The hydrosphere contains all liquid surface and subterrain water on Earth, which is about 70 % of its surface. The Cryosphere includes sea ice, the ice sheets of Greenland and Antarctica such as continental glaciers, snow fields and permafrost. Due to its high albedo the cryosphere is very important for the climate system when it comes to interactions with solar radiation. The biosphere represents the area where marine and terrestrial life on Earth occurs. The remaining component of the climate system on which we want to focus in this work is the atmosphere. All components of the climate system interact with each other in physical, chemical and biological processes,

e.g. the biosphere has an impact on the carbon dioxide concentration in the atmosphere due to photosynthesis and respiration (Baede et al., 2001). Numerous other processes on different scales like the hydrolocial cycle, global circulation and also human influences contribute to the interactions between the components of the climate system (Roedel, 1992). A schematic overview of the components of the global climate system is displayed in Figure 2.1.
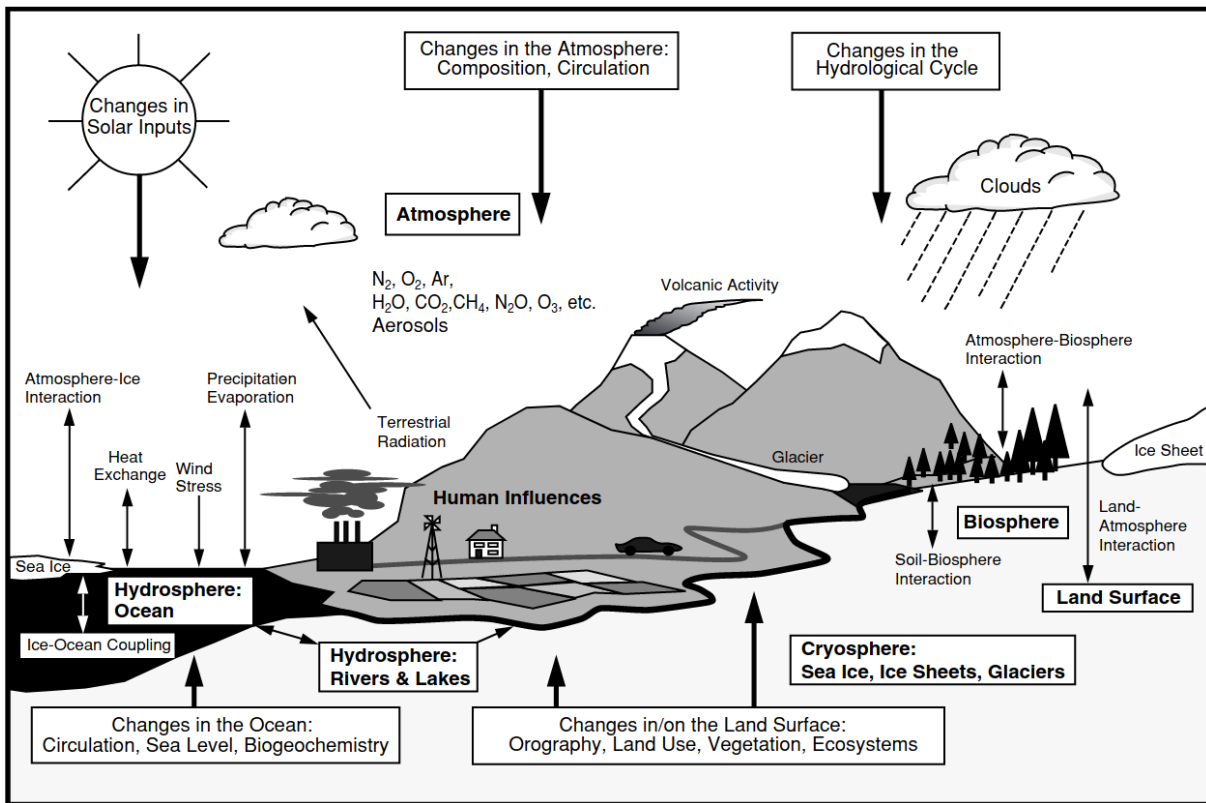

Figure 2.1: Schematic view of the components of the global climate system (bold), their processes and interactions (thin arrows) and some aspects that may change (bold arrows). The Figure is taken from Baede et al. (2001).

The atmosphere is an important safety shield for our Earth and reaches from the land surface up to a continuous upper boundary at about 1000 km height (Schönwiese, 2020). As air density and pressure are extremely low in these altitudes, only the lower atmosphere (below 100 km) is relevant for meteorological processes. For example within a height of 5.5 km air pressure decreased to 50 % and to 1 % in 30 km compared to the surface of the Earth (Schönwiese, 2020). The temperature reaches its maximum more or less directly at the surface of the Earth and decreases with altitude to about -55 °C in the Upper Troposphere Lower Stratosphere (UTLS) region at a height of about 10 km. This is followed by the stratosphere where temperature is at least more or less constant but then rises to 0 °C at an altitude of about 50 km. Above this, the mesosphere follows up to a

height of about 80 km with a similar vertically decreasing temperature gradient as in the troposphere. Then the thermosphere as the last part of the lower atmosphere follows with a continuous transition to the exosphere and finally space. The vertical structure of the atmosphere is displayed in Figure 2.2 where also the altitude, temperature gradient, air pressure and density are shown.
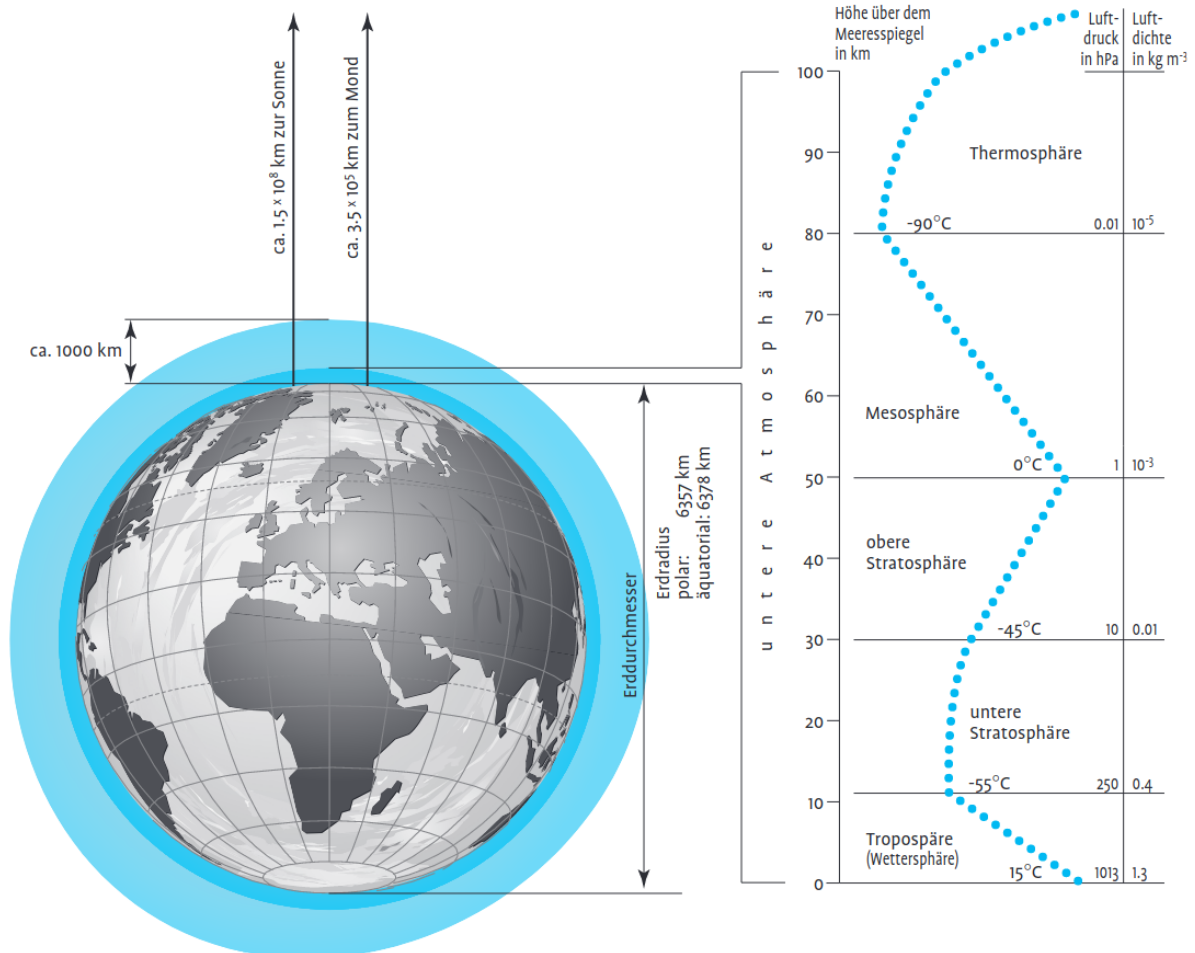

Figure 2.2: Right: Vertical structure of the atmosphere of the Earth according to thermal criteria (the dotted line represents the spatiotemporal mean temperature of the air). Left: size comparison with solid Earth. The Figure is taken from Schönwiese (2020).

Compared to the size of our Earth with a (polar) radius of 6357 km, this 100 km layer seems to be relatively thin. Nevertheless, our atmosphere makes life on Earth possible and plays an important role when it comes to the greenhouse effect (Buchal and Schönwiese, 2016; Schönwiese, 2020).

Before we can learn more about the greenhouse effect we first need to take a closer look at the composition of the air in the lower atmosphere. It consists of 78.084 % nitrogen (N_2),

20.946 % oxygen (O_2), 0.934 % argon (Ar) and 0.0409 % carbon dioxide (CO_2) such as a large number of trace gases like helium (He), carbon monoxide (CO), methane (CH_4), nitrous oxide (N_2O), sulfur dioxide (SO_2) and ozone (O_3) (Schönwiese, 2020). Another gas that is of great importance for the composition of the atmosphere and the greenhouse effect in particular is water vapour (H_2O). It has a high spatiotemporal variability, e.g. its normal mean near the surface is about 2.6 %, and affects chemical sources and sinks such as the concentration of many trace gases (Schönwiese, 2020). Without our atmosphere - or with an atmosphere only consisting of nitrogen and oxygen - the global mean temperature would be around -18 °C. This underlines the massive effect of trace gases like methane that act as GHG within our atmosphere (Buchal and Schönwiese, 2016).

To understand the natural and anthropogenic greenhouse effect we need to understand the global energy balance, which dominating source is radiation from the Sun - about $342\,\mathrm{W\,m^{-2}}$ (Roedel, 1992; Baede et al., 2001). Over 30 % of it is immediately reflected back into space by the atmosphere, clouds and the surface of our Earth. Another 25 % of this short-wave radiation is absorbed by the atmosphere and the remaining 45 % by the land and water surface on the ground (Baede et al., 2001; Buchal and Schönwiese, 2016). This energy is again released to the atmosphere as long-wave infrared radiation which is absorbed and re-emitted by GHGs like carbon dioxide, methane, nitrous oxide, ozone and water vapour as the most important of them. These processes drive heating on the Earth and lead to a global average temperature near the surface of about 15 °C, making life on earth possible (Roedel, 1992). This accumulation of heat in the lower atmosphere and the temperature increasing from -18 °C to 15 °C is called the natural greenhouse effect and consistently denoted in the relevant literature as a temperature increase of 33 K (Roedel, 1992; Baede et al., 2001; Ponater et al., 2012; Buchal and Schönwiese, 2016).

In addition to the natural greenhouse effect, the cause and impact of human activities on GHG concentration increase is a global issue that is widely discussed in- and outside science (Ehhalt et al., 2001; Schönwiese, 2020). The first one to mention a connection between humans and global warming was the swedish physicochemist Svante Arrhenius (1896). His assumption proved to be right that mainly the usage of fossil energy, which increased by a factor of 20 since the year 1900, cause a raising CO_2 concentration in the atmosphere (Arrhenius, 1896; Schönwiese, 2020). Satellite data and climate models show that the radiation budget as described above is recently not balanced. The incoming radiation of $342\,\mathrm{Wm^{-2}}$ is about $0.85\,\mathrm{Wm^{-2}}$ higher than the outgoing radiation from the Earth, leading to a warming and an increase of the surface temperature on our planet. This trend of trace gases influencing the climate can be quantified globally and for Germany within the last 100 years by about +0.7 °C and +1 °C, respectively (Buchal and Schönwiese, 2016). Recent studies and reports use the Representative Concentra-

tion Pathways (RCP) as an approach of climate projection to make prognosis for the anthropogenic greenhouse effect and its impact on global mean temperature and sea-level rise until 2100. Depending on how high the radiative forcing is assumed, different scenarios like RCP2.6 (most optimistic), RCP4.5, RCP6.0 and RCP8.5 (most pessimistic) are compared while the number denotes the radiative forcing in $\mathrm{Wm^{-2}}$. These can then be compared with with emissions and concentrations of CO_2-equivalents (IPCC, 2014; Schönwiese, 2020). An overview of the different scenarios, of which RCP8.5 is the most likely one at the moment due to Schönwiese (2020) is shown in Table 2.1.

Table 2.1: Comparison of the different RCP climate projections by IPCC (2014). Shown are RCP2.6, RCP4.5, RCP6.0, RCP8.5 with the prognosis for mean temperature increase and sea-level rise compared for 1986-2005 with 2081-2100. The ranges result from the 32-42 model simulations. Table is adapted from Schönwiese (2020).

| scenario	temp. increase	sea-level rise	CO_2-equivalent conc.
RCP2.6	0.3-1.7 °C	26-55 cm	490 ppm
RCP4.5	1.1-2.6 °C	32-63 cm	650 ppm
RCP6.0	1.4-3.1 °C	33-63 cm	850 ppm
RCP8.5	2.6-4.8 °C	45-92 cm	1370 ppm

Methane causes about 20 % of the pre-industrial global warming induced by GHGs with a warming potential even higher than carbon dioxide (Kirschke et al., 2013; Saunois et al., 2016a). Without taking care of our planet the worse scenarios will be real, including severe thunderstorms, flood events and catastrophes of all kind (IPCC, 2021). For these reasons climate research and the development of new methods to quantify and reduce the emission of GHGs is a major task and recent topic. Especially the investigation and study of global methane emissions is becoming more and more important for a mitigation of the climate change in the future.

2.2 The global methane budget

In this work we will focus on the GHG methane and therefore in this section we will have a closer look on its global budget including its sources and sinks. Regarding the total amount of emissions, methane is the second most important GHG after CO_2 affecting global warming (Saunois et al., 2016a). Although most of the sources and sinks have been specified in the past three decades of methane research, their relative contributions to the global budget are extremely uncertain (Dlugokencky et al., 2011; Kirschke et al., 2013). Within this section we first introduce the reaction of OH with methane as its main sink, leading to assertions about the atmospheric lifetime (see Section 2.2.1). Furthermore, we name and classify the most important sources of methane (see Section 2.2.2) and focus on an evaluation of the uncertainties in methane emission estimates (see Section 2.2.3).

2.2.1 Chemical sinks and atmospheric lifetime

According to AR6 of IPCC (Canadell et al., 2021) about 96% of the annually emitted $576\,\mathrm{Tg}$ methane is removed from the atmosphere by sinks from chemical reactions ($514\,\mathrm{Tg}$, 93%) and sinks in soils ($37\,\mathrm{Tg}$, 7%). The uncertainty range of global methane sinks is about 40%, most of it in wetlands (Kirschke et al., 2013). The oxidation of CH_4 with the hydroxyl radical (OH) represents its main sink (about 93% of all chemical sinks, (Saunois et al., 2020)), especially in the troposphere. The result of this reaction is carbon monoxide and the hydroperoxyl radical (HO_2) as shown in Equation 2.1.

$$OH + CH_4 \xrightarrow{k_{OH+CH_4}} H_2O + CH_3 \longrightarrow ... \longrightarrow CO + HO_2 \tag{2.1}$$
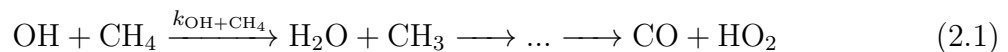
The reaction rate k_{OH+CH_4} of methane with the hydroxyl radical is calculated as

$$k_{OH+CH_4} = 2.45 \times 10^{-12} \cdot \exp\left(\frac{-1775}{T}\right) \tag{2.2}$$

according to Sander et al. (2011). The atmospheric lifetime of a substance is universally defined as the reciprocal value of the product of the reaction rate and the number concentration of the reaction partner (Seinfeld and Pandis, 2006).

Equation 2.3 shows how the atmospheric lifetime of methane is calculated. We can see that the reaction rate k_{OH+CH_4} - where temperature is an important factor (see Equation 2.2) - and the OH number concentration [OH] come into play.

$$\tau_{CH_4} = \frac{1}{k_{OH+CH_4} \cdot [OH]} \tag{2.3}$$

With a rising OH number concentration and higher temperatures the lifetime of methane decreases what leads to even higher OH concentrations and CH_4 depletion. The anti-correlation of OH number concentration and methane lifetime is displayed in Figure 2.3. For about $280\,K$ and an OH concentration of $10^6\,\#\,cm^{-3}$ (conditions near the surface of the Earth) the lifetime of atmospheric methane is about 8-10 years (Weimer, 2015) what concludes with the most common literature value for the lifetime of atmospheric methane of 9.1 years (e.g. Hayman et al., 2014).
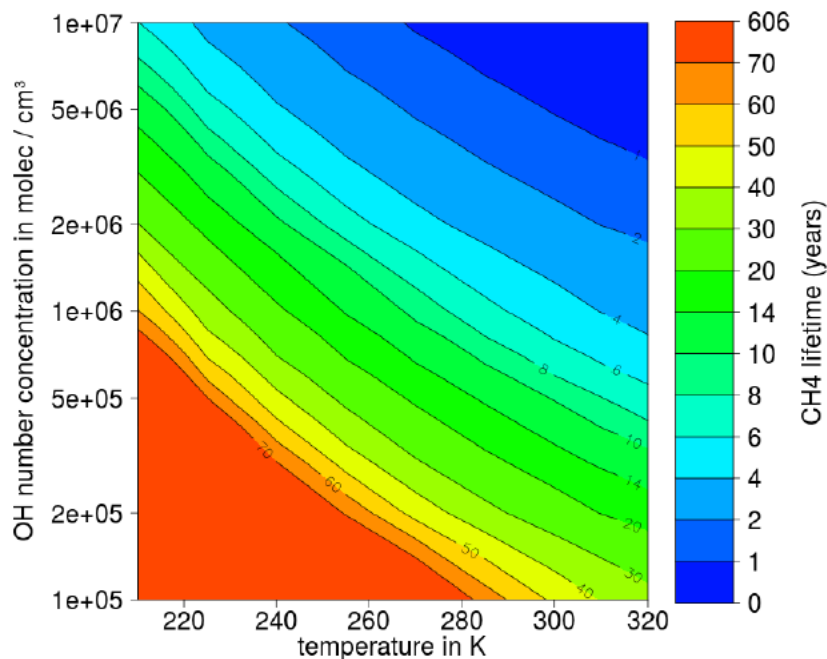

Figure 2.3: Isopleths of methane lifetime with respect to its reaction with OH. The Figure is taken from Weimer (2015).

About $90\,\%$ of the atmospheric methane is reduced by the mentioned reaction, most of it in the troposphere (Saunois et al., 2016a). The largest CH_4 loss due to its reaction with OH radicals can be recognized in the tropics because a major amount of the OH is produced there (Kirschke et al., 2013).

2.2.2 Sources of methane emissions

Even though its lifetime in the atmosphere of about 9 years is relatively short, CH_4 is the second most important GHG after CO_2 (Dlugokencky et al., 1994; Saunois et al., 2016a). The average global methane emissions in the time range 2003-2012 is estimated on 540-568 Tg CH_4 yr^{-1}, its total sinks on 529-555 Tg CH_4 yr^{-1} (GCP, 2016), leading to an annual increase of the global methane volume mixing ratio (VMR). Atmospheric measurements of the National Oceanic and Atmospheric Administration (NOAA) revealed a methane dry air mole fraction of 1810 ppbv in 2012 what is 2.5 times higher than in 1750. Figure 2.4 shows the evolution of the global mean methane VMR from 1983-2012 in ppbv as measured by NOAA and published by Dlugokencky et al. (1994).
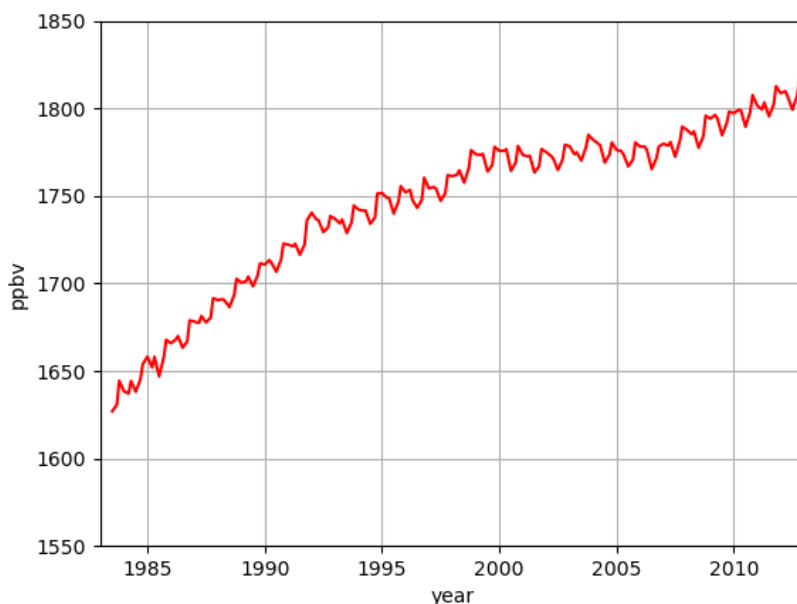

Figure 2.4: Evolution of the global mean methane VMR from 1983-2012 as measured by NOAA (Dlugokencky et al., 1994).

We recognize a steady increase until the end of the 1990s up to about 1775 ppbv, followed by about a decade of stagnation in the methane VMR until, from 2008 on, atmospheric methane VMRs began to rise again. Kirschke et al. (2013) conclude, that a decrease in fugitive emissions in fossil fuel production between 1985 and 2000 led to the stagnation, but still this topic is discussed in many recent studies (Saunois et al., 2016b; Van Dingenen et al., 2018; Nisbet et al., 2019). The time series also displays the annual cycles of methane for each year, where we recognize lower methane VMRs during summer and higher values in winter. The annual growth rate varies from -5 to 15 ppbv with an average of about

6 ppbv of methane VMR increase per year. Van Dingenen et al. (2018) conclude that the observed changes in methane growth rates are mainly influenced by emissions and the reaction with the OH radical. We will further evaluate this observation for our simulations in Chapter 5.

There are two practicable ways to structure methane emission. The first one is a division in *biogenic*, *thermogenic* and *pyrogenic* methane (Saunois et al., 2016a). *Biogenic* methane results from the decomposition of organic matter in anaerobic environments like water-saturated soils, rice plantations, waste-water facilities or the intestines of cattle. *Thermogenic* methane is the product of geological processes that are driven by heat and pressure breaking down organic matter deep in the Earth's crust. It reaches the surface for example through boreholes during the gas and oil transmission or coal mining. *Pyrogenic* methane is the result of the incomplete burning of biomass or the usage of biofuel. A second way to structure methane emission is the subdivision in *natural* and *anthropogenic* (Saunois et al., 2016a). *Natural* methane is emitted by lakes, ponds, rivers, volcanoes, wild animals, termites, permafrost soils and oceans (Saunois et al., 2016a). *Anthropogenic* methane emission are initiated by humans for example by the cultivation of rice (biogenic methane), the energy sector (thermogenic methane) or biomass burning (pyrogenic methane). Obviously a strict separation of the two alternatives is not possible, but for this work we consider the separation in anthropogenic and natural methane. Moreover, methane from anthropogenic sources is emitted within the production of fossil fuels and other industrial processes like the production of metallic and non-metallic minerals (Janssens-Maenhout et al., 2019). Also the agricultural and waste sector, where livestock farming and the cultivation of crop plays an important role, contributes about 2/3 of the anthropogenic methane emissions (Kirschke et al., 2013). All in all, about 60 % of methane emissions are from anthropogenic sources (Kirschke et al., 2013; GCP, 2016).

As shown, methane is emitted and reduced by numerous anthropogenic or natural sources and sinks that need to be examined and quantified separately. Figure 2.5 gives a simplified overview of the methane budget with its sources and sinks. As aforementioned, the most important anthropogenic sources are from the agricultural sector and the production and use of fossil fuels. Biomass burning contributes about 5-10 % to the total amount of annual methane emissions, wetlands and other natural sources like permafrost or termites represent about 40 %. Subtracting the above mentioned sinks from chemical reactions and in soils we end up with a growth rate of 10 Tg CH_4 yr^{-1} (GCP, 2016). In addition to this quantification it is important to figure out the uncertainties of the sources and sinks to get a better understanding of the global methane budget.
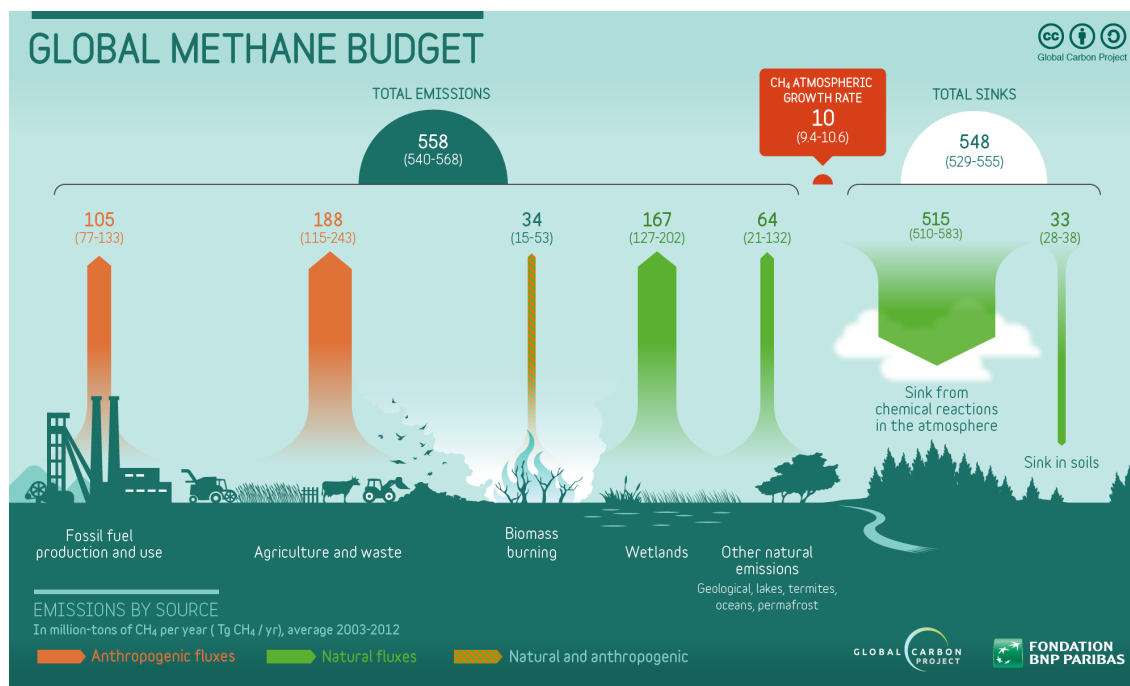
Figure 2.5: Total methane emission and reduction by source and sink in Tg CH$_4$ yr^{-1}. The Figure is taken from GCP (2016).

2.2.3 Uncertainties of methane emission estimates

In this Section we will focus on uncertainty estimates of different emission inventory reporting approaches. On the one hand there are top-down studies (TD), which originate and aggregate data at national or global levels to estimate the amount of single sources. On the other hand we will have a look at bottom-up approaches (BU) which describes data collection and processing at local levels to estimate the total amount of emissions. The advantage of BU estimates are a higher accuracy but they also much more complex and expensive when it comes to data quantity. TD approaches are faster and with this also more recent (Nicholls et al., 2015).

Although most of the methane sources are specified, their amount and intensity are highly uncertain. Anthropogenic sources have an uncertainty range of 20 % for biomass burning and 30 % for agriculture, waste and fossil fuel usage. For natural wetlands the uncertainty range is about 50 % and for other natural sources up to 100 % for BU estimates (Kirschke et al., 2013). In this section we compare the results of three studies from different years estimating the global methane budget subdivided by source. First the estimates of Khalil (2000), which is a collection of BU estimates, second a BU estimate of Saunois et al. (2016a) for the years 2003-2012 and third the TD approaches of the Global Carbon Project (GCP, 2016). Fourth and last we include the actual TD studies from the recent IPCC

Assessment Report (Canadell et al., 2021). For this comparison we subdivide the global CH$_4$ sources into the following groups:

- Biomass burning (BB)

- Anthropogenic emission without biomass burning (ANT (no BB))

- Total anthropogenic emission (ANT)

- Natural wetlands emission (WL)

- Natural emission without wetlands (NAT(no WL))

- Total natural emission (NAT)

- Total anthropogenic and natural emission (TOT)

The results of the aforementioned studies are displayed in Table 2.2 and Figure 2.6. An Overview of the datasets used in GCP (2016) is shown in Table 2.3. For each of the emission-groups the mean value of the dataset entries was calculated. The data of Canadell et al. (2021) are updated from Saunois et al. (2020) with geological emissions of Schwietzke et al. (2016), Petrenko et al. (2017) and Hmiel et al. (2020).

Table 2.2: Comparison of emission estimates of methane sources from Khalil (2000), the BU estimate for the years 2003-2012 of Saunois et al. (2016a), the TD approaches of GCP (2016) and the IPCC Assessment Report (Canadell et al., 2021). Values are given in Tg CH$_4$ yr^{-1}.

	BB	ANT (no BB)	ANT	WL	NAT (no WL)	NAT	TOT
Khalil (BU)	50	308	358	100	45	145	503
Saunois (BU)	30	322	352	185	199	384	736
GCP (TD)	39	290	329	161	52	213	543
IPCC (TD)	30	327	357	180	35	215	576

For the anthropogenic sources all three studies assume similar values between 330 and 360 Tg yr^{-1}. Also the biomass burning emissions, that take about 30 - 50 Tg yr^{-1} show minor differences between the methods. The major differences appear in the natural methane emissions what matches with the uncertainty values given in Kirschke et al. (2013). Here the BU study of Saunois et al. (2016a) assumes emissions that are higher by the factor of two compared to Khalil (2000), GCP (2016) and IPCC (2021). This comes mostly by the non-wetland natural emissions of Saunois et al. (2016a) that are higher by the factor of four compared to both other studies.
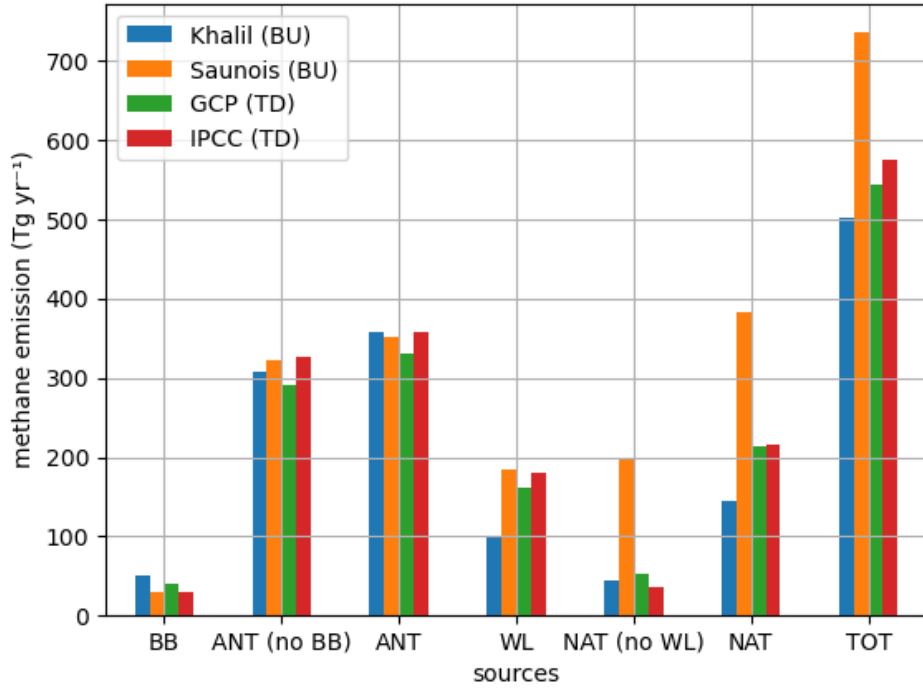
Figure 2.6: Comparison of four different emission estimates of methane sources from Khalil (2000), the BU estimate of Saunois et al. (2016a) and the TD approaches of the Global Carbon Project (GCP, 2016) and the IPCC Assessment Report (Canadell et al., 2021).

This leads to total emissions of $503\,\mathrm{Tg\,yr^{-1}}$ in Khalil (2000), $543\,\mathrm{Tg\,yr^{-1}}$ in GCP (2016) and a maximum of $736\,\mathrm{Tg\,yr^{-1}}$ in Saunois et al. (2016a). The latter assumes that emissions from anthropogenic and natural sources are almost equal. Khalil (2000), GCP (2016) and IPCC (2021) show that about $60\,\%$ of methane emissions are from anthropogenic sources.

Table 2.3: Overview of the datasets and corresponding articles used for the mean values of the GCP TD approach in Table 2.2 and Figure 2.6.

TM5-EC-JRC/SURF	Bergamaschi et al. (2013), Alexe et al. (2015)
LMDz-MIOP	Pison et al. (2013)
CT-CH4/SURF	Bruhwiler et al. (2014)
TM5-SRON/SCIA and SURF	Houweling et al. (2014)
GELCA/SURF	Ishizawa et al. (2016), Zhuravlev et al. (2013)
ACTM/SURF	Patra et al. (2016)

The aforementioned studies contain global data, including land and sea surface, although compared to CO_2 the role of the oceans in the global methane budget is relatively small with a contribution of only 1-3 % what leads Saunois et al. (2016a) to call source estimation mostly a continental problem.

2.3 Atmospheric emission inventories

Since the Kyoto Protocol entered into force in February 2005, the international community of nations committed itself to reduce GHG emissions with the overall aim of protecting the global climate. Within the framework of the second committed period of the Kyoto Protocol the European countries have agreed to reduce their GHG emissions by 20 % by 2020 (Strogies and Gniffke, 2018).

National reports with standardized guidelines are the basis for transparent inventories which include information about the amount and the geographical locations of the different pollutants that are emitted. Three well established BU inventories that cover global anthropogenic emissions are the Greenhose gas and Air pollutant Interactions and Synergies model (GAINS) developed by the International Institute for Applied System Analysis (IIASA, Höglund-Isaksson (2012)), the inventories from the United States Environmental Protection Agency (USEPA, 2006) and the Emission Database for Global Atmospheric Research (EDGAR, Janssens-Maenhout et al. (2019)), an inventory from the European Commission Joint Research Centre (EC-JRC) and Netherland's Environmental Assessment Agency (Saunois et al., 2016a). Although the level of detail varies between the different inventories such as the number of sectors and regions provided, all of them contain the major anthropogenic sources for methane emission: The production, transmission and distribution of fossil fuel, livestock (enteric fermentation and manure management), rice cultivation, solid waste and waste water.

Emission inventories are of high importance when working with global atmospheric chemistry models e.g. as emission input data. The comparison of model simulations to established emission inventories and the adjustment of missing emissions are an essential part of this work. Following this general description of atmospheric emission inventories, we will have a deeper insight into the national inventory reports and guidelines (see Section 2.3.1). Afterwards a more detailed overview of the emission database EDGAR and the offshore installations inventory of the Oslo-Paris commission (OSPAR) is given, closing with the basic problem that motivates this work.

2.3.1 National inventory reports and guidelines

The United Nations Framework Convention on Climate Change (UNFCCC, 1992) was signed two years after the first assessment report of the Intergovernmental Panel on Climate Change (IPCC, 1990) with the goal to collect nationally reported GHG emission inventories. When the UNFCCC was drafted, the 24 OECD countries in 1990 were grouped together with 16 other European states and Russia to the so called Annex I countries. To demonstrate their effort in reducing anthropogenic GHG emissions and to ensure transparency, completeness, comparability, consistency and accuracy the Annex I countries and the EU annually submit complete inventories of their national GHG emission sources and sinks relative to the base year 1990 to the UN. Non-Annex I countries are encouraged to submit emission inventories at least biennial for the 3 main GHGs CO_2, CH_4 and N_2O. Until now 150 countries have submitted one or more national reports (Janssens-Maenhout et al., 2019). The actual reports are accessible on the UNFCCC homepage for all Annex I countries (UNFCCC, 2020).

The German annual report is conducted by the German Environment Agency (UBA) in Dessau (Strogies and Gniffke, 2020) with categories in the IPCC 1996 standard. For this work the IPCC category 1.B (Fugitive emissions from fuels) is of high importance because methane emissions from solid fuels and fugitive emissions from natural gas and oil are the major part of it. More precisely, we take a deeper look at the subcategory 1.B.2 (Oil and natural gas and fugitive emissions from energy production) only. Table 2.4 gives an overview of the source categories in 1.B.2. Some things are remarkable about this definition of the source categories in 1.B.2. The exploration of oil and gas is not separated and therefore the emissions from exploration of gas (1.B.2.b.i) is included in the exploration of oil (1.B.2.a.i). Also the emissions from venting are assigned to the transport and distribution categories of oil and gas. The exact amount of reported methane emissions is shown in Table 2.5. These values are calculated from activity rates and emission factors using the different IPCC Tier methods, e.g. with regard to emission levels for individual categories in one year (Tier 1 level assessment), time series analysis of inventory data (Tier 1 trend assessment) or detailed analysis of inventory data with error evaluation (Tier 2 level and trend assessment with consideration of uncertainties) (Strogies and Gniffke, 2020). Information about how data reporting works and details about the calculation using different activity data and emission factors for the specific source categories can be found on the websites of UBA (2019). For example the calculation of source category 1.B.2.a.iii (Transport of crude oil) the activity data are the transports of domestically produced crude oil, the transports of imported crude oil and the transports via inland-waterway tankers in kilotons. The emission factor for methane emissions in this category varies for each of the activity data between 0.0064 and 0.013 kg t^{-1}.

Table 2.4: Structure and description of the source sector 1.B.2 in IPCC 1996 standard. Table is adapted from Strogies and Gniffke (2020).

IPCC sector	Short name	Included emissions
1.B.2.a	**Oil**	
1.B.2.a.i	Exploration	Total emissions from exploratory drilling for oil and gas
1.B.2.a.ii	Production	Fugitive emissions from oil production and from oil processing (separation of water and accompanying gases)
1.B.2.a.iii	Transport	Emissions from transport of crude oil via pipelines and inland- waterway tankers
1.B.2.a.iv	Refining and storage	Emissions from oil desulphurisation and refining, from storage of crude oil and of petroleum products and from cleaning of storage tanks
1.B.2.a.v	Distribution	Emissions from distribution of petroleum products, from refuelling processes and drip losses and from cleaning of tanks of transport vehicles
1.B.2.a.vi	Other	No emissions in this category
1.B.2.b	**Gas**	
1.B.2.b.i	Exploration	The emissions are assigned to category 1.B.2.a.i, since no differentiation is possible
1.B.2.b.ii	Production	Fugitive emissions from natural gas production
1.B.2.b.iii	Processing	Emissions from desulphurisation and processing of sour gas and from processing of town gas
1.B.2.b.iv	Transport	Emissions from long-distance high-pressure pipelines and from underground gas storage (caverns and porous-rock reservoirs)
1.B.2.b.v	Distribution	Emissions from natural-gas distribution lines, and from above- ground storage facilities, and fugitive leaks from tanks of vehicles for natural-gas transport
1.B.2.b.vi	Other	Fugitive emissions from installations in the residential, institutional and commercial (small consumers) and industry sectors
1.B.2.c	**Venting and flaring**	
1.B.2.c.i	Venting	The emissions from oil are included in the categories 1.B.2.a.iii and 1.B.2.a.v, the emissions from gas are included in the categories 1.B.2.b.iv and 1.B.2.b.v
1.B.2.c.ii	Flaring	Flaring emissions related to oil production and refining such as flaring emissions related to natural gas production and to processing of sour gas

Table 2.5: Reported German annual methane emissions for 2018 in source sector 1.B.2 (Strogies and Gniffke, 2020).

IPCC sector	Short name	Included emissions [t]
1.B.2.a	**Oil**	
1.B.2.a.i	Exploration	1.216
1.B.2.a.ii	Production	37
1.B.2.a.iii	Transport	574
1.B.2.a.iv	Refining and storage	2441
1.B.2.a.v	Distribution	-
1.B.2.a.vi	Other	-
1.B.2.b	**Gas**	
1.B.2.b.i	Exploration	-
1.B.2.b.ii	Production	240
1.B.2.b.iii	Processing	101
1.B.2.b.iv	Transport	77000
1.B.2.b.v	Distribution	86000
1.B.2.b.vi	Other	28800
1.B.2.c	**Venting and flaring**	
1.B.2.c.i, 1.B.2.c.ii	Venting and flaring	24

Again considering the above mentioned example of category 1.B.2.a.iii (Transport of crude oil) the annual emission is calculated via the IPCC Tier 2 method as:

$$ 85200000 \ \frac{t}{a} \ \cdot \ 0.0064 \ \frac{kg}{t} \ + \ 2100000 \ \frac{t}{a} \ \cdot \ 0.013 \ \frac{kg}{t} \ \approx \ 572 \times 10^3 \ \frac{kg}{a} $$

Activity data for transports of imported and domestically produced crude oil
Emission factor for transports of imported and domestically produced crude oil

The interim result of 572×10^3 kg a^{-1} is then multiplied by a category specific uncertainty factor according to the IPCC Tier 2 method which is unfortunately not specified by any of the involved agencies. Only Strogies and Gniffke (2020) define a range for the uncertainties of emission factors of -20 % - 20 % and activity data of -10 % - 10 %, leading to methane emissions for the source category 1.B.2.a.iii (Transport of crude oil) of 574×10^3 kg a^{-1}

which is satisfyingly near to the result of our example calculation above. All activity rates and emission factors for the source categories can be found in Strogies and Gniffke (2020).

The data in the annual national inventory reports are collected, stored and processed by UBA as the national coordination agency in Germany. At ministerial level, the responsibility lies with the Federal Ministry for the Environment, Nature Conservation and Nuclear Safety (BMU) working together with the Federal Ministry of Food and Agriculture (BMEL), for Economic Affairs and Energy (BMWi), of Transport and Digital Infrastructure (BMVI), of the Interior, Building and Community (BMI), of Finance (BMF) and of Defence (BMVg). The concrete data acquisition begins at a lower administrative level because the municipalities and regional authorities are responsible to collect data of facilities that are obliged to report their GHG emissions (Strogies and Gniffke, 2020). An overview of the emission reporting process is shown in the flow chart in Figure 2.7.
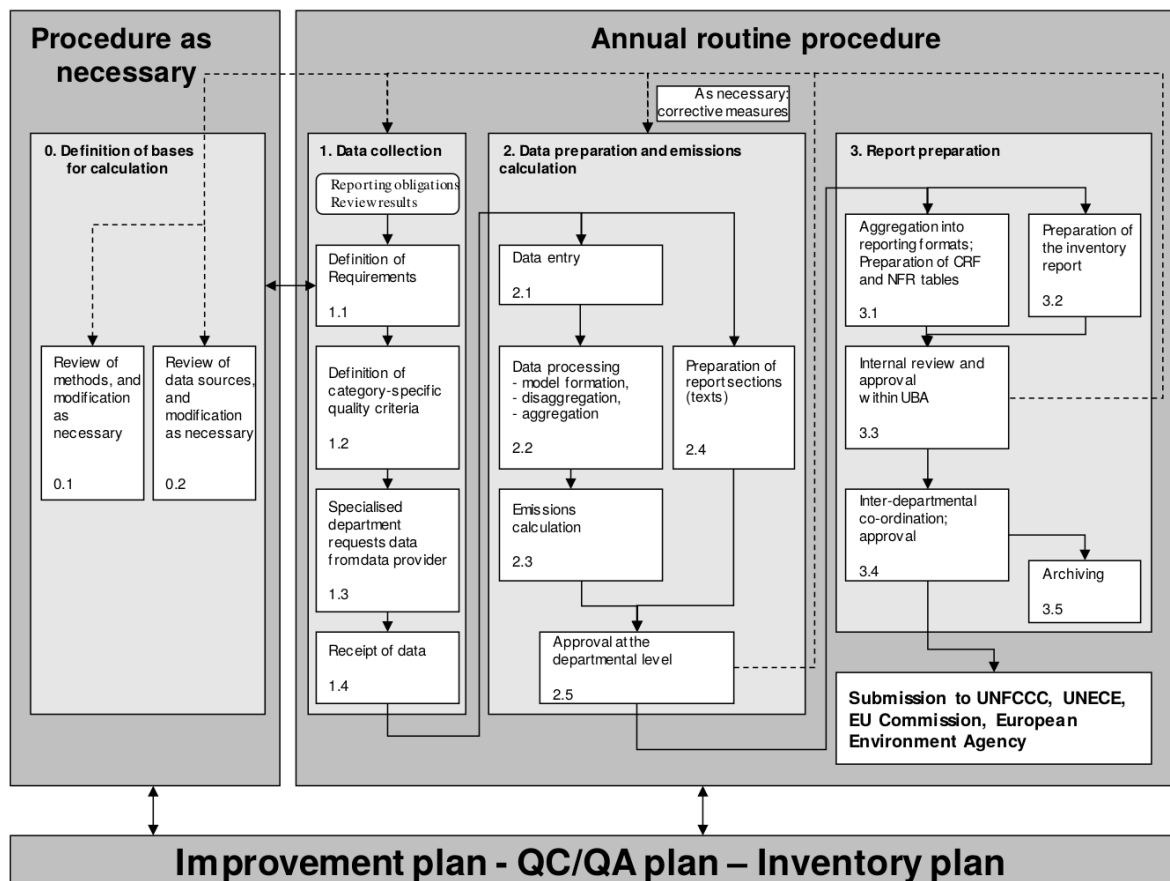
Figure 2.7: Flow chart of the emission-reporting process. The Figure is taken from Strogies and Gniffke (2020).

For example in Germany the data collection as shown in Figure 2.7 is anonymous so that no conclusions can be drawn about individual facilities. Especially the emissions from on- and offshore oil and gas explorations are combined and not reported separately. Only the total production of oil and gas in tons per year are reported in the annual statistical report of the federal association of natural gas, oil and geoenergy (BVEG) as specified in BVEG (2019). As visible in Figure 2.7, the national inventory reports are submitted to the UNFCCC that conducts a European Pollutant Release and Transfer Register (E-PRTR). It provides information about emissions from industrial facilities, transparent and free (E-PRTR, 2020). Also Germany has a national PRTR called THRU conducted by the UBA where the German facilities and data concerning GHG emissions are available (THRU, 2020).

The European PRTR Regulation of January 2006 (E-PRTR, 2006) lays down rules on how emissions must be reported and also specifies which activities are subject to reporting requirements. Appendix I of the E-PRTR Regulation provides a list of activities and the corresponding capacity thresholds that build the basis on which to decide if a facility is obligated to report their GHG emissions or not. For emissions of offshore platforms there are two possible activities according Appendix I of the E-PRTR regulation where the United Kingdom and Norway are reporting into (E-PRTR, 2006, 2020):

1 (c) Energy sector - Thermal power stations and other combustion installations - Extraction of crude petrolium

3 (a) Mineral industry - Underground mining and related operations - Extraction of natural gas

Germany has two offshore platforms. The oil exploiting platform Mittelplate in the Wadden Sea near the coast of Schleswig Holstein and the gas platform A6-A in the exclusive economic area of Germany in the North Sea. Both German platforms are not reported due to the E-PRTR regulation because due to UBA natural oil and gas production as an activity cannot be assigned to any of the activities listed in Appendix I of the E-PRTR Regulation. Therefore no PRTR reporting obligations exist for Mittelplate and A6-A (Grimm, 2020).

2.3.2 Emission Database for Global Atmospheric Research (EDGAR)

The Emission Database for Global Atmospheric Research (EDGAR, Janssens-Maenhout et al. (2019)) is an inventory from EC-JRC and Netherlands' Environmental Assessment Agency (Saunois et al., 2016a). It is provided by the online database ECCAD (2018). National inventory reports of GHG emissions as presented in Section 2.3.1 are the basis for emission inventories with the difference that EDGAR uses the same IPCC Tier method for all sectors and countries to homogenize the global emision map. The EDGARv4.3.2 inventory used as emission input for the simulations in this work covers sector- and country-specific time series of 1970-2012 with monthly means and a global spacial resolution of $0.1° \times 0.1°$ providing CH_4, CO_2, CO, SO_2, NO_x, C_2H_6, C_3H_8 and many other species (Janssens-Maenhout et al., 2019). Different source sectors in EDGAR are defined using the IPCC 1996 guidelines as displayed in Table 2.6 for the example of the fuel production and transmission sector PRO and the sector of oil refineries and transformation industry REF_TRF (Janssens-Maenhout et al., 2012). The sectors are equal for all GHG and chemical species in EDGAR. Regarding Table 2.6 which is similar to Table 2.5 we can see that beside category 1.B.1.a (coal mining) - on which we will not focus in this work - all emissions from oil (1.B.2.b) are used as well as venting and flaring emissions (1.B.2.c) for the EDGAR code PRO. As aforementioned, emissions from gas exploration (1.B.2.b.i) are contained in the corresponding oil sector. Nevertheless, the major part in IPCC source sector 1.B.2 are emissions from gas (1.B.2.b) which are partly contained in PRO and REF_TRF but not in any of the other EDGAR codes (EC-JRC, 2020a) which leads to the conclusion that some emissions are missing in the EDGAR emission inventory for whatever reason.

The newer version of EDGARv5.0 released in 2019 (EC-JRC, 2020b) seperates emissions of PRO into the subsectors PRO_COAL (IPCC 1.B.1.a), PRO_OIL (IPCC 1.B.2.a.i - 1.B.2.a.iv) and PRO_GAS (IPCC 1.B.2.c) with the latter only containing emissions from venting and flaring and not the apparently missing data of EDGARv4.3.2.

Table 2.6: Comparison of EDGAR codes PRO and REF_TRF with IPCC 1996 source sectors (EC-JRC, 2020a). Emission values and descriptions are taken from Strogies and Gniffke (2020).

EDGAR code	IPCC sector	Short name	Included emissions [t]
	1.B.1.a	**coal mining**	
PRO	1.B.1.a.i	Underground mining	61.2
PRO	1.B.1.a.ii	Open-pit mining	1.8
	1.B.2.a	**Oil**	
PRO	1.B.2.a.i	Exploration	1.216
PRO	1.B.2.a.ii	Production	37
PRO	1.B.2.a.iii	Transport	574
PRO	1.B.2.a.iv	Refining and storage	2441
REF_TRF	1.B.2.a.v	Distribution	-
REF_TRF	1.B.2.a.vi	Other	-
	1.B.2.b	**Gas**	
-	1.B.2.b.i	Exploration	-
-	1.B.2.b.ii	Production	240
-	1.B.2.b.iii	Processing	101
-	1.B.2.b.iv	Transport	77000
REF_TRF	1.B.2.b.v	Distribution	86000
-	1.B.2.b.vi	Other	28800
	1.B.2.c	**Venting and flaring**	
PRO	1.B.2.c.i, 1.B.2.c.ii	Venting and flaring	24

A comparison of the total emission contained in EDGAR with the value of all national inventory reports is not possible as many countries report their emissions not regularly and incomplete as well as it is not transparent in EDGAR which data are used for such non-Annex I countries. In addition, different countries report the data in their national inventory reports with different levels of detail (UNFCCC, 2020).

The next important question concerning the EDGAR emission inventory is how the sector specific data is calculated and then spatially distributed on the maps. Therefore, a differentiation of emission processes improve and refine the estimates of EDGAR with technology-specific emission factors, end-of-pipe abatement measurements, modeling based on latest scientific knowledge, available global statistics and IPCC-recommended methods (Janssens-Maenhout et al., 2019). Emissions in EDGARv4.3.2 are calculated

explicitly as displayed in Equation 2.4 (Janssens-Maenhout et al., 2019).

$$
\begin{aligned}
\mathrm{EM_i}(C,t,x) \quad = \quad \sum_{j,k} \Big[\quad &\mathrm{AD_i}(C,t) \\
\cdot \quad &\mathrm{TECH_{i,j}}(C,t) \\
\cdot \quad &\mathrm{EOP_{i,j,k}}(C,t) \\
\cdot \quad &\mathrm{EF_{i,j}}(C,t,x) \\
\cdot \quad &(1 - \mathrm{RED_{i,j,k}}(C,t,x) \quad \Big]
\end{aligned}
\tag{2.4}
$$

The factors of Equation 2.4 are specified below.

$\mathrm{EM_i}(C,t,x):$ Emissions from a sector i in a country C accumulated during a year t for a chemical compound x

$\mathrm{AD_i}(C,t):$ Country-specific activity data for sector i and year t

$\mathrm{TECH_{i,j}}(C,t):$ Mix of j different technologies in sector i and year t for country C

$\mathrm{EOP_{i,j,k}}(C,t):$ Mix of k different end-of-pipe abatement measurements in sector i and year t for country C installed with share k for each technology j

$\mathrm{EF_{i,j}}(C,t,x):$ Emission rate with uncontrolled emission factor in sector i and year t for country C and technology j

$\mathrm{RED_{i,j,k}}(C,t,x):$ Relative reduction of the chemical compound x by abatement measure k in sector i and year t for country C and technology j

These calculations are dependent on many parameters e.g. the consumed energy of a particular fuel type or the amount of products manufactured what leads to a differentiation and determination of the factors of Equation 2.4 at different levels: country specific,

regional, country group (e.g. Annex I) or global. In addition to that technology-specific emission factors are used to take into account the different infrastructures and international annual statistics are used to avoid inaccuracies of monthly or daily fluctuations (Janssens-Maenhout et al., 2019).

The above calculated sector specific total emissions of a substance x in year t for country C are now distributed in space and time as Equation 2.5 displays. The emissions of a grid cell expressed by its coordinates (lat, lon) in sector i of year t and country C are $\mathrm{em}_i(lat, lon, t, x)$ and depend on $\mathrm{EM}_i(C, t, x)$ (see Equation 2.4). In addition to that monthly shares m and spatial proxy datasets f are used, both depend on specific factors for each technology j. The Heaviside function H equals 1 if the grid cell is inside the country area of C (Janssens-Maenhout et al., 2019).

$$
\begin{aligned}
\mathrm{em_i}(lat, lon, t, x) \quad &= \quad \mathrm{EM_i}(C, t, x) \\[1em]
&\quad \cdot \quad \frac{\mathrm{m_{i,j}}(C)}{\sum_{l=1,\ldots,12} \mathrm{m_{i,j}}(C)} \\[1em]
&\quad \cdot \quad \frac{\mathrm{f_{i,j}}(lat, lon, t)}{\sum_{lat,lon}\Big(\mathrm{f_{i,j}}(lat, lon, t) \cdot \mathrm{H}(lat, lon, C)\Big)} \quad (2.5)
\end{aligned}
$$

with

$$
\mathrm{H}(lat, lon, C) \quad = \quad
\begin{cases}
1 & \text{if} \quad (lat, lon) \in C \\
0 & \text{if} \quad (lat, lon) \notin C
\end{cases}
$$

The proxy datasets are based on national spatial data containing information about population density, the road network, waterways, aviation and shipping trajectories (Janssens-Maenhout et al., 2012). A global $0.1° \times 0.1°$ grid is used onto which the emissions are assigned, either emitted from a single pointsource (e.g. oil or gas platforms), distributed over a line source (e.g. shiptracks) or over an areal source (e.g. agricultural fields) always depending on the source sectors and subsectors. For this work pointsources are of high importance. These zero-dimensional sources are allocated to a single grid cell of the $0.1° \times 0.1°$ grid with the average of all points that fall into the same cell (Janssens-Maenhout et al., 2019). An overview of the EDGAR proxy data can be found in Table III.1.1 in Janssens-Maenhout et al. (2012). The proxy dataset that is used for offshore oil and gas platforms is based on the data that is available in E-PRTR (2020). As we learned

in section 2.3.1 the European register is neither representing a complete picture of the facilities in the study area nor are the reporting obligations interpreted in the same manner. Furthermore the proxy data is not open source and a deeper investigation therefore difficult.

We are finally taking a look at EDGAR methane fluxes in Europe and the North Sea Region (NSR) in particular as displayed in Figure 2.8. Values are relatively high over the surface of the landmass surrounding the North Sea. The resolution of $0.1° \times 0.1°$ makes it possible that industrial regions and also cities are visible as single pixels. The orography of the Norwegian landscape is resolved by the EDGAR inventory as well as big cities like London, Oslo and Berlin, which are emission hotspots in the dataset. Over sea we recognize shiptracks in and outside the North Sea, which are clearly outstanding from the background due to the proxy datasets on which EDGAR is based.
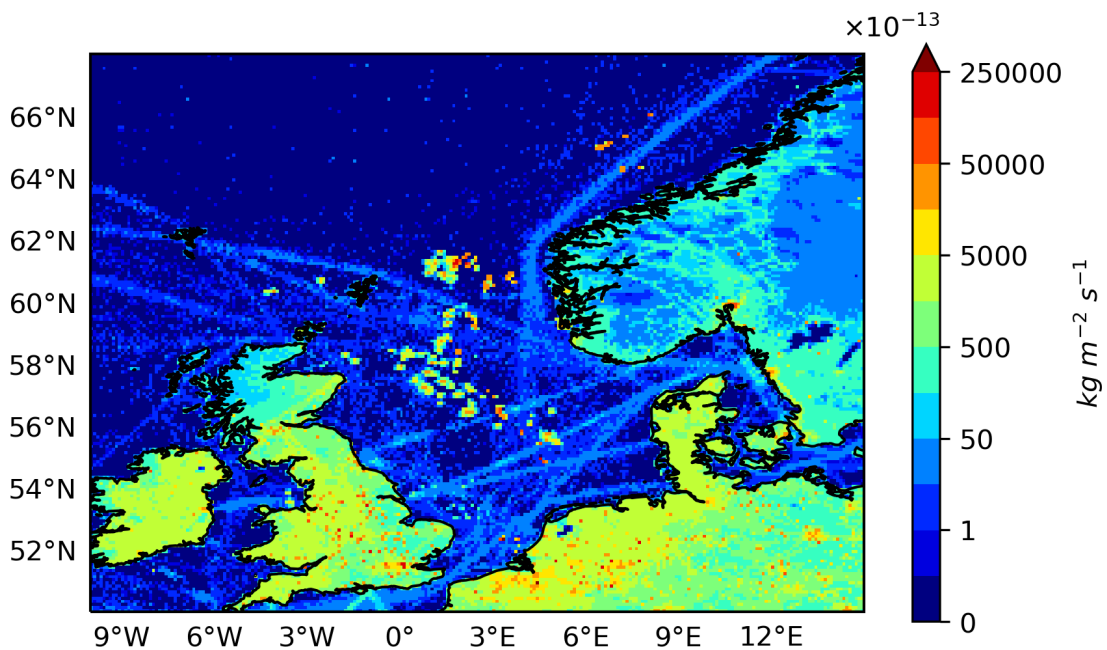
Figure 2.8: Methane emission fluxes in EDGAR 4.3.2 show relatively high values in the NSR due to pointsources of oil and gas platforms in the proxy datasets.

2.3.3 OSPAR offshore installations inventory

The Oslo-Paris commission has the goal to protect and conserve the North-East Atlantic ocean - in particular the North Sea - and its resources. Starting in 1972 OSPAR monitors the development of offshore installations and publishes inventories containing the name, ID number, location, operator, water depth, production start, current status, category and function of offshore installations. The latest version was published in 2017. The countries with oil and gas industry offshore installations are: Denmark, Germany, Ireland, the Netherlands, Norway, Spain and the United Kingdom (OSPAR, 2017). Figure 2.9 shows a map of Europe with all 914 active offshore oil and gas platforms from the OSPAR inventory of installations displayed on it. The installations can be split in two main clusters, the big amount of platforms in the southern part of the NSR between the coastal areas of the United Kingdom and the Netherlands, where mostly gas is exploited and a cluster in the northern part of the NSR where mostly oil platforms are located.
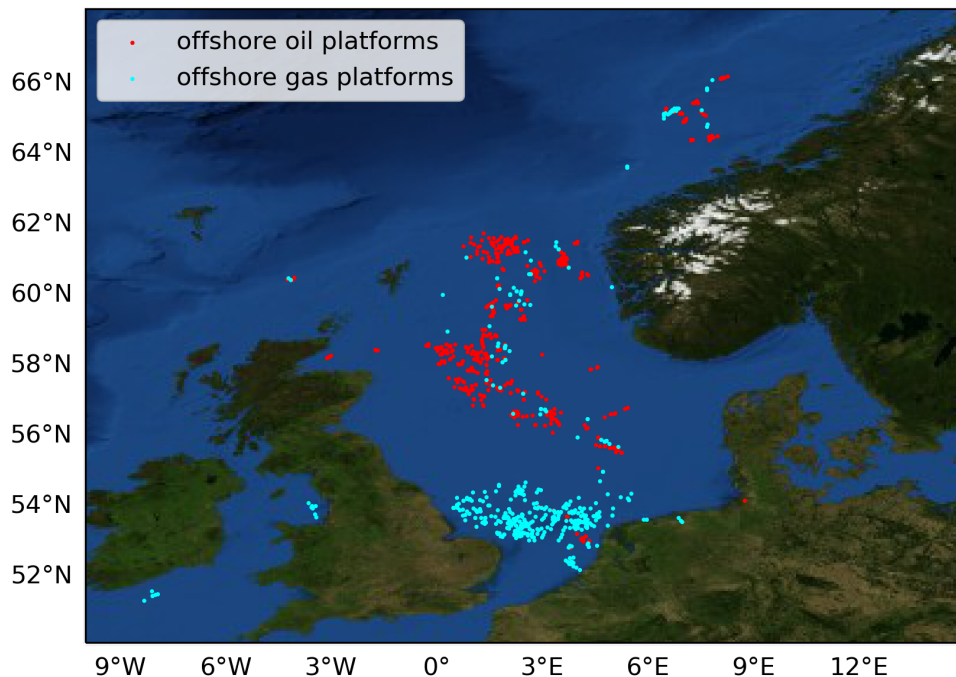
Figure 2.9: Satellite image of the NSR with offshore oil (red) and gas (blue) exploration platforms.

For this work we want to concentrate on the high emissions that are visible in the North Sea which are related to offshore platforms as displayed and explained within Figure 2.8. If we compare the EDGAR emission fluxes and the OSPAR platform locations as shown in Figure 2.9 two things are remarkable. First, for the upper part of the NSR the fluxes and the platform locations match quite well due to the proxy datasets. The second thing is, that in the southern part of the NSR there are many platforms visible but no emission fluxes in EDGAR. As we learned in the sections before, this can have at least two reasons: As explained in Section 2.3.1 oil and gas emissions are not separated within the international reporting guidelines and together with high bureaucratic hurdles that leads to inconsistent data. In Section 2.3.2 we learned that the proxy data of EDGAR, on which the emissions are distributed, are based on the E-PRTR register, which is not necessarily representing a complete picture of the facilities in the study area. These two reasons lead us to the assumption that GHG emissions are missing in the internationally well-established emission inventory EDGAR.

Within this work we want to investigate the impact of missing emissions on the regional and global methane budget. We also aim to find new ways how missing emissions can be adjusted and quantified more accurate and independent from national reports with high uncertainties.

3   The Modeling Framework ICON-ART

3.1 General description

The ICOsahedral Non-hydrostatic (ICON) modelling framework (Zängl et al., 2015) is a joint development of Deutscher Wetterdienst (DWD) and Max Planck Institute for Meteorology (MPI-M) which became operational in DWD's forecast system in January 2015. The main goals and characteristics that make ICON an outstanding next generation numerical weather prediction (NWP) and climate modeling system are the exact local mass conservation and mass-consistent transport formulated as non-hydrostatic equations, the scalability on parallel high-performance computing (HPC) architectures and the availability of vertical nested grid such as one-way and two-way horizontal nesting for spatial resolutions down to 100 m (Zängl et al., 2015; Prill et al., 2019). The calculations of the ICON model are performed on an icosahedral-triangular C grid, which allows to overcome problems with boundary conditions and singularities, e.g. at the poles (e.g. Staniforth and Thuburn, 2012). In addition to that, global and local grid refinement is easily possible within this type of horizontal grid as shown in Sadourny et al. (1968). The nomenclature of grids in ICON is defined as follows:

Grids are denoted RnBk if the edges of the original icosahedron are divided into n parts which are then subsequently bisected k-times to achieve the targeted refinement. With this construction, each vertex of a global grid is surrounded by exactly six triangles. Exceptions are the twelve vertices of the original icosahedron, the so called pentagon points, which are adjacent to only five of the triangular grid cells (Sadourny et al., 1968; Prill et al., 2019). Vertically, the ICON model reaches a height of 75 km usually subdivided in 90 levels, starting with a lowest model level of 20 m above the ground. Figure 3.1 illustrates the horizontal grid construction in ICON. As shown by Prill et al. (2019) the

total number of triangular grid cells within a global R*n*B*k* grid in ICON is

$$n_{cells} \quad = \quad 20n^2 4^k \tag{3.1}$$

and the resulting effective mesh size is given as

$$\overline{\Delta x} \quad = \quad \frac{R_{earth}}{n2^k}\sqrt{\frac{\pi}{5}} \quad \approx \quad \frac{5050}{n2^k} \qquad [km] \tag{3.2}$$

where R_{earth} is the radius of the Earth.
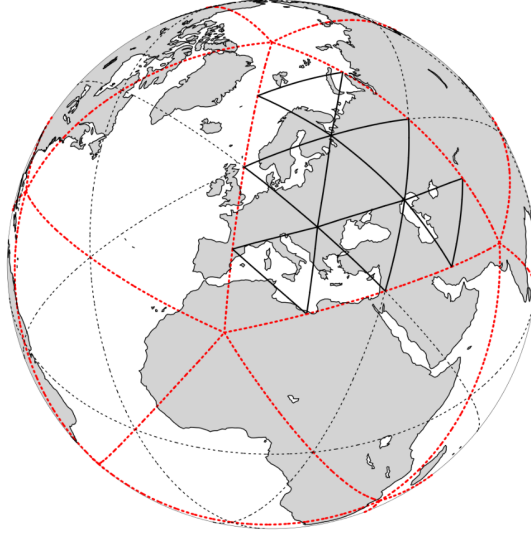
Figure 3.1: Illustration of the grid construction in ICON. The original icosahedron is displayed in red. In this example, the initial division (n=2, black dotted) is followed by one subsequent edge bisection (k=1, black solid). The result is a R2B1 grid. The Figure is taken from Prill et al. (2019).

Within this work a global R2B5 grid of ICON is used which contains 81 920 triangular cells and has a mesh size of $\overline{\Delta x} = 78.9$ km. Additionally three simulations were performed with a higher resolution of $\overline{\Delta x} = 39.4$ km. This R2B6 grid consists of 327 680 triangular cells.

The dynamical core of ICON consists of a non-hydrostatic formulation and is based on Gassmann and Herzog (2008). It solves the Navier-Stokes and the continuity equations as well as the first law of thermodynamics and is expressed as follows:

$$\frac{\partial v_{\mathrm{n}}}{\partial t} + \frac{\partial K_{\mathrm{h}}}{\partial n} + (\zeta + f)v_{\mathrm{t}} + w\frac{\partial v_{\mathrm{n}}}{\partial z} = -c_{\mathrm{pd}}\theta_v\frac{\partial \pi}{\partial n} + F(v_{\mathrm{n}}) \tag{3.3}$$

$$\frac{\partial w}{\partial t} + \mathbf{v}_{\mathrm{h}} \cdot \nabla w + w\frac{\partial w}{\partial z} = -c_{\mathrm{pd}}\theta_v\frac{\partial \pi}{\partial z} - g \tag{3.4}$$

$$\frac{\partial \rho}{\partial t} + \nabla \cdot (\mathbf{v}\rho) = 0 \tag{3.5}$$

$$\frac{\partial \rho\theta_v}{\partial t} + \nabla \cdot (\mathbf{v}\rho\theta_v) = \tilde{Q} \tag{3.6}$$

$$\frac{\partial \pi}{\partial t} + \frac{R_{\mathrm{d}}}{c_{\mathrm{vd}}}\frac{\pi}{\rho\theta_v}\nabla \cdot (\mathbf{v}\rho\theta_v) = \hat{Q} \tag{3.7}$$

with

$$\pi = \left(\frac{R_{\mathrm{d}}}{p_{00}}\rho\theta_v\right)^{\frac{R_{\mathrm{d}}}{c_{\mathrm{vd}}}} \tag{3.8}$$

the Exner function.

Here the prognostic variables are the horizontal and vertical wind components v_{n} and w, respectively, where the index n stands for the component of v perpendicular to the edges of the triangular grid. Furthermore, $\mathbf{v}_{\mathrm{h}}$ denotes the horizontal wind tangential to the triangle edges where $\mathbf{v}$ is the three dimensional wind. The virtual potential temperature θ_v and air density ρ are also prognostic variables in this set of equations and p_{00} represents a reference pressure of 1000 hPa which is used for the definition of potential temperature. Moreover, ζ indicates the vertical vorticity component, f is the Coriolis parameter, K_{h} is the horizontal kinetic energy, c_{pd} denotes the heat capacity for constant pressure and c_{vd} for constant volume, leading to the gas constant of dry air R_{d} which is defined as the difference of c_{pd} and c_{vd}. The diabatic heat source terms are $\tilde{Q}$ and $\hat{Q}$ and the source term for the horizontal momentum is $F(v_{\mathrm{n}})$. Finally, t denotes time and z the geometric height. A more detailed explanation of the dynamical core of ICON can be found in Zängl et al. (2015). An overview of the prognostic variables, physical constants and symbols used within Equations 3.3 - 3.8 of the dynamical core of ICON is provided in Table 3.1.

Table 3.1: Overview of the prognostic variables, physical constants and symbols used in the dynamical core of ICON.

symbol	explanation
t	time
z	geometric height
v_n	horizontal wind component, n denotes component of v normal to edges
w	vertical wind component
$\mathbf{v}_\mathrm{h}$	horizontal wind tangential to edges, $\mathbf{v}$ is three dimensional wind
θ_v	virtual potential temperature
ρ	air density
p_{00}	reference pressure of $1000\,\mathrm{hPa}$, used for definition of pot. temp.
ζ	vertical vorticity component
f	coriolis parameter
K_h	horizontal kinetic energy
c_pd	heat capacity for constant pressure
c_vd	heat capacity for constant volume
R_d	gas constant of dry air, which is defined as $(c_\mathrm{pd} - c_\mathrm{vd})$
$\tilde{Q}, \hat{Q}$	diabatic heat-source terms
$F(v_\mathrm{n})$	source term for the horizontal momentum
$\frac{\partial}{\partial n}$	horizontal derivative in triangle-edge normal direction

The ART (Aerosols and Reactive Trace gases) modules developed at Karlsruher Institute of Technology (KIT) extend the numerical weather and climate prediction system ICON with chemistry, aerosol dynamics and radiation feedback processes (Rieger et al., 2015). ICON-ART is well suited at simulating interactions between the trace substances and the state of the atmosphere by coupling the spatiotemporal evolution of tracers with atmospheric processes (Schröter et al., 2018).

In the following sections of this chapter we will take a closer look at ART modules like the emissions (Section 3.2) and the pointsource module (Section 3.3). We will also focus on other ICON-ART specifications like the chemistry setup which is used for this work (Section 3.4).

3.2 The emissions module

As already mentioned in Section 2.2.2, trace gases like methane are emitted into the atmosphere by many different sources from the surface of the Earth. For a simulation of these hereafter called tracers in global atmospheric chemistry models, many different approaches have been taken in the last decades (e.g. McKeen et al. (1991) or Keller et al. (2014)). In this section, the emissions module of ICON-ART as explained in Weimer et al. (2017), is introduced.

As a first step the raw data of the emissions in the netCDF format, e.g. from the EDGAR inventory, are taken and splitted into separate files for each time step. During this pre-processing phase the emissions, which are usually given as regular latitude-longitude data, are remapped to the native ICON triangular grid and saved with metadata following the structure and naming convention

ART_<X>_iconR<n>B<k>-grid-yyyy-mm-dd-hh_<grid-num>.nc

where <X> denotes a three character abbreviation of the emission types anthropogenic (ANT), biogenic (BIO) and biomass burning (BBE). As introduced in Section 3.1 <n> and <k> are the resolution indicators of the ICON grid. After initialising the emission structure, the module searches for the two files closest to the actual simulation time and reads the emissions which are necessarily given in kg m^2 s^{-1}. The emissions are then interpolated to the simulation time between both momentarily selected files. In a final step the emissions are converted to mass mixing ratio (MMR) and, as all emissions in ART, are added to the actual MMR of the corresponding tracers at the lowest model level. While the MMR of the tracers is used for internal computations, the output is given in volume mixing ratio (VMR) in mol mol^{-1}. The detailed workflow of the emissions module in ICON-ART is shown in Figure 3.2.

Some steps within this workflow are of a high importance for this work, e.g. the interpolation to simulation time which comes into play in the methods Section 4.1. In Section 4.2 we will modify some parts in the pre-processing and show a new way how raw data can be remapped to ICON grids. An important issue, not only for this work, is the question of how to implement text based information like metadata of tracers to the program code. Within ICON and ART the eXtensible Markup Language (XML, see W3C) is used, a text based format with the ability to store and transport data in a structured way. There are some rules the user has to follow when using XML, e.g. that only one root-element is allowed and the mandatory type (`char`, `int` or `real`) each tag needs. The advantages of the usage of XML are a full flexibility, direct access, control mechanisms and data type distinction (Schröter et al., 2018).
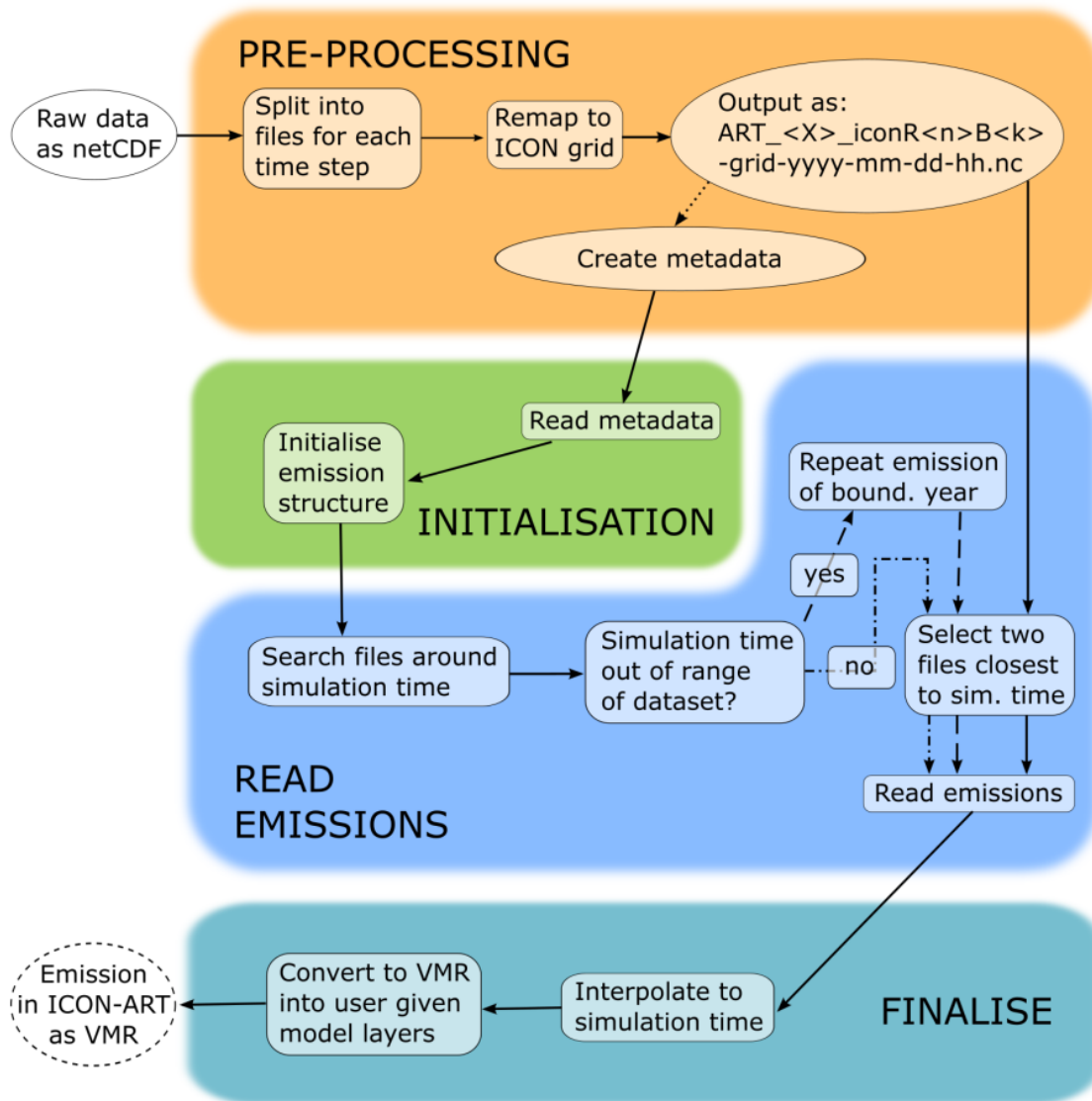
Figure 3.2: Flow chart of the process from the external netCDF emission data with regular grid and emission data as mass flux density to the emission as VMR in ICON-ART. The process can be separated into four steps: pre-processing, initialisation, read emissions and finalising the module. Pre-processing before the run of ICON-ART is necessary, whereas the other processes are included in ICON-ART. Ellipses depict files while rectangles stand for processes. The different arrow lines illustrate either the interaction with the remapped netCDF data set which has to be performed by the user in the pre-processing step (dotted), the "no" path (dotted and dashed) or the "yes" path (dashed). The Figure is taken from Weimer et al. (2017).

The following example shows how metadata of tracers are stored within ICON-ART. The tag <chemtracer> under the root-element <tracers> identifies the tracer with the name TRCH4, which is methane. The other tags denote metadata like the unit of the tracer, the molecular weight, the atmospheric lifetime, the chemistry setup or the initialisation method which is used.

```
<tracers>
 <chemtracer id="TRCH4" full="FALSE" chemtr="TRUE">
  <tag001 type="char"> chemtr </tag001>
  <mol_weight type="real"> 1.604E-2 </mol_weight>
  <lifetime type="real"> 25920000 </lifetime>
  <transport type="char"> stdchem </transport>
  <unit type="char"> mol mol-1 </unit>
  <c_solve type="char"> OH </c_solve>
  <products type="char"> TRCO </products>
  <emiss_ANT type="char" inum_levs="1"> CH4_ANT_EDGAR432-monthly </emiss_ANT>
  <emiss_BBE type="char" inum_levs="1"> CH4_BBE_GFED3 </emiss_BBE>
  <emiss_BIO type="char" inum_levs="1"> CH4_BIO_MEGAN-MACC </emiss_BIO>
  <init_mode type="int"> 1 </init_mode>
  <init_name type="char"> CH4 </init_name>
 </chemtracer>
</tracers>
```

Important XML-tags related to the emissions module of ICON-ART are `<emiss_ANT>`, `<emiss_BBE>` and `<emiss_BIO>`. Within these tags the emissions metadata are stored, e.g. `CH4_ANT_EDGAR432-monthly`. The characters between the underscores denote the chemical tracer methane, the anthropogenic emission source type and the emission inventory EDGAR4.3.2 monthly, where the remapped raw data are from.

Here, we introduced an emissions module in ICON-ART with the ability to integrate global 2-dimensional area emissions on the lowest model level of the triangular grid. Moreover, for the studies and the showcase presented in this work we need an implementation of emissions which is more spatiotemporal flexible, especially when it comes to pointsources with various source strengths, alternating heights and different start and end times. The next Section 3.3 will focus on a solution to this problem, the pointsource module of ICON-ART.

3.3 The pointsource module

Pointsources can be added to ART following the given XML-structure as shown in the example below. Beside the `id` which is necessary to define the name of the pointsource, the information about longitude and latitude (in degrees) is mandatory to indicate the location of the source. In our example we specify the `substance` as a dummy tracer called `cstracer` with an example `source_strength` of 42 given in `kg s-1` which is specified as the `unit`. The `height` of 10 m is chosen because it is the middle of the lowest model level which has a thickness of 20 m. The two final and mandatory tags for the `startTime` and `endTime` are given in the ISO-8601 format. A detailed description of the options within an ICON-ART pointsource XML can be found in Table 3.2.

```
<sources>
 <pntSrc id="Campus_Nord_Office">
  <lon type="real"> 8.435538 </lon>
  <lat type="real"> 49.095056 </lat>
  <substance type="char"> cstracer </substance>
  <source_strength type="real"> 42 </source_strength>
  <height type="real"> 10. </height>
  <unit type="char"> kg s-1 </unit>
  <startTime type="char"> 2018-09-01T00:00:00 </startTime>
  <endTime type="char"> 2021-12-31T23:59:00 </endTime>
 </pntSrc>
</sources>
```

XML-files like this will be of high importance later in this work, where the XML-generator will be introduced to process a high amount of multi-dimensional data to pointsources (see Section 4.3.4).

The pointsource module of ART reads the given input and then converts and adds the fluxes to the atmospheric values. Therefore, first of all an emission factor emiss_fct is calculated through the given source strength as shown in Equation 3.9. The variable cell_area in the denominator stands for the area in m^2 of the triangular ICON grid cell in which the pointsource is located. The parameter dtime in seconds is the basic time step of ICON. As the source strength is given in $kg\ s^{-1}$, dtime is necessary to define the correct emission flux for the actual time step. In our simulations this basic computation time step is 6 minutes and therefore dtime is 360 s. More information about computational time steps in ICON can be found in Prill et al. (2019). The unit of the emission factor emiss_fct is $kg\ m^{-2}$.

Table 3.2: Overview and detailed description of the options that can be set in an ICON-ART pointsource XML file. Table is taken and adapted from Muser et al. (2018).

pntSrc id	Specification of the pointsource name. This `id` is not used in the ICON-ART code and only serves for a better understanding of the XML file and the context. It is also possible to have two pointsources with the same `id`.
substance	The name of the substance to which the emission is added. This has to be the very same name as specified in `cart_passive_xml` or `cart_chemistry_xml`.
lon	Geographical longitude in degrees of pointsource given by a value from -180 to 180.
lat	Geographical latitude in degrees of pointsource given by a value from -90 to 90.
source_strength	The source strenght of the pointsource in the unit that is specified below.
height	Specification of the pointsource height in meters above ground.
unit	The pointsource unit can be one of the following: `kg s-1`, `kg h-1`, `Bq s-1`, `Bq h-1`, `s-1`, `h-1`.
startTime	Start time of pointsource emission in the format `YYYY-MM-DDTHH-MM-SS`.
endTime	End time of pointsource emission in the format `YYYY-MM-DDTHH-MM-SS`.

$$\text{emiss\_fct} \quad = \quad \frac{\text{source\_strength}}{\text{cell\_area}} \cdot \text{dtime} \qquad \left[\frac{\text{kg}}{\text{m}^2}\right] \tag{3.9}$$

The emission has now been transformed from a pointsource to a 2-dimensional emission in a triangular grid cell. As a next step the above calculated emission factor is added to the actual tracer value of the grid:

$$\text{tracer} \quad = \quad \text{tracer} \quad + \quad \frac{\text{h} \cdot \text{emiss\_fct}}{\rho \cdot \text{dz}} \qquad \left[\frac{\text{kg}}{\text{kg}}\right] \tag{3.10}$$

Equation 3.10 shows how emiss_fct is multiplied with a height factor h which is a number without a unit. Also the density of air ρ in kg m^{-3} and the height of the corresponding ICON layer dz in meters come into play. In our case all the pointsources are located in the middle of the lowest model level with a height of 20 m.

With the pointsource module in ICON-ART we are able to convert 0-dimensional fluxes of emissions to MMR on the triangular grid.

3.4 Atmospheric chemistry

In this section we will introduce the main chemistry setup of ICON-ART which is used for the simulations within this work. It is a simplified OH-chemistry mechanism that calculates a diagnostic steady-state OH number concentration as

$$
[\text{OH}] \quad = \quad \frac{2\,[\text{O}(^1\text{D})]\,k_{\text{H}_2\text{O}}\,[\text{H}_2\text{O}]}{k_{\text{OH+CH}_4}\,[\text{CH}_4] + (k_{\text{CO},1} + k_{\text{CO},2})\,[\text{CO}]}
\tag{3.11}
$$

where $\text{O}(^1\text{D})$ is an oxygen atom in excited state produced by the photolysis of ozone and is calculated according to a simplified model as introduced by Jacob (1999). This results in the following formula:

$$
[\text{O}(^1\text{D})] = \frac{J_{\text{O}_3}[\text{O}_3]}{k_{\text{O}_2}\,[\text{O}_2] + k_{\text{N}_2}\,[\text{N}_2] + k_{\text{H}_2\text{O}}\,[\text{H}_2\text{O}]}
\tag{3.12}
$$

The ozone concentration is derived from the LINOZ scheme (McLinden et al., 2000) and the H_2O concentration represents the water tracer of ICON-ART `qv`. The reaction rates k within the above shown equations are calculated based on Sander et al. (2011). The photolysis rate J_{O_3} is calculated by the external CloudJ module (Prather, 2015) in ICON-ART. For the simplified OH chemistry the species CH_4 and CO are mandatory chemical tracers within the corresponding simulation. With the above presented OH concentration, the depletion of the following species can be calculated: CO (required), CH_4 (required), CH_3COCH_3, C_2H_6, C_3H_8, C_5H_8, SO_2, OCS, DMS, NH_3, NO_2. Due to computational limitations the simplified OH chemistry is only active for a threshold of more than 1 ppmv of methane. Below this value the species are depleted based on their atmospheric lifetime (Weimer et al., 2017). More details about the simplified OH chemistry mechanism can be found in Weimer et al. (2017).

As mentioned in Section 3.2, we will now come back to some of the XML-tags that are relevant for atmospheric chemistry in ICON-ART and which are used for the files

within the emissions module. The most important one is the tag `c_solve`, where the chemistry mechanism is defined with `OH`. If neither the simplified OH-chemistry nor any other mechanism is applicable for a species, one can also use `lt` for a simple lifetime based parametrisation.

The tag `products` takes a semicolon-separated list with the products of a chemical reaction of the species. For example if the depletion of tracer X results in 90% Y and 10% Z, the corresponding XML-tag should look like this:

```
<products type="char"> 0.9*Y; 0.1*Z </products>
```

The XML-tag `lifetime` contains the atmospheric lifetime of a tracer given in seconds. The lifetime of all substances that are simulated within the ICON-ART simulations of this work have been adjusted according to the most common literature values (see Table 3.3).

Table 3.3: Overview of ICON-ART tracers with chemical formula, name, the atmospheric lifetime, the lifetime value in seconds as it is implemented in the XML file and the literature reference.

Species	Name	Lifetime	XML value [s]	Literature
$CHBr_3$	bromoform	24 d	2073600	Rieger et al. (2015)
CH_2Br_2	dibromomethane	123 d	10627200	Rieger et al. (2015)
CH_3COCH_3	acetone	20 d	1728000	Weimer (2015)
CH_4	methane	9.1 yr	286977600	Hayman et al. (2014)
C_2H_6	ethane	58 d	5011200	Hodnebrog et al. (2018)
C_3H_8	propane	13 d	1123200	Hodnebrog et al. (2018)
C_5H_8	isoprene	144 min	8640	Weimer (2015)
CO	carbon monoxide	60 d	5184000	Ehhalt et al. (2001)
CO_2	carbon dioxide	100 yr	3153600000	Albritton et al. (2001)
HNO_3	nitric acid	6 h	21600	Day et al. (2008)
H_2SO_4	sulfuric acid	30 min	1800	Fiedler et al. (2005)
NH_3	ammonia	1 d	86400	Pinder et al. (2008)
NO_2	nitrite	3 d	259200	Ehhalt et al. (2001)
NO_y		3 d	259200	Ehhalt et al. (2001)
N_2O	nitrous oxide	150 yr	4730400000	Wypych (2017)
O_3	ozone	18.25 d	1576800	Ehhalt et al. (2001)
SO_2	sulfur dioxide	14 d	1209600	von Glasow et al. (2009)

4

Methods for the adjustment of emission inventories

In Chapter 4 we present the methods that were developed within this work to adjust missing emissions in atmospheric inventories. Three different approaches were developed including

1) a straight forward **up-scaling** method by the implementation of additional pointsources (see Section Section 4.1),

2) a **distribution of reported data** to derive the new gridded emission product EDGAR+ (see Section 4.2),

3) WALLACE, a new method for the accurate **quantification of emissions** based on satellite measurement data (see Section 4.3).

In Section 4.4 we outline the experimental design of this study and wrap up the contents of the last Chapters.

4.1 Up-scaling EDGAR emissions

The first and most simple approach is to adjust the missing emissions in the NSR by equally distributing the total amount of methane emissions in the area encompassing pointsources that represent the offshore platforms as listed in OSPAR (2017). As EDGAR consists of monthly means and the simulation is running for one complete year it would lead to errors if we would take the emissions of just one of the monthly means for the pointsources strength. Another possibility is to use the mean value of all 12 monthly means, but that would not be consistent either as ICON uses an interpolated emission flux for each month as follows: For the emission flux of month n ICON uses the mean of

this and the following month $n + 1$ and so on, what means that the data is valid for the 1st of each month.
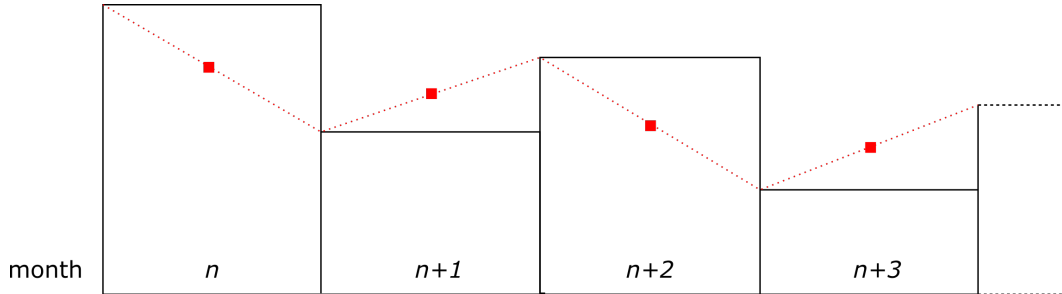
Figure 4.1: Illustration of interpolated means. For the emission flux of month n ICON uses the mean of this and the following month $n + 1$ and so on. With respect to this the correct mean value is calculated as the mean of all the interpolated means for each month to minimize the error of the new pointsource emissions over the whole simulated year.

With respect to this, the mean value is calculated as the mean of all the interpolated means for each month to minimize the error of the pointsource emissions over the whole simulated year. This method is illustrated in Figure 4.1.

As mentioned before, the total sum of the emissions of all triangles in the NSR is equally distributed to all 914 active platforms. For the species methane, ethane, propane and carbon monoxide, which are all included in EDGAR, we use this method to determine the source strength of the platforms. An overview of these emission fluxes is given in Table 4.1.

Table 4.1: Overview of the emission fluxes per pointsource derived from the EDGAR dataset by calculating the interpolated monthly means.

species	source strength in kg s^{-1}
CH_4	0.0223
C_2H_6	0.00062
C_3H_8	0.00052
CO	0.00036

4.2 The EDGAR+ emission product

The second approach we are taking to adjust the missing trace gas emissions in the NSR is to create the new gridded product EDGAR+ based on three main components. First, the original EDGAR dataset as introduced in Section 2.3.2 and taken for the adjustment in Section 4.1. Second, we use the same information about the locations of oil and gas platforms from OSPAR (2017) as presented in Section 2.3.3 and also used in the Section before. The third component is taken from OSPAR (2019), a report on Discharges, Spills and Emissions from Offshore Oil and Gas Installations for the year 2017. This includes reported data about methane emissions from the contracting countries Denmark, Germany, Ireland, the Netherlands, Norway, Spain and the United Kingdom.

The first task on the way to our new EDGAR+ product is to get a better understanding of the EDGAR inventory and the emission sectors of which it is composed. For the NSR there are three different sectors which contain emissions over water in our study area. These are the sectors for fuel exploitation (PRO), shipping (SHIP) and aviation cruise (CRS) as displayed together with the total sum of emissions (SUM) in Figure 4.2. For the species CO, C_2H_6 and C_3H_8 see Appendix A Figures A.1, A.2 and A.3, respectively. For the preparation of EDGAR+ we need to answer a few basic questions and do some preprocessing work. We first need to know which platform belongs to which country. This question is answered by OSPAR (2017), the dataset we introduced in Section 2.3.3. See Figure 4.3 (a) for a visualisation. From the same OSPAR dataset we then calculated the number of platforms in each pixel (see Figure 4.3 (b)). Furthermore we use OSPAR (2019) to derive the emission flux per platform per country. Together with the information of how many platforms are in each pixel we get the the new emission value $v_{new}(i)$ for pixel i as displayed in Figure 4.3 (c). Before we can add the new emission value to the EDGAR grid, we need to subtract the actual emissions of sector PRO from the SUM. As no original proxy values are available, we use the locations of sector PRO from carbon monoxide in EDGAR (see Appendix A Figure A.1 and Figure 4.4 (a)) for this subtraction. The values of SUM without PRO at platforms are displayed in Figure 4.4 (b). Finally the new emissions are added, including sectors CRS and SHIP as background values at the locations of the platforms. The result is EDGAR+ (see Figure 4.4 (c)), a new gridded product for methane in the NSR, which is calculated as follows:

$$v_{edgar+}(i) = \begin{cases} v_{sum}(i), & \text{if pixel i does not contain a platform} \\ v_{new}(i) + v_{crs}(i) + v_{ship}(i), & \text{if pixel i contains a platform} \end{cases}$$

The newly developed methane from EDGAR+ has a reasonable order of magnitude and is similar to the original EDGAR emissions with the main difference, that the methane fluxes in the southern part of the NSR are now adjusted. It is noticeable that EDGAR+ smoothes the emission peaks especially at about 61 °N. Also the spatial distribution is different in our new product, where the emissions are more discrete compared to EDGAR. This is mainly caused by the definition of how the emissions are distributed and due to the fact that more detailed proxy data was used for the original EDGAR dataset. More information about the EDGAR dataset and its proxy data can be found in Section 2.3.2 and in Janssens-Maenhout et al. (2019).

(a)

(b)

(c)

(d)
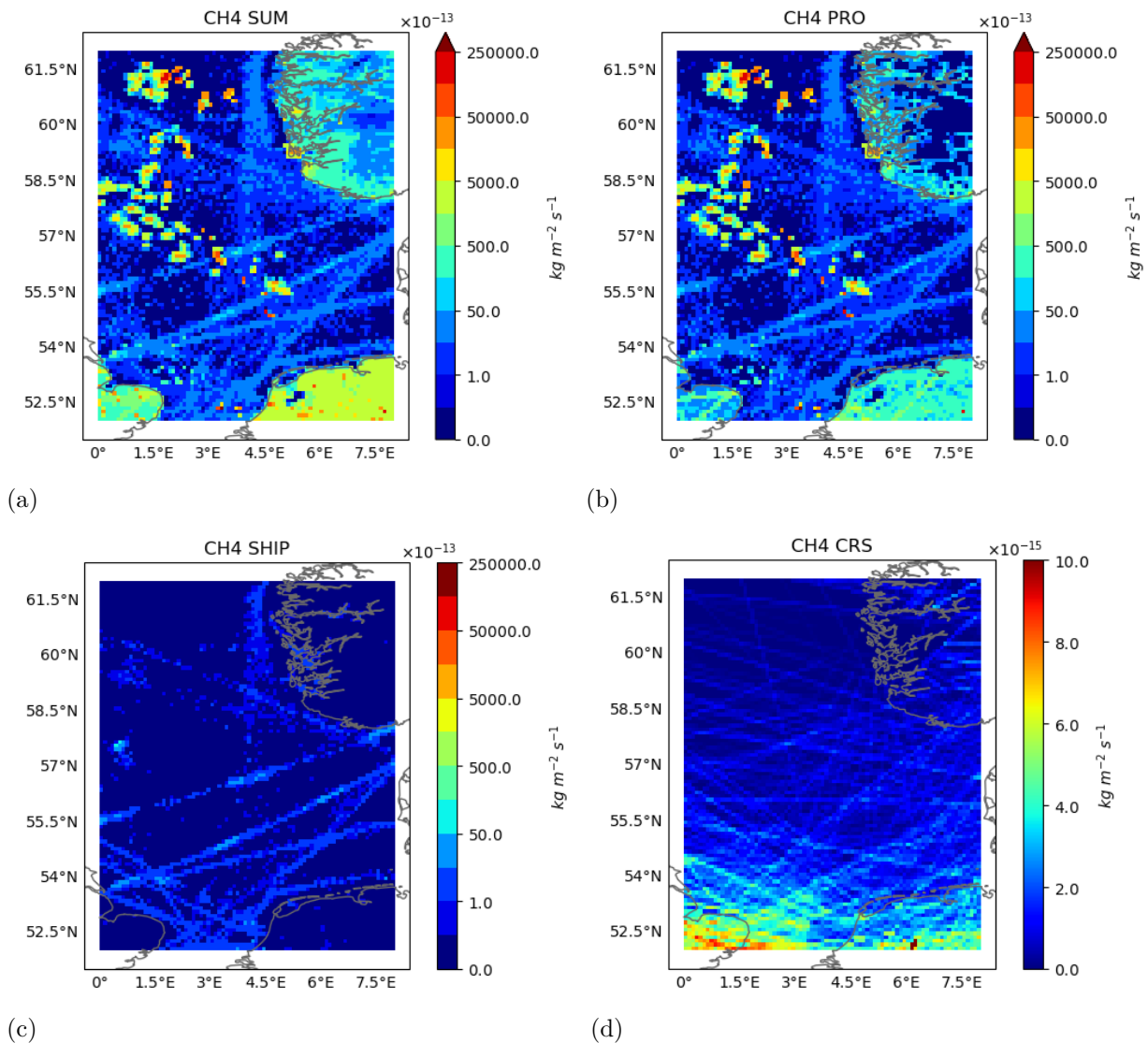
Figure 4.2: Collection of EDGAR sectors with methane emissions over water in the NSR. Displayed are SUM (a) and the sectors PRO (b), SHIP (c) and CRS (d). Note the smaller scale of the CRS sector.

(a)

(b)

(c)
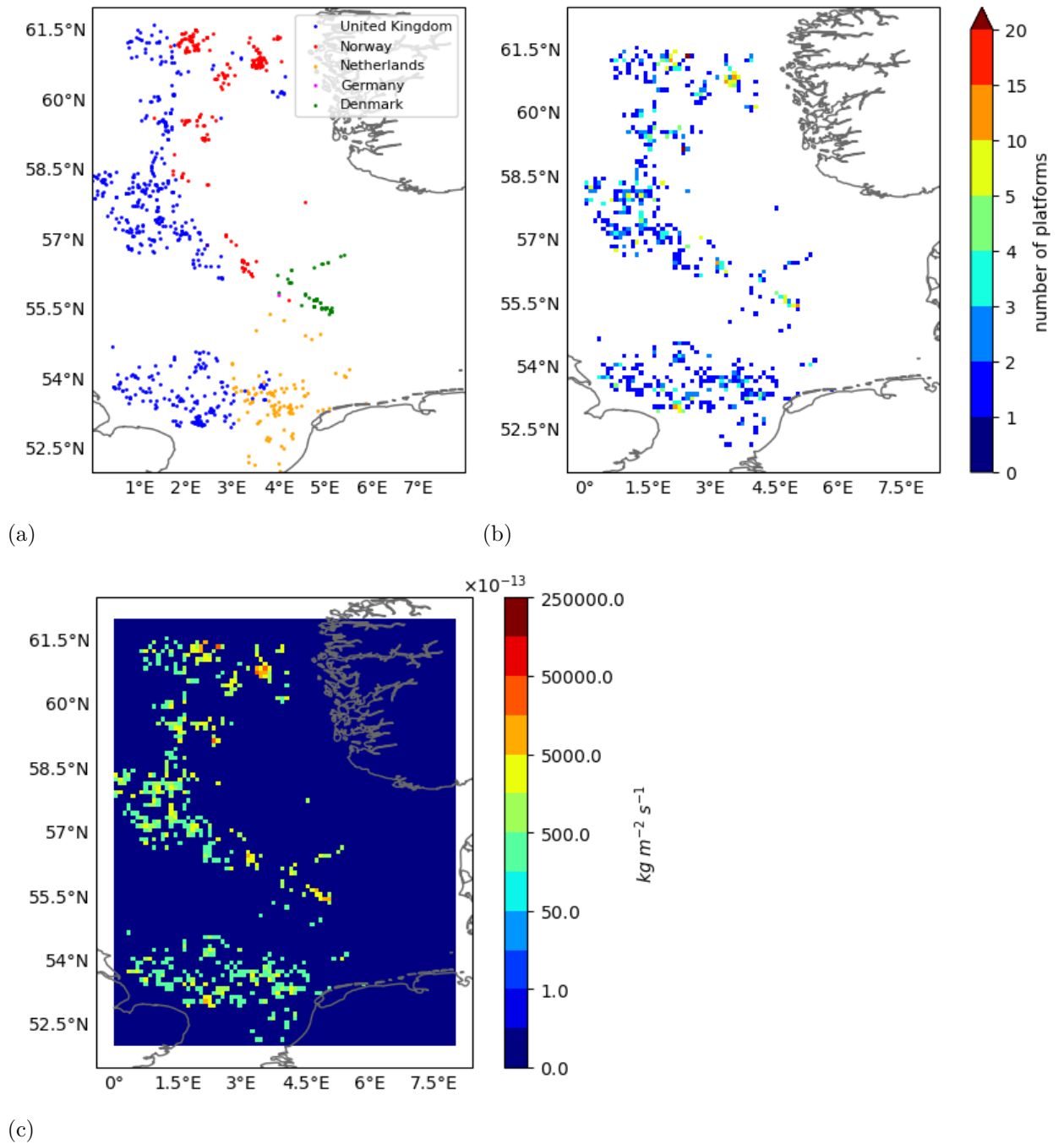
Figure 4.3: Preprocessing of EDGAR+, part I. Displayed are the platforms with information about the countries (a) and how many platforms are in each pixel (b). From these information and the emission values of OSPAR (2019), the new emission values (c) are calculated.

(a)

(b)

(c)
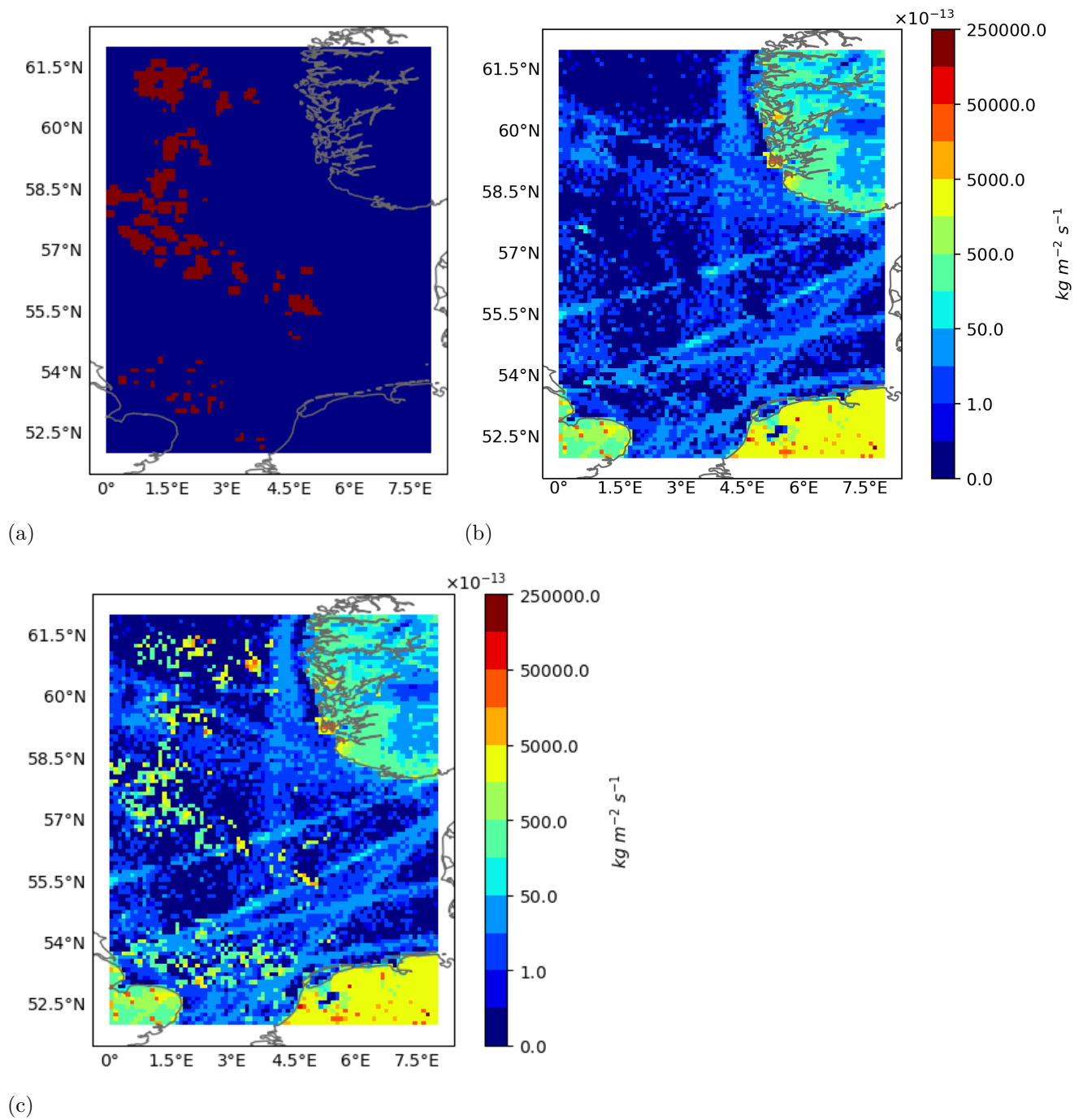
Figure 4.4: Preprocessing of EDGAR+, part II. Displayed are the locations of the platforms (a) which are added to the SUM without the emissions from sector PRO (b). The result is EDGAR+ (c), a new gridded emission product for methane in the NSR.

As OSPAR (2019) does not contain information about CO, C_2H_6 and C_3H_8 we developed a new method to derive their missing emissions starting with our new EDGAR+ CH_4 product. Therefore, we use a special ability of the original EDGAR dataset, namely the fact that the quotients of methane and the three other species appear as clusters. These clusters or groups are not random but specific for each of the countries, which is clearly displayed by the different colors in Figures 4.5 (a), (b) and (c) for the quotients of methane and carbon monoxide, ethane and propane, respectively.

(a)

(b)

(c)
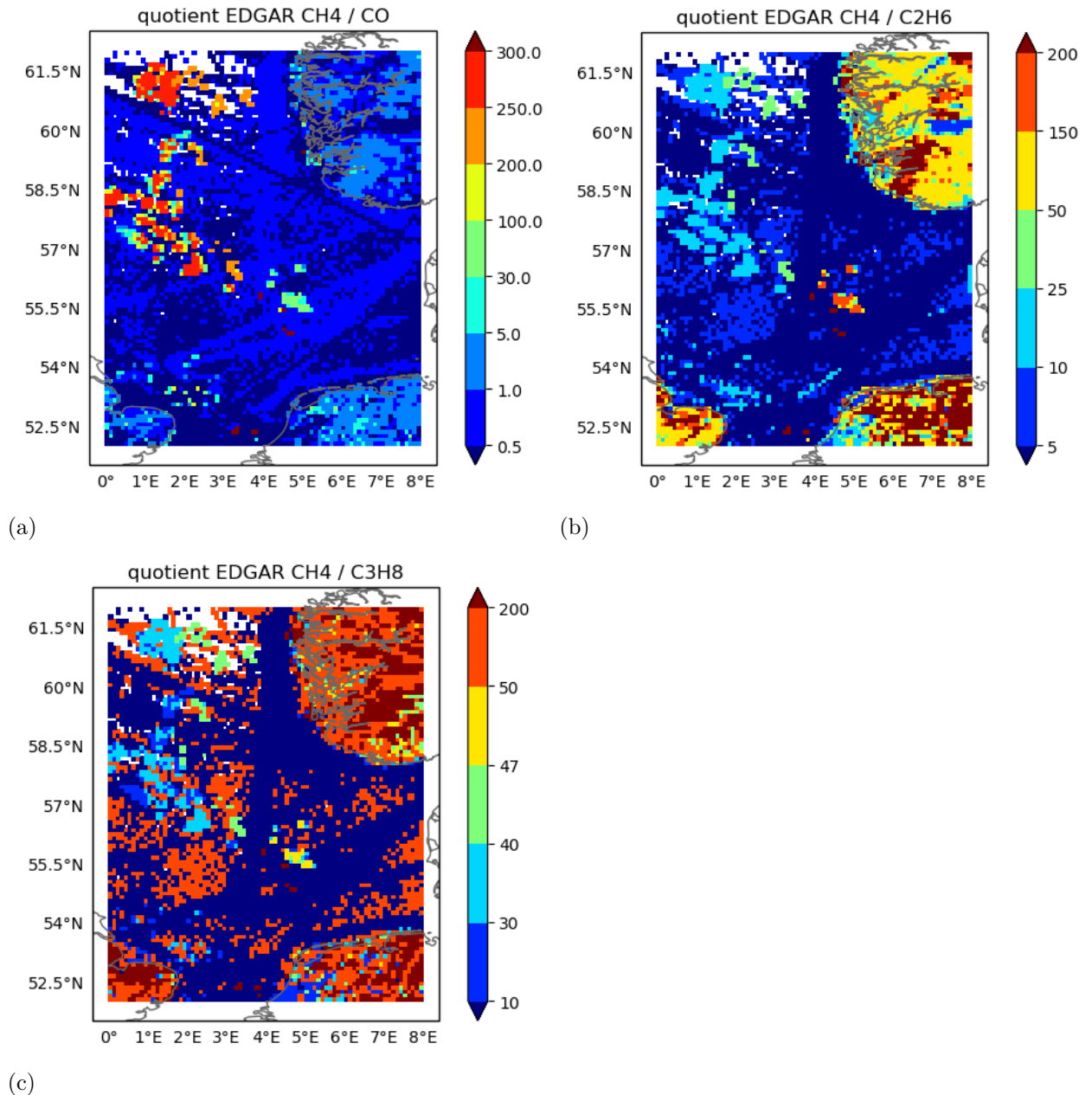
Figure 4.5: Quotients of methane with carbon monoxide (a), ethane (b) and propane (c). The colors show that the quotients come within nation-specific clusters.

We define nation-specific coefficients (NSC) from the quotients which we will use to convert methane from EDGAR+ to carbon monoxide, ethane and propane emission fluxes. The NSC are calculated as follows:

- The **median of quotients** at pixels with a platform is used.

- Only the **region between 55 °N and 62 °N** is taken because there are no platform emissions below this in the original EDGAR dataset.

- The **background values** and noise over sea are **masked** as follows:

  - $0 < CH_4/CO < 1$

  - $0 < CH_4/C_2H_6 < 10$

  - $10 < CH_4/C_3H_8 < 50$

This leads us to the following matrix with NSC (see Table 4.2).

Table 4.2: Matrix with nation-specific coefficients for EDGAR+. Germany and the Netherlands are given the mean value of the other countries because there are too less platforms available in the selected area.

	CO	C_2H_6	C_3H_8
DEN	0.022	0.005	0.021
GER	0.005	0.013	0.024
NED	0.005	0.013	0.024
NOR	0.004	0.033	0.022
UK	0.003	0.043	0.033

Displayed are the species on the x-axes and countries on the y-axes. To get the new emission flux for species x of country y we simply insert the values into the following equation:

$$v_{new}(x, y) = v_{new}(CH_4) \cdot NSC(x, y)$$

With these NSC the new EDGAR+ emission fluxes for CO, C_2H_6 and C_3H_8 are derived from the new EDGAR+ CH_4 values. A summary of the new EDGAR+ emission fluxes for all four species can be found in Appendix B. This gridded product is then implemented as emissions into ICON-ART as described in Section 3.2. EDGAR+ is the second of three approaches to adjust missing emissions in the NSR which we will evaluate in Chapter 5.

4.3 The WALLACE workflow

The new and innovative workflow package WALLACE (**W**orkflow for the **A**djustment of **L**ow **L**evel **A**tmospheric **C**ompounds and **E**missions) builds the third and most complex approach to quantify and adjust missing emissions of methane in the NSR, based on satellite measurement data. A simplified overview of the WALLACE workflow is displayed in Figure 4.6. For a detailed flow chart see Section 4.3.5 and Figure 4.13.
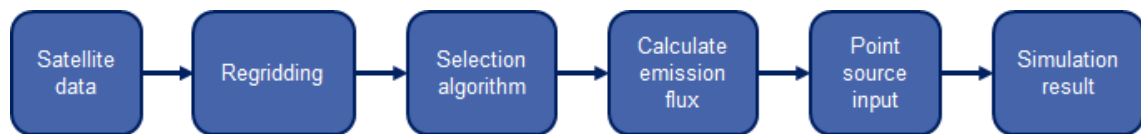
Figure 4.6: A simplified overview of the workflow package WALLACE.

WALLACE consists of four python based programs that all focus on different tasks in the workflow. The Sentinel-5P Level 3 Processor (see Section 4.3.1) focuses on the regridding of unstructured satellite measurement data, followed by a complex selection algorithm, the Pattern Algorithm, which highlights emission hotspots in areas with high background noises (see Section 4.3.2). With the Source Pixel Method (see Section 4.3.3), which we adapt from van Damme et al. (2018), and the NSC of EDGAR+ introduced in Section 4.2 the step from concentrations in the atmosphere to emission fluxes of the species is taken. The values derived from the before mentioned methods need to be processed to pointsource XML files as emission input for the ICON-ART model as described in Section 3.3. Following the four components of WALLACE are explained and evaluated in detail. In Section 4.3.5 the WALLACE workflow is applied to the NSR for the adjustment of emissions.

4.3.1 Sentinel-5P Level 3 Processor

The Copernicus Sentinel-5P (S5P) mission is a collaboration between the European Space Agency (ESA) and the Netherlands Space Office (NSO). This air quality and atmospheric chemistry monitoring mission aims to track changes in the composition of our Earths atmosphere and replaces instruments like SCIAMACHY and the Envisat satellite as both came to the end of their lifetimes (Kramer, 2020). The S5P satellite was launched on October 13, 2017 (09:27 GMT) and has an altitude of 824 km with an orbit time of 101 minutes and a repeat cycle of 17 days or 227 orbits. It carries the TROPOspheric Monitoring Instrument TROPOMI, an advanced multispectral imaging spectrometer that scans

trace gases like carbon monoxide, formaldehyde, methane, nitrogen dioxide, ozone and aerosols in the atmosphere with a swath width of 2600 km and delivers much information and data on these substances that affect our climate and the air quality (Kramer, 2020). Figure 4.7 shows an illustration of the S5P satellite with the TROPOMI spectrometer.

Figure 4.7: Illustration of the S5P satellite. The Figure is taken from Kramer (2020).

An overview of the different data products delivered by TROPOMI can be found in Table 4.3. The most important product for this work is Level 2 data as it delivers geolocated total columns of the gases (ESA, 2020).

Table 4.3: Overview of TROPOMI data products (ESA, 2020).

product	description
Level-0	Time ordered raw satellite telemetry without temporal overlap including spectrometer data, satellite position and altitude such as metadata. Level-0 data are not provided to the public.
Level-1B	Geolocated and radiometrically corrected top of the atmosphere Earth radiances in all spectral bands
Level-2	Geolocated total columns of carbon monoxide, formaldehyde, methane, nitrogen dioxide and ozone, tropospheric columns and vertical profiles of ozone such as cloud and aerosol information

A problem that comes up in working with Level 2 data is, that it uses an unstructured grid. The measurements are captured as parallelograms with different areas only delivering the latitude and longitude of the center of each parallelogram. Their size depend on the location in the measurement swath from smaller parallelograms near the middle and bigger ones near the edges of a swath (SPA, 2019). For a usage of the TROPOMI data and comparing them to databases like EDGAR or ICON-ART model output we need the data in a regular latitude/longitude grid, so called Level 3 data. To address the requirement of processing Level 2 to Level 3 data, we developed the Sentinel-5P Level 3 processor, a *python*-based program which generates our own and new Level 3 product as shown in the scheme in Figure 4.8. The unstructured parallelograms are displayed in black with their centers as circles. The red squares represent the new structured grid with regular latitudes and longitudes. Each center of the unstructured parallelograms of the Level 2 data is allocated to exactly one of the Level 3 structured grid centers by first finding the next latitude and then the next longitude that intersects with a new grid center (blue arrows).
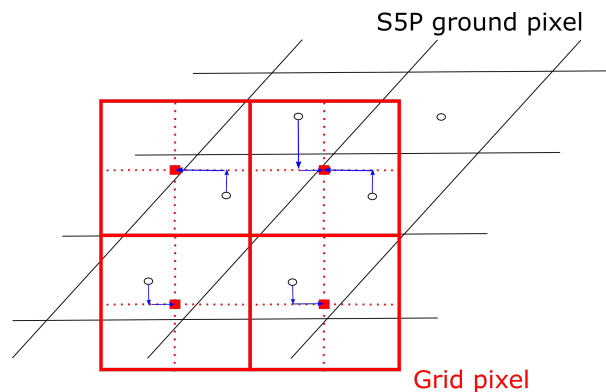
Figure 4.8: Scheme of the Sentinel-5P Level 3 processor. Each center of the unstructured parallelograms of the Level 2 data (black) is allocated to exactly one of the Level 3 structured grid centers (red) by first finding the next latitude and then the next longitude that intersects with a new grid center (blue arrows).

Figure 4.9 shows that the Sentinel-5P Level 3 processor is mapping the Level 2 data of TROPOMI in an appropriate way. The different sizes of the parallelograms due to its location in the swath can be seen in Figure 4.9 (left) where pixels over Scandinavia are smaller than the ones over Great Britain. The standard resolution of the S5P Level 3 processor is $0.1° \times 0.1°$ as visible in Figure 4.9 (middle). For coarser resolutions the interpolation routines of the Climate Data Operators (CDO, Schulzweida, 2019) are implemented in the S5P Level 3 processor and can be switched on to regrid TROPOMI measurement data on every regular grid. For an example resolution of $0.5° \times 0.5°$ see Figure 4.9 (right). As

most of the emission sources are located on the surface of the Earth, we considered the cloud fraction value qa=1 to get a cloud free picture of the TROPOMI measurements. This is why some of the regions in the example are no more represented in the Level 3 product.
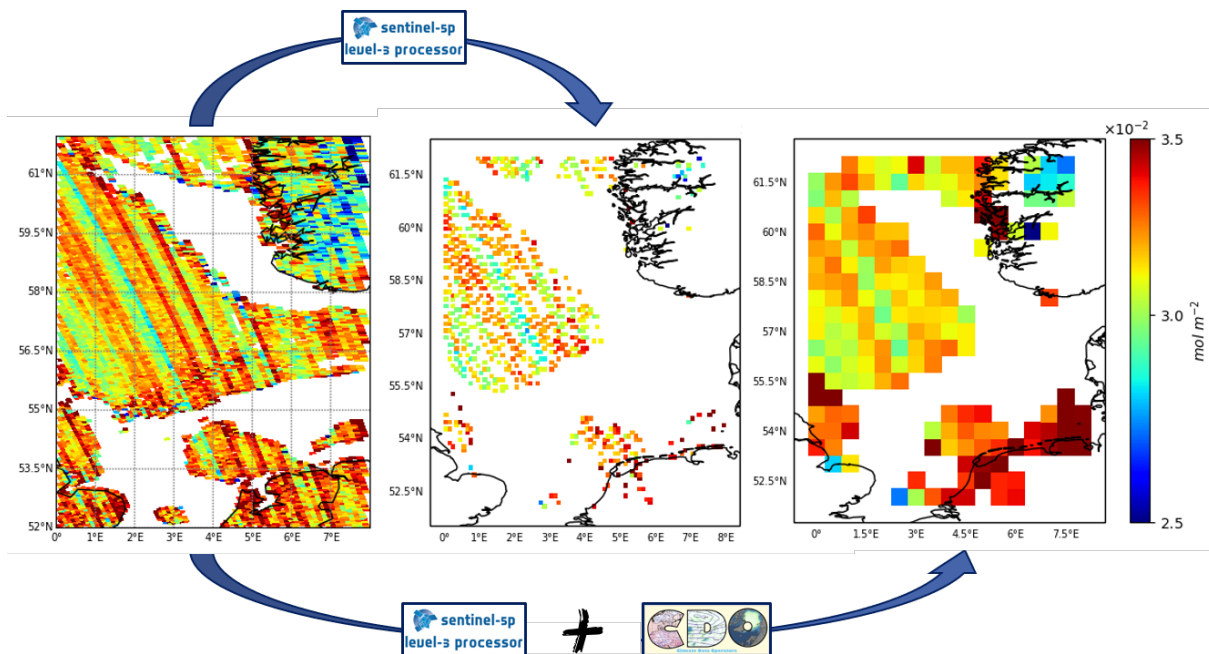
Figure 4.9: Comparison of Sentinel-5P Level 2 (left) and Level 3 data products with a spatial resolution of $0.1° \times 0.1°$ (middle) and $0.5° \times 0.5°$ (right). For coarser resolutions than $0.1° \times 0.1°$ the interpolation routines of CDO (Wegner, 2012; Schulzweida, 2019) are implemented in the Sentinel-5P Level 3 processor.

4.3.2 Pattern Algorithm

The objective of this section is to introduce the Pattern Algorithm, a python based command line tool that detects and isolates emission hotspots of GHGs in atmospheric datasets. Its overall goal is to separate hotspot areas within the background noise and therefore uses a completely new method including spatiotemporal proxy data and a selection algorithm. We define a structure quotient by which the algorithm decides on behalf of a threshold value whether the values of a time step in the dataset meet the requirements of the algorithm and is then used for further calculations or not. The Pattern Algorithm comes with a bunch of implemented features like an automated creation of user-specific patterns and an analysis tool to choose the optimal threshold value.

The Pattern Algorithm opens the input dataset and, due to memory and handling reasons, selects the specified variable and a rectangular area given via the latitude and longitude values of its vertices. This area, hereafter named P0, is splitted into two so called patterns, named P1 and P2. Pattern P1 contains all the cells that we assume to be part of our expected hotspot area. P2 is the complement so that P1 ∪ P2 = P0. Let $n_1 = \#P1$ and $n_2 = \#P2$ be the number of cells that belong to P1 and P2, respectively. The predefined patterns are now fix for the whole loop, only the input data changes from one timestep to another, e.g. the VMR of a chemical tracer. These data values at pixel i in P1 and at pixel j in P2 are named v(i) and v(j) with $i \in \{1, ..., n_1\}$ and $j \in \{1, ..., n_2\}$. We then define the arithmetic mean value m of a time step in P0 as:

$$m \quad = \quad \frac{\sum_{k=1}^{n_1+n_2} v(k)}{n_1 + n_2}$$

Furthermore we are now interested in the number of pixels in P1 and P2 that are above the mean value m of the whole rectangle P0. Therefore an indicator is defined which is equal to 1 if the condition v(i) > m is true and equal to 0 if not. We summarize the indicator for P1 and P2 to get the number of occurrences above the mean as shown in Equation 4.1 for P1 and in Equation 4.2 for P2, accordingly.

$$a_1 \quad = \quad \sum_{i=1}^{n_1} \mathbf{1}\{v(i) > m\} \quad = \quad \sum_{i=1}^{n_1} \mathbf{1}\{v(i) > \frac{\sum_{k=1}^{n_1+n_2} v(k)}{n_1 + n_2}\} \tag{4.1}$$

$$a_2 \quad = \quad \sum_{j=1}^{n_2} \mathbf{1}\{v(j) > m\} \quad = \quad \sum_{j=1}^{n_2} \mathbf{1}\{v(j) > \frac{\sum_{k=1}^{n_1+n_2} v(k)}{n_1 + n_2}\} \tag{4.2}$$

With these technical preparations done we can define a quotient that builds the core of the actual algorithm. The so called structure quotient (sq) contains the relative number of occurrences in P1 that are above the mean value m in the numerator and the relative number of occurrences in P2 that are above m in the denominator as shown in Equation 4.3.

$$sq \quad = \quad \frac{\frac{a_1}{n_1}}{\frac{a_2}{n_2}} \quad = \quad \frac{a_1 \cdot n_2}{a_2 \cdot n_1} \quad = \quad \frac{\sum_{i=1}^{n_1} \mathbf{1}\{v(i) > \frac{\sum_{k=1}^{n_1+n_2} v(k)}{n_1+n_2}\} \cdot n_2}{\sum_{j=1}^{n_2} \mathbf{1}\{v(j) > \frac{\sum_{k=1}^{n_1+n_2} v(k)}{n_1+n_2}\} \cdot n_1} \tag{4.3}$$

with

$$i \in \{1, ..., n_1\}, \qquad j \in \{1, ..., n_2\}, \qquad k \in \{1, ..., n_1 + n_2\}$$

For each time step in the dataset the Pattern Algorithm calculates the value of sq and in principal there are three outcomes that are possible. First, the structure quotient sq is near to 1 (numerator and denominator are almost equal). Second, if there are relatively more pixels above the mean in P2 than in P1 (denominator greater than numerator), sq decreases to a value below 1. Just in case there are relatively more pixels above m in P1 than in P2, sq increases to values above 1, which is the desired outcome. As we are about to select time steps where values in P1 are significantly higher than outside, the first two alternatives are not interesting for us. Dependent on the threshold value $sq_t \in \mathbb{R}$, the Pattern Algorithm only keeps time steps with $sq > sq_t$ and drops the ones with a structure quotient smaller or equal to sq_t. The result is a subset of the original dataset that contains only time steps that fulfill the above mentioned conditions. In particular the region of pattern P1, which we assume to be a hotspot area, is highlighted.

Although the Pattern Algorithm is written in *python*, users do not need to change code if they want to apply the algorithm to their specific input. Therefore a user-friendly command line interface was implemented by using *argparse*, a *python* module that parses arguments written in the command line and links them with variables used in the source code. The *argparse* module also creates automatically generated help and error messages, e.g. when users give invalid arguments. Table 4.4 shows an overview of the command line arguments of the Pattern Algorithm together with their description.

Table 4.4: Overview of command line arguments of the Pattern Algorithm. Displayed is the short and long version of the argument, the description that also arises in the help message and the information if this argument is required for the Pattern Algorithm or not.

argument (short)	argument (long)	description	required
−i	−−indir	input directory	yes
−o	−−outdir	input directory	yes
−p	−−path_to_pattern_file	path to csv file for pattern	yes
−f	−−filename	name of output files	no
	−−llat	lower latitude boundary	yes
	−−ulat	upper latitude boundary	yes
	−−llon	lower longitude boundary	yes
	−−ulon	upper longitude boundary	yes
−l	−−lev	vertical level selection	no
−t	−−timestep	timestep in input files	no
−s	−−sq	threshold for sq	yes
−m	−−land_mask	mask land (True or False)	no

When it comes to the definition of the hotspot pattern P1, the source code comes with two advantages that are implemented. First, it is only necessary to provide a text file with comma separated values for longitude and latitude, e.g. locations of factories or offshore platforms, then the program creates the patterns itself on the basis of these data. Second, the Pattern Algorithm is able to recognize the grid resolution of the given input data and the patterns are created according to the mesh size of the individual grid. At the moment this is possible for regular grids only. Per default all land surfaces are not taken into account but users can decide if they want to have the land surface masked or not. This is implemented by the *python* module *global-land-mask* (Todd, 2020), which checks whether a point given by its latitude and longitude values is over land or sea. For the NSR land masking and the pattern used for the analysis in this section see Figure 4.10 (a) and (b), respectively.

(a)   (b)
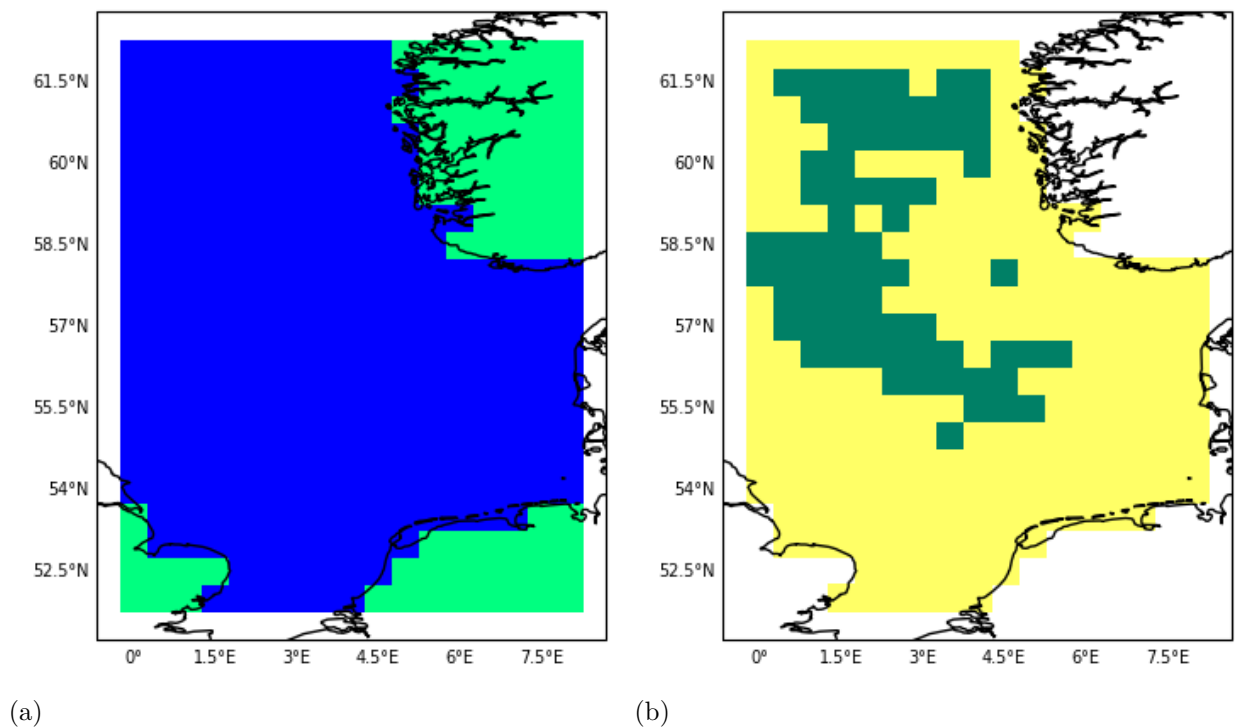
Figure 4.10: Pixels over the land surface (light green) can be masked within the
Pattern Algorithm because methane VMRs are much lower over sea
(blue) and additional noise can be avoided (a). The pixels in dark green
contain offshore oil and gas exploration platforms and therefore belong to
pattern P1 within the Pattern Algorithm, yellow pixels belong to P2.
Land masking is enabled (b).

The Pattern Algorithm program comes with a separate tool which is also usable via the command line. The so called *threshold analysis* aims to evaluate the input data in advance and provides a threshold value sq_t that is optimal for the individual given dataset. The

threshold analysis tool processes the structure quotient for each time step of the input dataset and writes a text file with mathematical parameters on the basis of which the user knows which value of sq_t to chose for an elimination of e.g. $10\,\%$ of the original set. The parameters calculated by the threshold analysis are maximum, arithmetic mean, median, upper quartile, 0.9-quantile and 0.95-quantile. With simple adjustments the user can also integrate own empirical p-quantiles that are written into the output text file.

We proof the concept of the Pattern Algorithm with ICON-ART simulation results and use simulation A2 PNTSRC (see Table 4.7) as described in Section 4.4. It consists of 730 output time steps with a 12 hour temporal resolution and platform emissions from pointsources in the NSR. As visible in Figure 4.11 (a) the annual mean of the methane VMR does not represent the platforms as emission hotspots due to transport and mixing reasons in the atmosphere, especially near the surface. Only in the northern part of the NSR slightly increased values at platform locations are visible. The Pattern Algorithm was applied on the 730 output files of the ICON-ART model with a threshold of sq=2 and it selected a total of 53 time steps, what is about $7\,\%$ of the total amount of frames. As visible in Figure 4.11 (b) the mean of the selected time steps shows a hotspot area which matches the platform locations precisely, being clearly separated from the background with high gradients at its borders between the in- and outside of the chosen pattern.

(a)   (b)
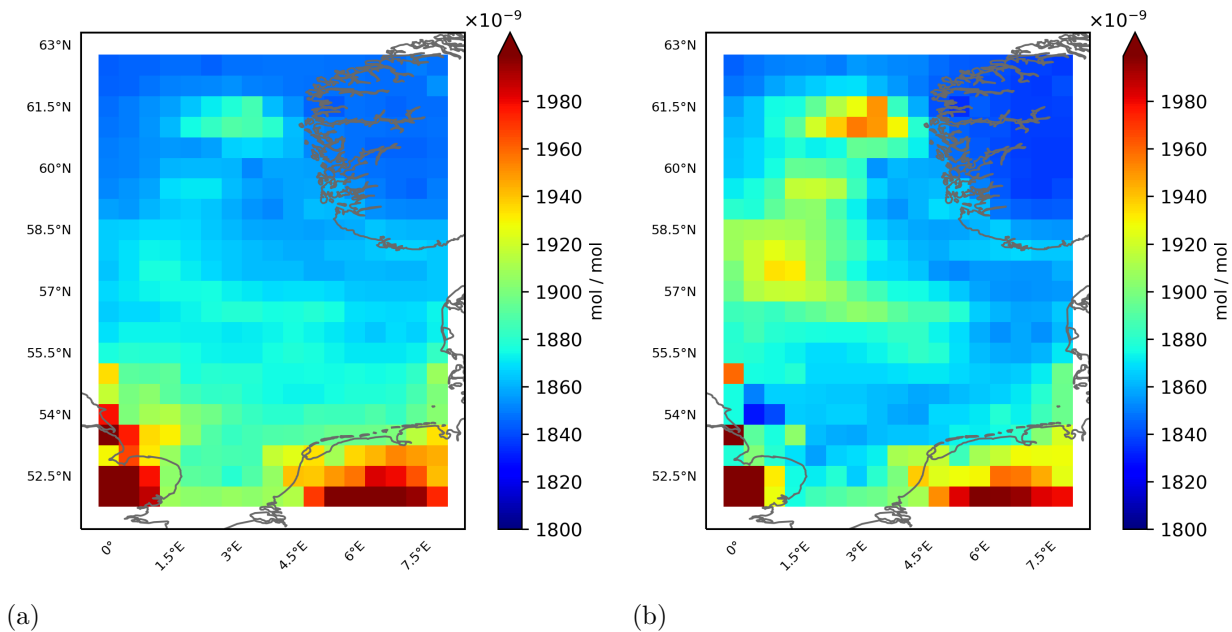
Figure 4.11: Methane VMR annual mean (a) and mean of the time steps selected by the Pattern Algorithm (b) of the ICON-ART simulation for the year 2018. Both represent the mean at the lowest model level at the surface.

For a first analysis of how good the Pattern Algorithm works we are applying the structure quotient sq on the annual mean of the ICON-ART simulation results and the mean of

the algorithm's selection of this input dataset as presented in Figures 4.11 (a) and (b), respectively. For the original annual mean of the simulation the structure quotient sq_{ori} is 0.753 and for the resulting selection sq_{res} equals 3.338, which is not only an increase of about 350 % but also pushes the value of the structure quotient of the selection result far over 1 which indicates the hotspot inside the pattern area from a mathematical point of view and following the algorithm's conception. The second approach of analysis brings another variable into play as we will have a look at the mean wind speed and direction of the annual mean and the time steps selected by the Pattern Algorithm. The North Sea is almost completely surrounded by parts of the European continent and - although the weather is mainly influenced by westerly winds - the direction and speed of winds is determined by local conditions. Due to these reasons, the component-wise annual mean wind direction and speed in the NSR computed in the ICON-ART model is balanced and no tendencies are visible (see Figure 4.12 (a)). Almost the same feature is emerging when we are looking at the component-wise wind mean of the Pattern Algorithm's selection where only some parts near the coastal areas show concrete wind directions, e.g. north-easterly winds in the English Channel (see Figure 4.12 (b)).

(a)

(b)
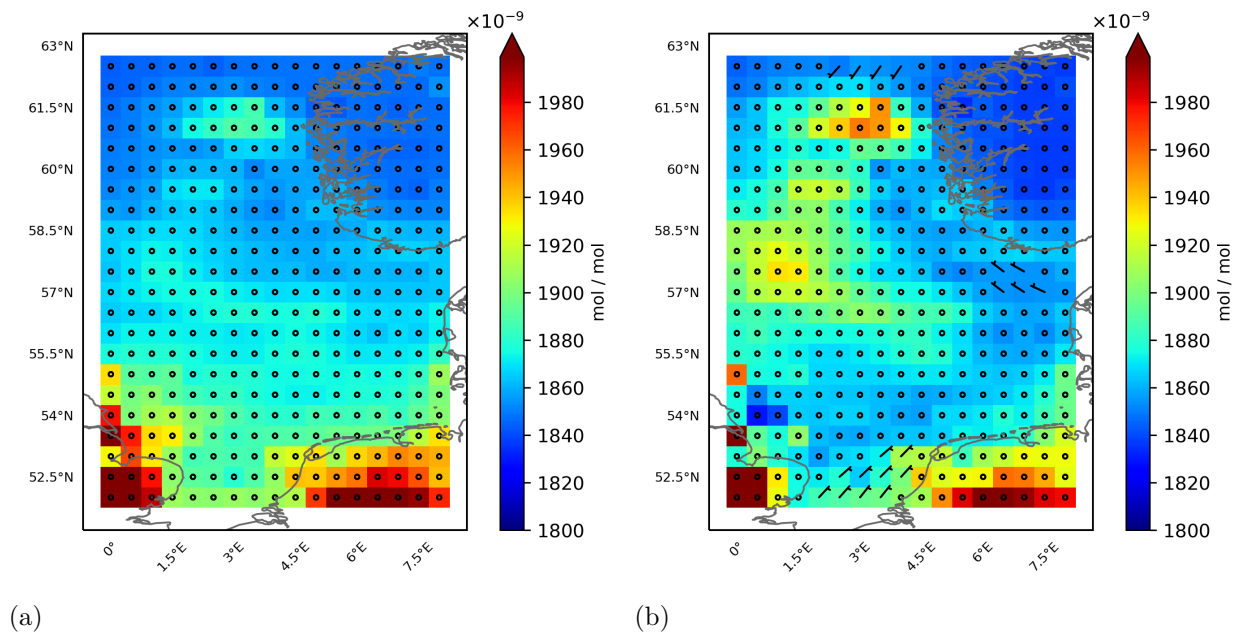
Figure 4.12: Methane VMR annual mean (a) and mean of the time steps selected by the Pattern Algorithm (b) of the ICON-ART simulation for the year 2018 together with component-wise mean wind.

The fact that the pattern algorithm selects time steps whose mean wind direction is as balanced as that of the annual mean shows that the majority of the methane in the hotspot area actually comes from the platforms implemented as pointsources in the simulation. To proof this assumption we created nine random patterns that were used as

input for the Pattern Algorithm and applied on the same ICON-ART simulation as the pattern presented in Figure 4.10 (b). The nine random patterns and their mean methane VMR together with component-wise mean wind after applying the Pattern Algorithm are displayed in Appendix C, Figures C.1 and C.2, respectively. The results show that the Pattern Algorithm works appropriately selecting time steps with high methane VMR in each corresponding P1. But decisively the usage of patterns different to the platform pattern shown in Figure 4.10 (b) lead to wind that obviously caused the high values in the random patterns. This shows, that with random patterns no hotspots are highlighted but the Pattern Algorithm just selects time steps with certain wind conditions.

4.3.3 Source Pixel Method

Our goal is to determine carbon monoxide emission fluxes from the total columns that we derived from the TROPOMI measurement data, or, more precisely, the subsets of those selected by the Pattern Algorithm. We are therefore adapting a method introduced by van Damme et al. (2018) called Source Pixel Method. To obtain the emission flux E in kg s^{-1} from the total column in mol m^{-2} we use a simple formula based on the total mass m of the substance in kg and the lifetime τ of the species in seconds.

$$E \quad = \quad \frac{m}{\tau}$$

For our experiment we used the tracer lifetimes of ICON-ART as shown in Table 3.3. To get the total mass m we take the proportion

$$m \quad = \quad M \cdot n$$

where M is the molar mass in g mol^{-1} and n the amount of substance in mol. The amount of substance n is calculated from the column value x in mol m^{-2} and the area (lenght of latitude at pixel *llat* times lenght of longitude at pixel *llon*) of the column's regular ground pixel as follows:

$$n \quad = \quad x \cdot llat \cdot llon$$

Bringing everything together the emission flux E is calculated as

$$E \quad = \quad \frac{m}{\tau} \quad = \quad \frac{M \cdot n \cdot 0.001}{\tau} \quad = \quad \frac{M \cdot x \cdot llat \cdot llon \cdot 0.001}{\tau} \tag{4.4}$$

4.3.4 XML-generator

The last part of WALLACE is the *python* based XML-generator. From the Source Pixel Method (see Section 4.3.3) we derived emission fluxes for the sources in the hotspot area that we defined and isolated from the background noise in the Pattern Algorithm (see Section 4.3.2). To make them usable for the ICON-ART model we need the XML-generator that creates pointsource XML files in the format introduced in Section 3.3. The XML-generator takes an input CSV file with the following information in its columns: Name, latitude, longitude, emission flux, unit of emission flux, start and end time of the pointsource. For more details of the input format for the XML-generator see Table 4.5. The result is an ICON-ART pointsource XML as visible in the example in Section 3.3.

Table 4.5: Input variables of the XML-generator together with the format and examples. Displayed are Name, Latitude, Longitude, Emission flux, Unit, Start and End time.

input	format	example
Name	string	'pointsource_name'
Latitude	float	5.13
Longitude	float	55.46
Emission flux	float	0.02233
Unit	string	'kg s-1' or 'kg h-1'
Start time	ISO-8601	2018-01-01T00:00:00
End time	ISO-8601	2018-12-31T23:59:59

4.3.5 Applying the WALLACE workflow

Here, we introduced the *python* programs that are part of our WALLACE workflow. Its main goal is to derive and quantify the emission fluxes of the North Sea platforms on the basis of satellite measurements. Compared to the approaches in Sections 4.1 and 4.2, the WALLACE workflow is the most complex one. Figure 4.13 displays the WALLACE workflow as we describe it in this Section. Additionally the logos of the S5P Level 3 processor (adapted from ESA (2021)), the Pattern Algorithm, the Source Pixel Method, the XML-generator (all own developments) such as the ART logo (see Prill et al. (2019)) are included.
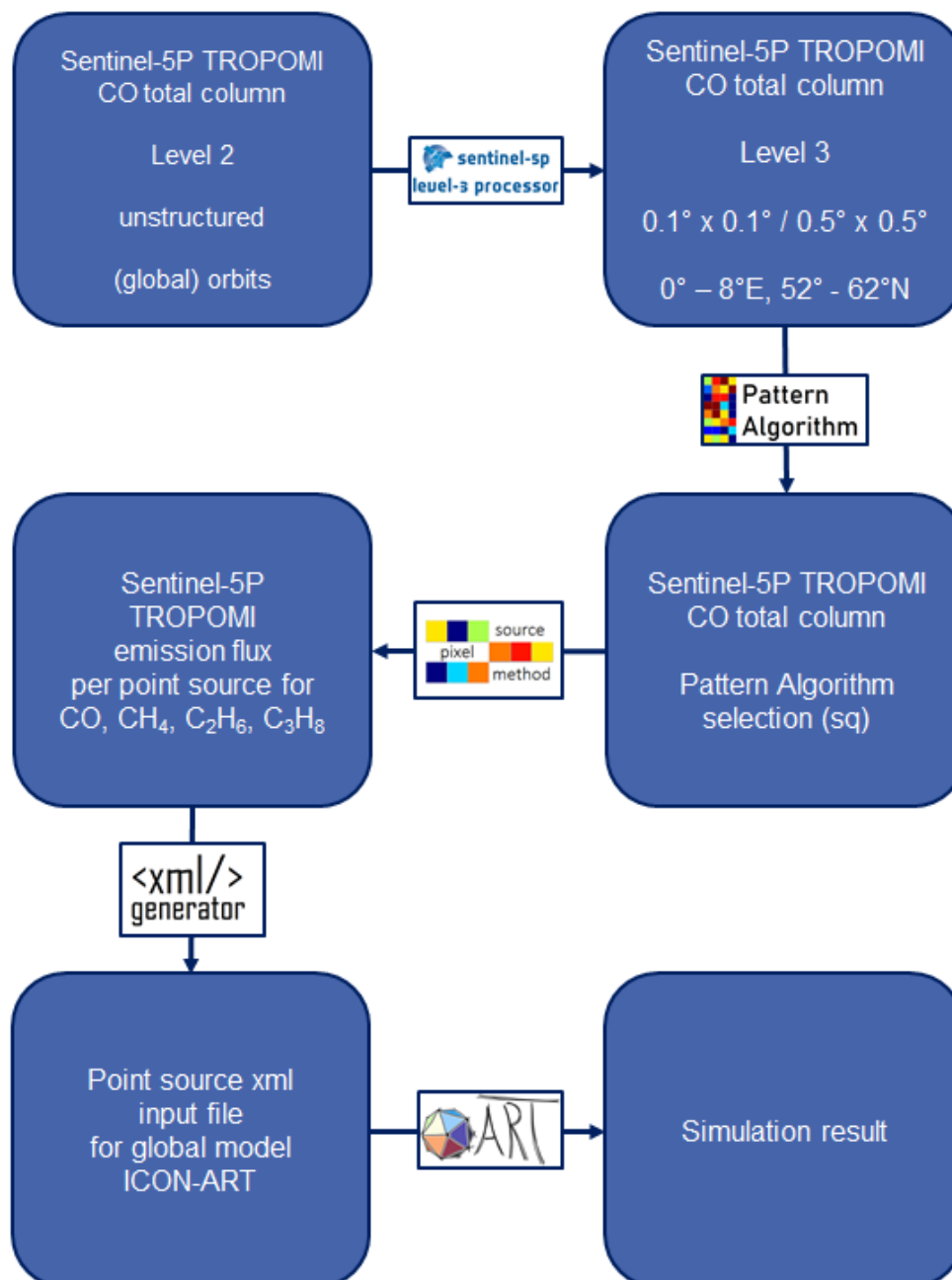
Figure 4.13: The workflow package WALLACE is a collection of python based programs. Its goal is to derive and quantify emission fluxes of trace gases on the basis of satellite measurements.

Here, we focus on carbon monoxide total column measurements from June 2018 to May 2021. This data comes as orbits in unstructured Level 2 data (see Section 4.3.1). As a first step the orbits are converted from Level 2 to Level 3 data by the Sentinel-5P Level 3 processor to get a data product with a regular latitude and longitude grid and a spatial resolution of $0.5° \times 0.5°$. Due to memory and file handling reasons, only data from the NSR is analysed. After applying the Pattern Algorithm to our three year mean we have highlighted the platform emissions within the background noise. This time with all North Sea platforms, also the ones in the southern part. Figure 4.14 displays the three year mean in $0.5° \times 0.5°$ resolution and the result of the Pattern Algorithm.

(a)   (b)
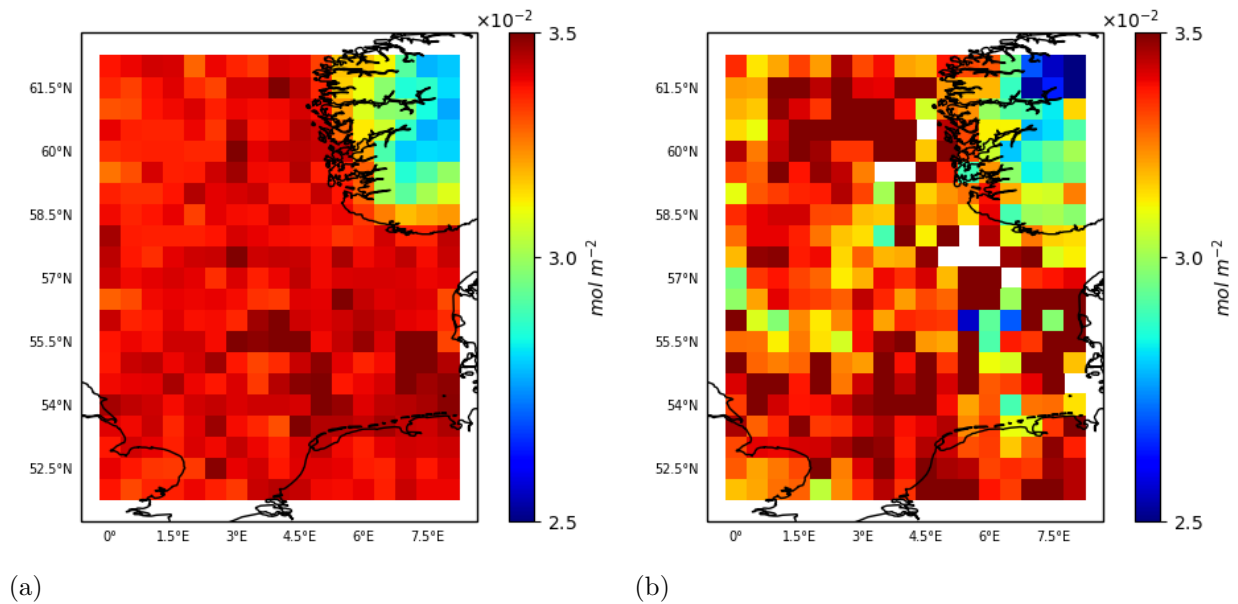
Figure 4.14: Carbon monoxide total column three year mean (a) and mean of the orbits selected by the Pattern Algorithm (b).

On the data shown in Figure 4.14 (b) we apply the Source Pixel Method as introduced in Section 4.3.3. For each platform we obtain the carbon monoxide total column value of the pixel in which it is located. With the information about the exact length and width of the pixel, which we derive from its latitude and longitude, we can use Equation 4.4 to calculate the emission flux E in kg s^{-1}. By using the mean of all NSC, which we introduced in Section 4.2, the carbon monoxide flux is converted to methane, ethane and propane flux. Table 4.6 gives an overview of the mean emission flux per pointsource derived from the TROPOMI measurements by the WALLACE workflow.

Table 4.6: Overview of the mean emission flux per pointsource derived from the TROPOMI measurements by the WALLACE workflow.

species	source strength in kg s^{-1}
CH$_4$	0.0192
C$_2$H$_6$	0.00053
C$_3$H$_8$	0.00045
CO	0.00031

With the XML-generator the data is transformed to the machine-readable XML-structure as pointsource input for the ICON-ART model as explained in Sections 3.3 and 4.3.4. In the final chapter of this work we evaluate and compare the three approaches introduced within this work, the EDGAR pointsource approach (see Section 4.1), EDGAR+ (see Section 4.2) and the WALLACE workflow.

4.4 Experimental design

In this section we want to bring everything together that has been presented in Chapter 4 and 3 with the introduction of the experimental design of this study. The simulations were performed on the HPC system HoreKa at the Steinbuch Centre for Computing (SCC) at the KIT.

For this work we used the ICON version 2.6.3 together with the corresponding ART tag, both released in 2021. A global R2B5 grid was implemented with 81920 triangular cells and a horizontal mesh size of about 78.9 km. Vertically this ICON setup consists of 90 levels with increasing thickness from the surface up to a height 75 km. The temporal output resolution of the simulations is 12 hours. As explained in Section 3.3 the internal computational time step `dtime` is six minutes. The global emissions for all simulations were taken from the EDGAR4.3.2 inventory with CH$_4$, C$_2$H$_6$, C$_3$H$_8$ and CO as emitted species and were interpolated to the native ICON grid by using CDO. This emission input data is given in the netCDF format and its spatial resolution is 0.1° × 0.1°. Following the scheme presented in Section 3.2 the data is then interpolated to the native R2B5 global grid of ICON and implemented as emissions. For the initialisation of the tracers we used globally constant values, concrete 1.8544×10^{-6} mol mol^{-1} for methane (Tans et al., 2021), 1.09×10^{-7} mol mol^{-1} for carbon monoxide (WHO, 2000), 1×10^{-9} mol mol^{-1} for ethane (CDIAC, 2012) and 1×10^{-10} mol mol^{-1} for propane (Pozzer et al., 2010).

All simulations use the simple OH-chemistry mechanism as desribed in Section 3.4 and have global EDGAR emissions, but as the focus of this work is the NSR, this is where they differ. We now introduce the following nomenclature: **A1 GRIDDED** denotes the simulation with gridded EDGAR emissions globally <u>and</u> in the NSR, just as described above. Simulation **A2 PNTSRC** uses EDGAR emissions that were transformed to pointsources within the NSR. The composition of simulations **A1 GRIDDED** and **A2 PNTSRC** defines the proof of concept to show, that the pointsource module works appropriately and that pointsource and gridded emissions are comparable within this setup. Further results and evaluation can be found in Chapter 5. The Simulations **B1 EDGAR**, **B2 EDGAR+** and **B3 WALLACE** denote the three different approaches to adjust emissions of oil and gas platforms in the NSR as presented in Sections 4.1, 4.2 and 4.3.5, respectively. This is done by implementing the missing emissions as pointsources, by creating a new gridded emission input dataset EDGAR+ and by the measurement based approach WALLACE which uses a complex algorithm to highlight and assign emissions to hotspots. To investigate the impact of all these simulations and make them comparable, we performed a reference simulation **Z ZERO** without any emissions in the NSR. Additionally, three simulations were performed with the exact same setup but on an R2B6 grid, which has a higher spatial resolution. These simulations are denoted as **Zh ZERO**, **A2h PNTSRC** and **B3h WALLACE**. An overview of the ICON-ART simulations made for this work is displayed in Table 4.7. Beside the simulation id, the emissions and methods used in the NSR are displayed, where "pntsrc" means an implementation of the pointsources in the northern part of the NSR and "pntsrc_all" indicates the adjustment of all North Sea platforms.

Table 4.7: Overview of simulations with ICON-ART 2.6.3. Listed here are the grid, the emissions inside the NSR and the method how species are emitted in ICON (2-dimensional gridded or 0-dimensional pointsources).

id	grid	NSR emission	method
Z ZERO	R2B5	-	gridded
A1 GRIDDED	R2B5	EDGAR	gridded
A2 PNTSRC	R2B5	EDGAR	pntsrc
B1 EDGAR	R2B5	EDGAR	pntsrc_all
B2 EDGAR+	R2B5	EDGAR+	gridded
B3 WALLACE	R2B5	WALLACE	pntsrc_all
Zh ZERO	R2B6	-	gridded
A2h PNTSRC	R2B6	EDGAR	pntsrc
B3h WALLACE	R2B6	WALLACE	pntsrc_all

5 Results

Within this section we evaluate measurement data from ground stations in Europe to investigate seasonal variability in the methane VMR. We will then focus on the analysis of the ICON-ART simulations which were introduced in Section 4.4. Starting with the reference simulations A1 GRIDDED and A2 PNTSRC with gridded EDGAR and pointsource emissions in the NSR, we later investigate the impact of the adjusted emissions on the seasonal variability, spatiotemporal distribution and global and regional methane budget. Furthermore, we take a look at the influence of GHG emissions on radiative forcing and compare our results to simulations performed on higher resolved grids. Additionally, we analyze the computing time and the sustainability of climate modeling in general.

5.1 Measurement sites in the North Sea region

In this section we investigate the seasonal variability of the methane emissions near the surface in Europe. As we learned in the previous sections, the quantification of GHG emissions is a difficult task that comes along with high uncertainties. Therefore we take a look on the methane VMR that is measured by five observation sites in Europe within the network of NOAA that contain long methane time series. These are Hohenpeissenberg, Germany (2006-2018), Storhofdi, Iceland (1992-2018), Mace Head, Ireland (1991-2018), the Baltic Sea station, Poland (1992-2011) and the Ocean station M, Norway (1983-2009) as displayed on the map in Figure 5.1. The measurement samples are injected into a gas chromatograph and separated from other constituents using flame ionization. Methane VMR is given in ppbv with an uncertainty of $\pm 0.2\,\%$ near $1800\,\mathrm{ppbv}$. More details about the technical process and data distribution can be found in Dlugokencky et al. (2018).
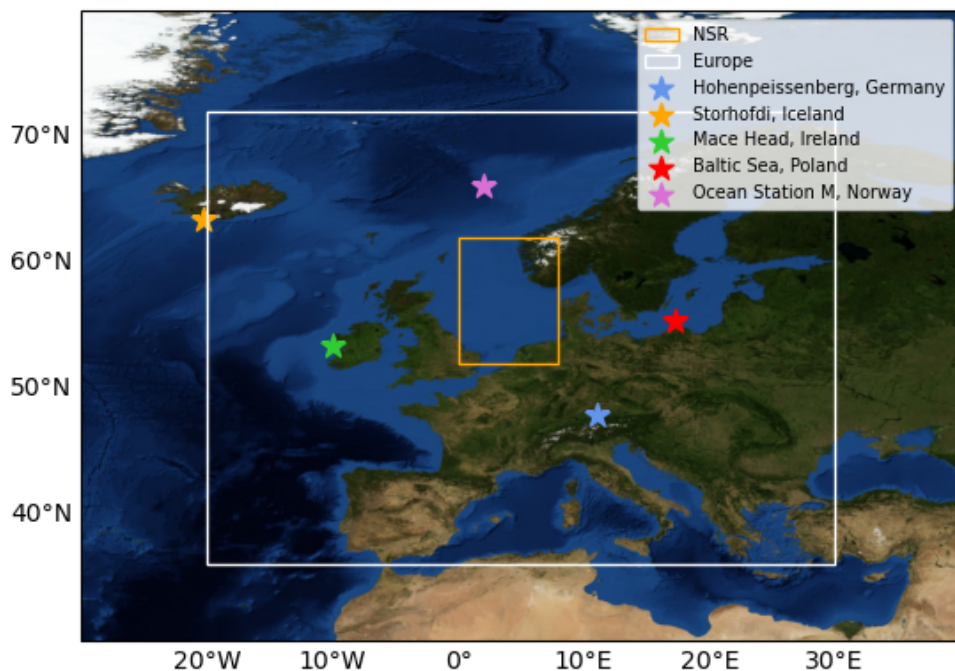
Figure 5.1: Map of Europe with the NOAA (2019) observation sites. Additionally, the defined areas of the NSR and Europe are displayed.

If we take a look at the raw data we can see that the time series contain more or less obvious outliers (see Figure 5.2 (a)). In a next step we mask all physically impossible values for methane VMR (equal to zero and negative) as shown in Figure 5.2 (b). Furthermore we calculate the mean μ and the standard deviation σ of the dataset without physically impossible values. All values higher than $\mu + 3\sigma$ and lower than $\mu - 3\sigma$ were declared as extreme outliers and also removed from the dataset. The result is the time series shown in Figure 5.2 (c) which shows values from about 1.6 - 2.2 $\times$ 10^{-6} mol mol^{-1} or 1600 - 2200 ppbv. Also the global methane trend with increasing values until the late 1990s, followed by a stagnation and a continuation of the increase as described in Section 2.2.2 is visible in the dataset. The mean value of each observation per year per site was calculated as well as the mean value of each month per site. The monthly means are divided by the annual mean of the corresponding year to receive relative monthly means for all observation years and sites. The mean values over the respective time series range for each month of these relative monthly means are displayed in Figure 5.3, including the standard deviation of the relative monthly means per site.

(a)

(b)

(c)
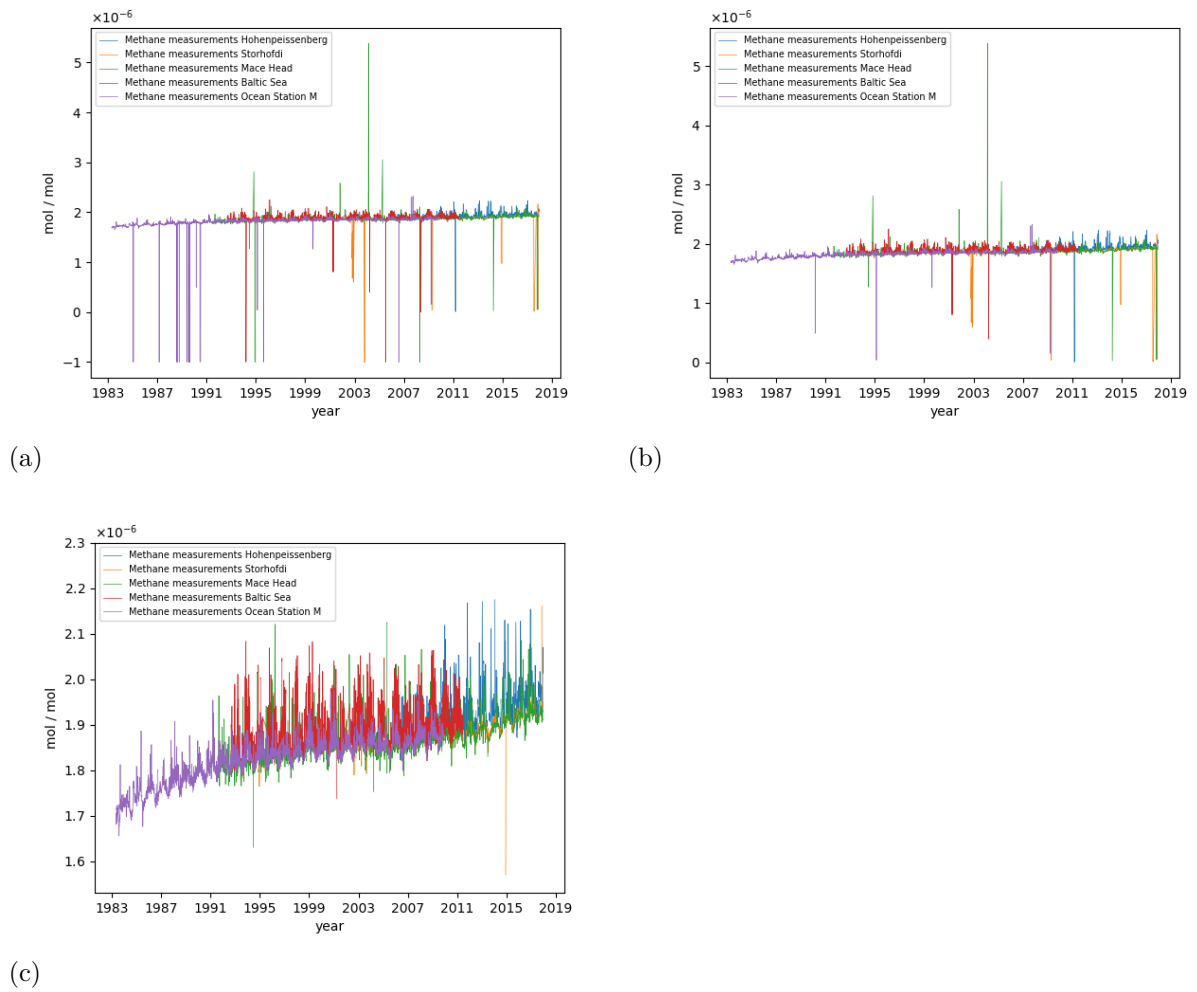
Figure 5.2: Time series of methane VMR raw data (a), without physically impossible values (b), and with extracted outliers above $\mu + 3\sigma$ and below $\mu - 3\sigma$ (c) at the five NOAA observation sites in Europe. Note the changing scales.

We recognize that mostly the months in the autumn and winter seasons have relatively high methane VMR compared to the annual mean of the corresponding year, although this is just an increases of about 0.5-2 %. These insights about the annual cycle and the regional mean methane VMR derived from measurement sites will be used in the following sections for the comparison with the results of the ICON-ART simulations that were performed within this work.
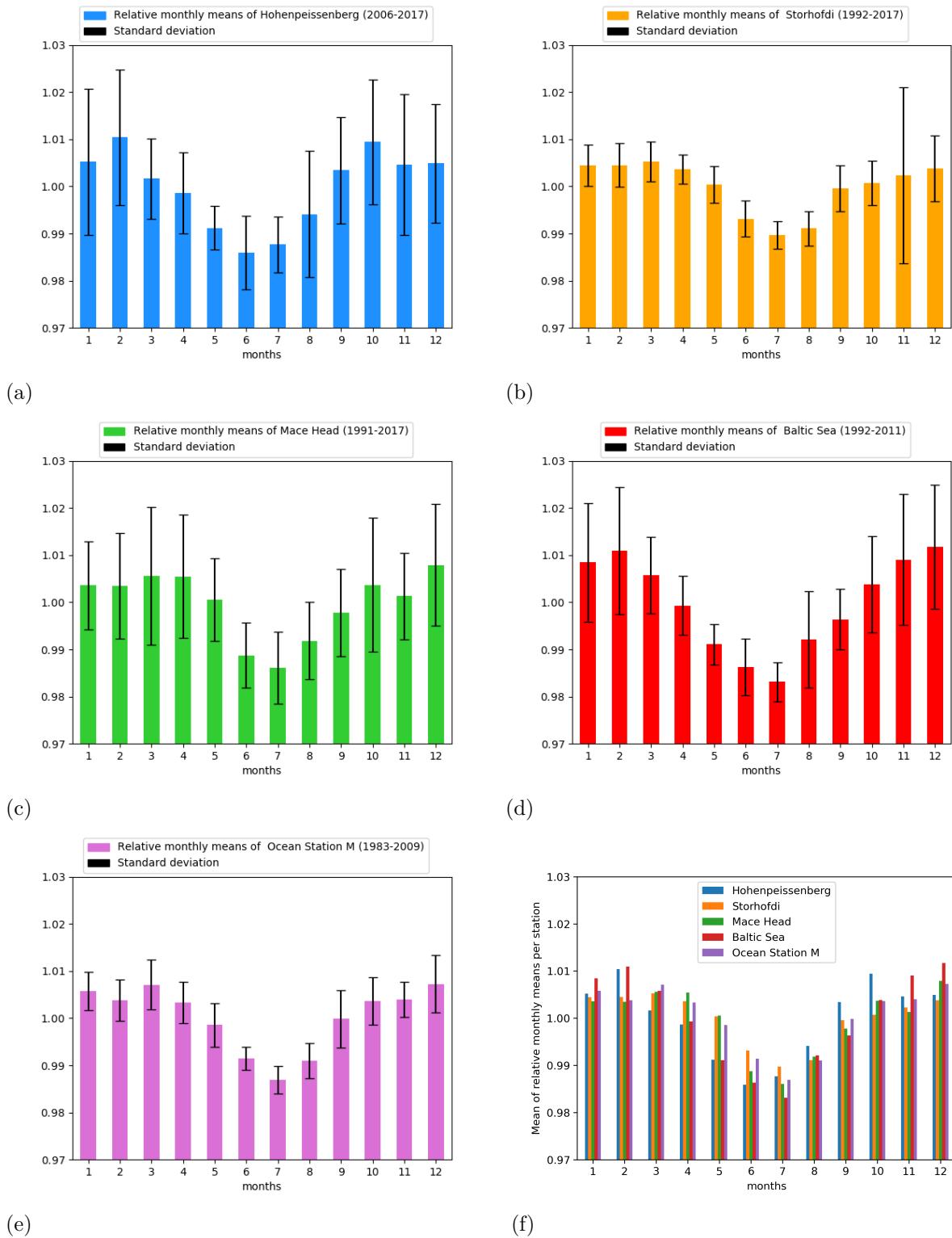
Figure 5.3: Mean of relative monthly means at Hohenpeissenberg (a), Stofhofdi (b), Mace Head (c), Baltic Sea (d), Ocean Station M (e) and all together (f).

5.2 Reference simulations

The basic simulation A1 GRIDDED with original gridded EDGAR emissions shows an accurate annual cycle for the methane VMR on a global and regional scale as displayed in the time series in Figure 5.4 (a) and (b), respectively. Following, we define and calculate the European mean within the area of 36° N - 72° N and 20° W - 30° E, as shown on the map in Figure 5.1.

(a)   (b)
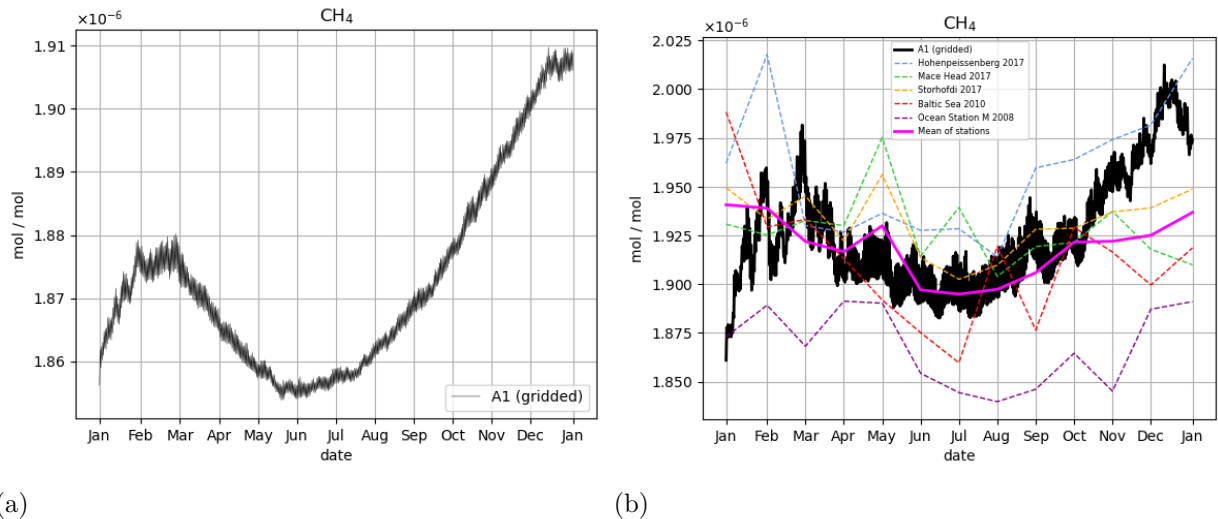
Figure 5.4: Time series of mean methane VMR from simulation A1 GRIDDED on a global (a) and European scale (b). Additionally the measurements of methane VMRs for the most recent year of the stations from Section 5.1 are included in (b).

Starting at the globally constant initialisation value of 1854.5 ppbv an increase in the VMR is recognizable until the end of February. At the beginning of the northern hemispheric spring, the methane VMR drops to a global minimum of 1854 ppbv and a European minimum of 1861 ppbv during summer. In autumn and winter the methane VMR rises up to its global maximum of 1910 ppbv. An even higher maximum of the methane VMR is recognizable on the European continent with a value of 2012 ppbv. The global mean value of 1873 ppbv for the simulation year 2018 from A1 GRIDDED differs from the measurements of Tans et al. (2021) by only 0.7 %. The Delta of the global methane VMR between the beginning and end of the year is about 5 ppbv, which matches to the annual increase in the methane VMR for the years 2010-2019 of 7.6 [4 - 15] ppbv (Tans et al., 2021). The European methane VMR mean value of simulation A1 GRIDDED is 1926 ppbv and with that, as expected due to a large amount of land mass, higher than the global mean. For a general comparison with in situ data, we included the measurements of methane VMR for the last recorded year of the stations from Section 5.1 in the graph

of Figure 5.4 (b). As the measurements are provided weekly, we took the first available sample of a month for this study. We recognize, that the measurements show a similar annual cycle for the European region with a lower methane VMR during summer. For the mean of the five selected measurement sites we notice a good match to the ICON-ART simulation results except from the before mentioned differences at the simulation start and some divergence at the end.

The map displayed in Figure 5.5 shows the global distribution of methane after one year in simulation A1 GRIDDED. A clear separation between the northern and southern hemisphere is visible. As there are much more emissions due to an unequally distribution of land mass and population, the northern hemisphere shows a higher methane VMR. The most powerful emission hotspots are China and India, where combustion and solid waste is a big driver (Janssens-Maenhout et al., 2019), but there are also some hotspots visible in central Africa, the Eurasian continent and North America caused by emissions e.g. from the energy and power industry or the agricultural sector (Janssens-Maenhout et al., 2019), all demonstrating the human impact on the global methane budget.
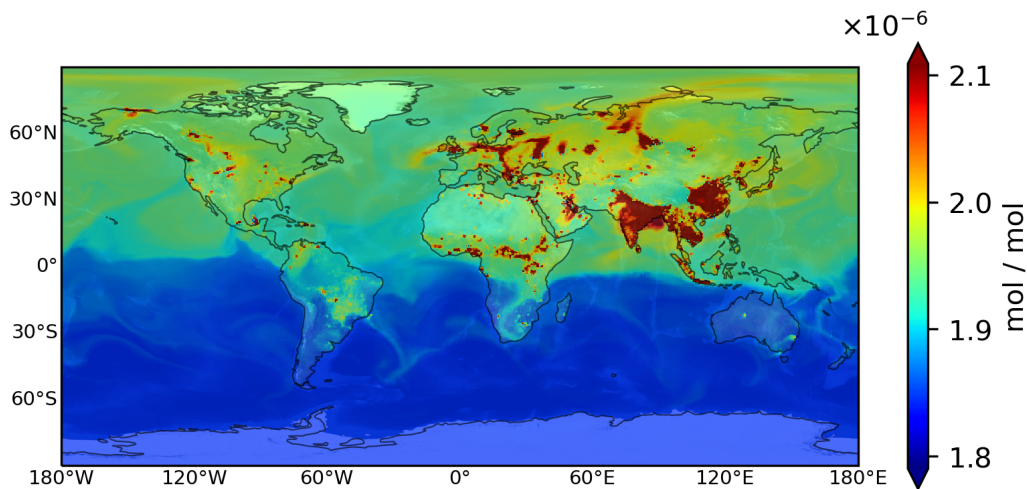
Figure 5.5: Methane VMR at the Earth's surface after one year of simulation A1 GRIDDED.

In reference simulation A2 PNTSRC the gridded NSR emissions of EDGAR are removed and replaced by pointsources. The difference to simulation B1 EDGAR is, that only the platforms in the northern part of the NSR are implemented as pointsources. A2 PNTSRC is part of the experimental setup of this work for two main reasons. First, we want to proof that the pointsource module is able to substitute gridded emissions without artefacts by simultaneously conserving the total mass of emitted methane and the annual cycle. Second, we will use simulation A2 PNTSRC in a comparison with B1 EDGAR and B3 WALLACE to evaluate the impact of the adjusted platform emissions (see Section 5.4).
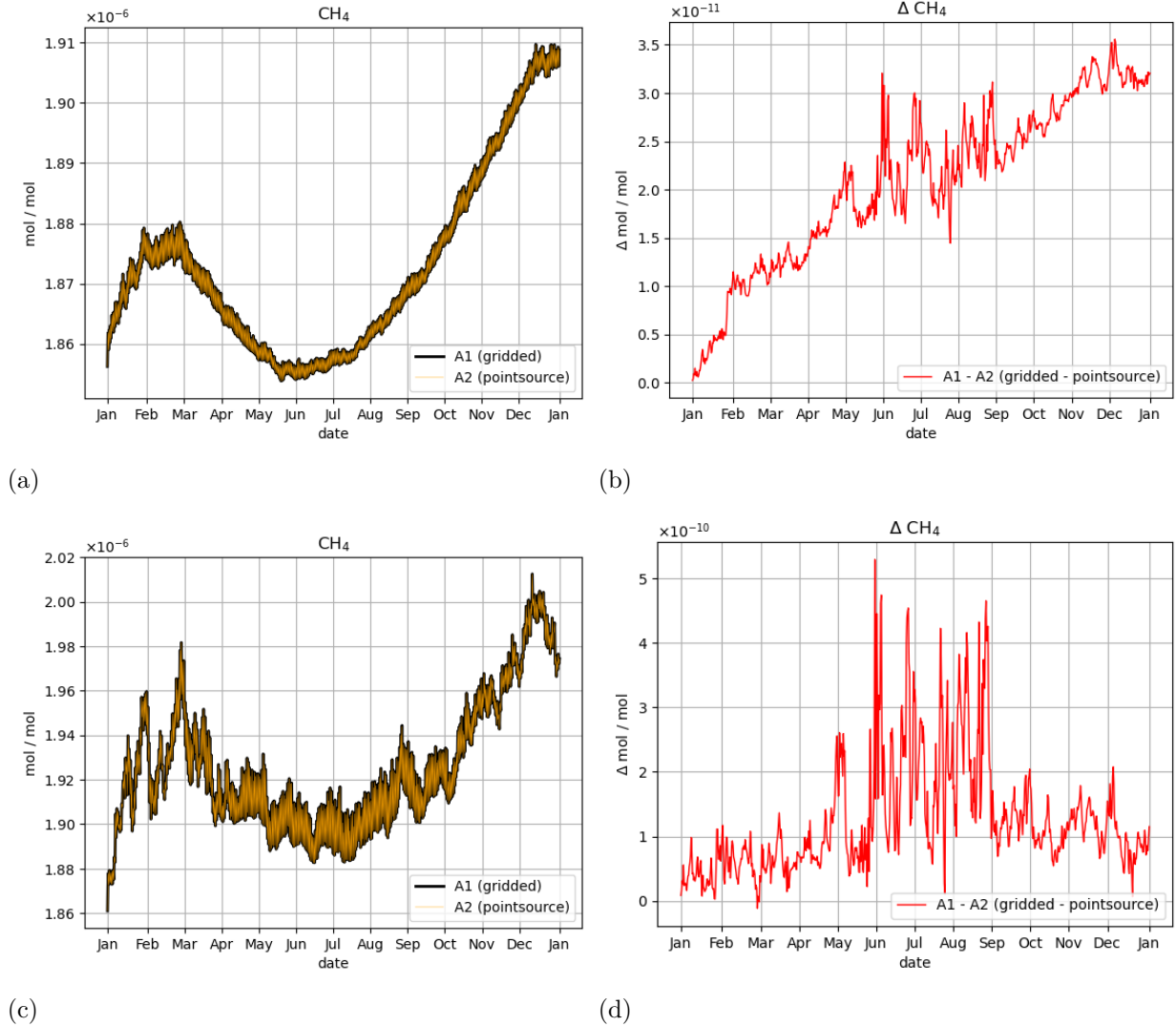
Figure 5.6: Comparison of time series of mean methane VMR from simulations A1
GRIDDED and A2 PNTSRC on a global (a) and European scale (c).
Additionally the differences are displayed in (b) and (d), respectively.

The comparison of ICON-ART simulations A1 GRIDDED (gridded EDGAR emissions)
and A2 PNTSRC (adjusted pointsource emissions) reveals that both fit perfectly over the
whole year on a global and regional scale as visible in Figure 5.6 (a) and (c). The maximum
of the absolute difference over the year on a global scale is $\Delta_{max} = 0.03558$ ppbv. The
global annual mean difference is $\Delta_{mean} = 0.02069$ ppbv (see Figure 5.6 (b)), the European
mean difference is $\Delta_{mean} = 0.1246$ ppbv (see Figure 5.6 (d)). All in all we can adhere
that the pointsource module slightly underestimates the gridded emissions over the year
by about 0.001 % on a global and about 0.006 % on an European scale. This result can be
seen as a proof of concept that the pointsource module of ART is working fine and adjusts
the platform emissions of EDGAR without a significant gain or loss of methane.

If we take a look at the difference of reference simulation A1 GRIDDED and the zero NSR emission simulation Z ZERO, we can see that with a positive and increasing Delta of methane VMR the OH number concentration decreases what leads to a negative Delta for the OH number concentration in Europe (see Figure 5.7 (a) + (b)). This anti-correlation is explained in Section 2.2.1 and displayed in Figure 2.3. In Figure 5.7 (c) we present the correlation of Δ CH$_4$ and Δ OH for Europe in A1 GRIDDED - Z ZERO and derive r = -0.87, which is a good indication for the negative correlation of methane and OH. These results show, that the implemented simple chemistry mechanism of ICON-ART as introduced in Section 3.4 works appropriately on a global and regional scale, as expected.

(a)

(b)

(c)
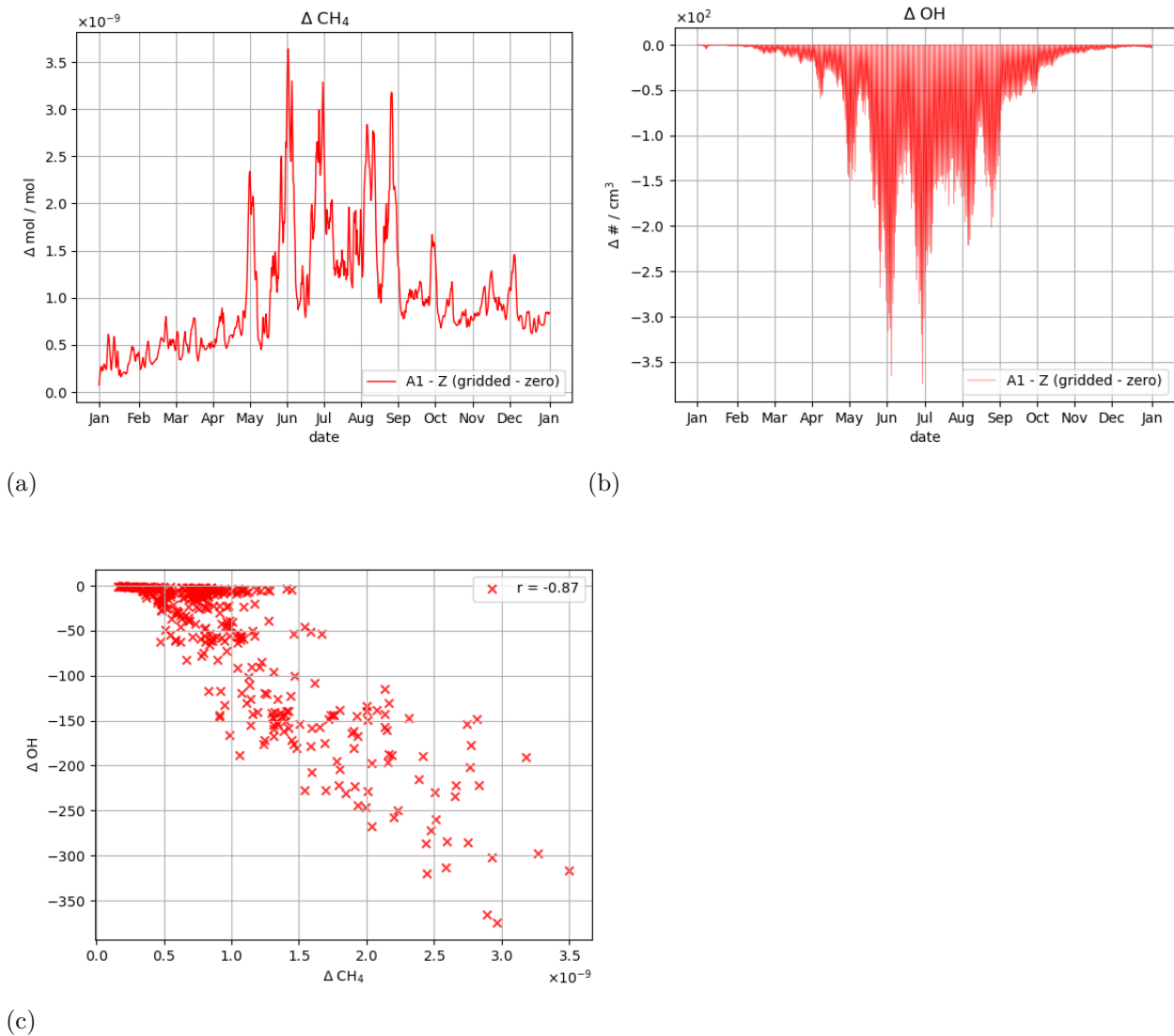
Figure 5.7: Time series of Δ CH$_4$ (a) and Δ OH (b) from simulation A1 GRIDDED - Z ZERO on a European scale. Additionally, the correlation of Δ CH$_4$ and Δ OH is displayed (c).

Although r = -0.87 is a good result and strong indication for the anti-correlation of $\Delta\,CH_4$ and $\Delta\,OH$ we do not achieve a perfect coefficient of r = -1 due to the following reasons. First, methane is transported and distributed horizontally and vertically on the globe. As we only evaluate the Deltas on the lowermost model level, this leads to uncertainties. Second, the triangular grid on which the model computes the simplified OH-chemistry is regridded to a regular latitude and longitude grid. Within this interpolation, some error might occur and affect the accuracy of this correlation. An evaluation of the negative correlation on a global scale led to even lower values of r. Background information on the statistical methods and the definition of Pearson's correlation coefficient can be found in Appendix D.

From the methane Delta in A1 GRIDDED - Z ZERO we can also obtain the impact of the recent methane emission fluxes on the European continent as they are implemented in EDGAR. Figure 5.7 (a) shows that this $\Delta\,CH_4$ reaches a maximum of 3.640 ppbv and a mean of about 1 ppbv.

The improvements of the pointsource module are also visible in the output, if we take a look at the first time step which is displayed on the maps in Figure 5.8. The shape of the platform locations (black dots) in the gridded EDGAR emission (original $0.1° \times 0.1°$ (a) and interpolated $0.5° \times 0.5°$ resolution (b)) is much better represented in the pointsource output (d) than with the gridded emission (c). This better spatial accuracy is of high importance especially when using the Pattern Algorithm as explained in Section 4.3.2.
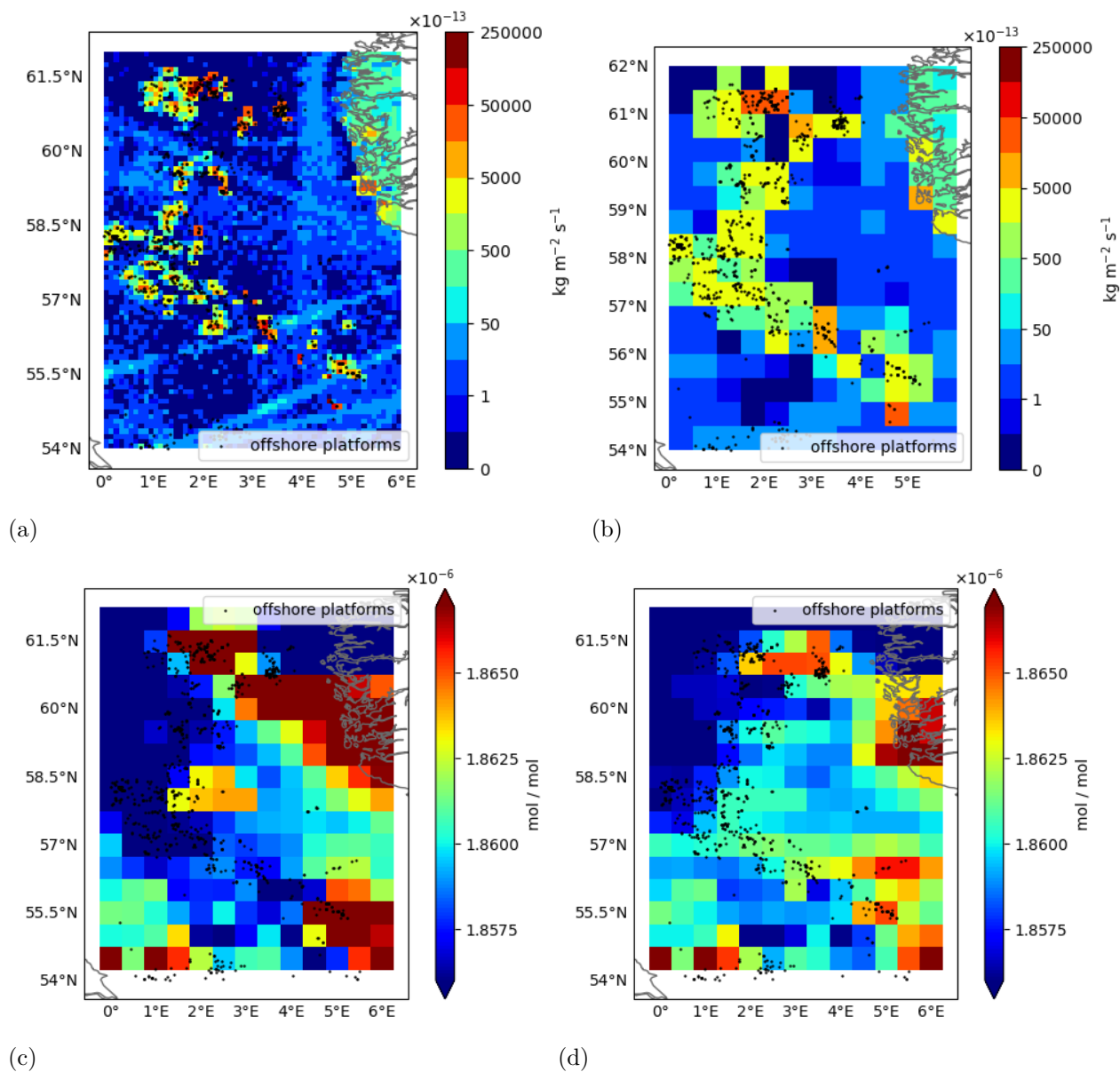
Figure 5.8: Comparison of EDGAR input in $0.1° \times 0.1°$ (a) and $0.5° \times 0.5°$ resolution (b) with ICON-ART output from simulation A1 GRIDDED (c) and A2 PNTSRC (d).

5.3 Atmospheric lifetime and depletion

As described in Section 2.2.1, the number concentration of the hydroxyl radical depends on the solar radiation and air temperature. The time series in Figure 5.9 (a) and (b) show that this is valid for the simulation setup of this work as the European OH number concentration is significantly higher during summer (up to 1.2×10^6 # cm^{-3}) when temperature is rising up to a maximum of over 285 K at the same time. We insert OH number concentration and air temperature into Equations 2.2 and 2.3 to calculate the time series of the European mean methane lifetime as displayed in Figure 5.9 (c).

(a)

(b)

(c)
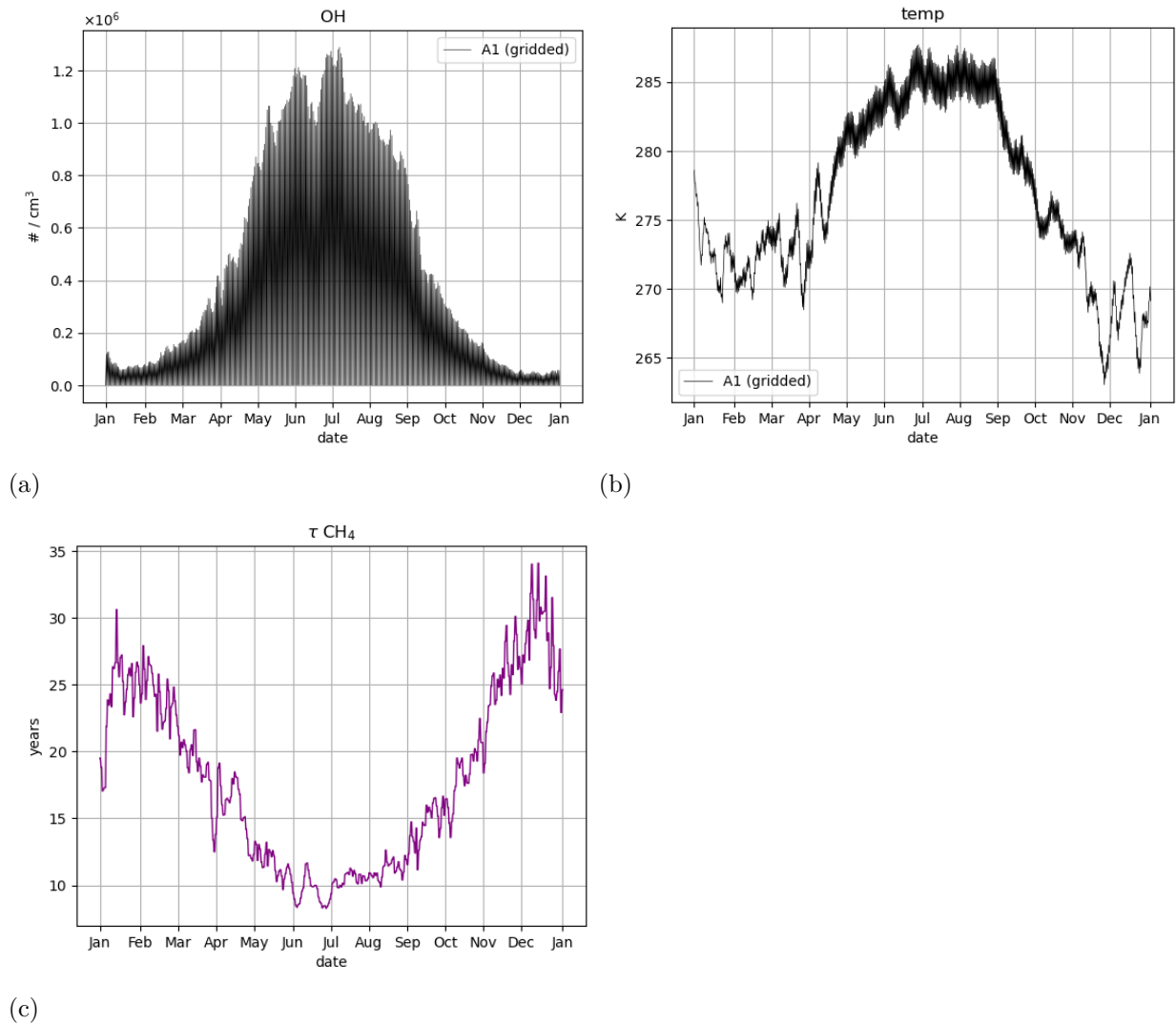
Figure 5.9: Time series of OH number concentration (a), temperature (b) and τ CH$_4$ (c) from simulation A1 GRIDDED on a European scale.

As expected, it is lower in summer with lifetimes about 8-12 years, what matches to the most common literature values (Hayman et al., 2014; Weimer, 2015), while it rises up to

34 years during European winter, where less solar radiation causes lower temperatures and OH number concentrations. To answer the question how much methane is reduced by the reaction with OH, we need the e-folding lifetime of methane. The e-folding lifetime of a species denotes the time which is required to decrease to $1/e$ of its original amount (Jacobson, 2005). We calculate the depletion due to Jacob (1999) as

$$d = \left(1 - e^{-\frac{1}{\tau}t}\right) \cdot 100 \tag{5.1}$$

Here, τ denotes the lifetime and t is time. For the summer and winter solstice on 21.06.2018 and 21.12.2018 the methane lifetime and the depletion on the Earth's surface is displayed on the maps in Figure 5.10. We recognize lifetimes between 1 and 5 years in the tropical regions, where temperatures are relatively high throughout the year, and lifetimes of about 10 to 80 years in the mid-latitudes and polar regions (see (a) and (c)). We found a maximum methane depletion of 9 % in the tropics and much lower values in the mid-latitudes (see (b) and (d)).

(a)

(b)

(c)

(d)
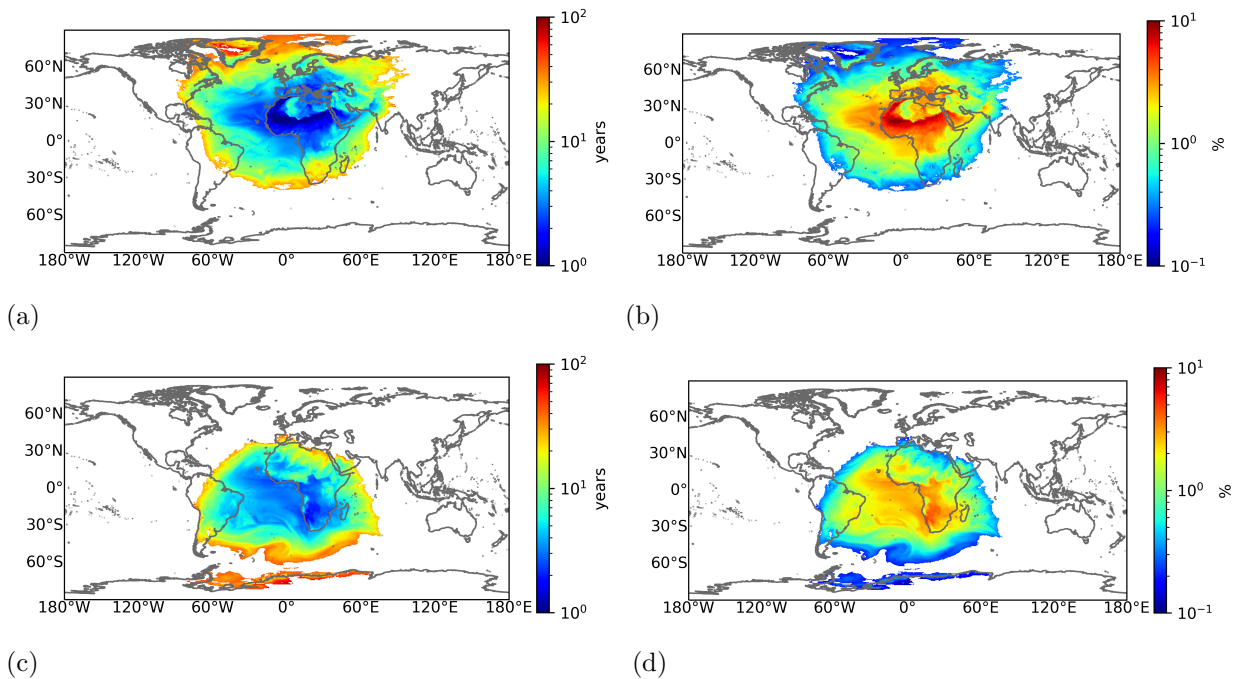
Figure 5.10: Comparison of methane lifetime and depletion on the Earth's surface on 21.06.2018 (a) + (b) and on 21.12.2018 (c) + (d), respectively.

This leads to the conclusion that the reaction with OH has a small impact on the annual cycle of methane with a depletion of less than 10 %. The annual cycle in our simulations is therefore mostly regulated by emissions where transport and advection play an important role to explain the minimum in the methane VMR during summer.

5.4 Comparison and impact of adjusted emissions

After a closer look at the reference simulations A1 GRIDDED, A2 PNTSRC and Z ZERO we will now focus on the main questions of this work. What is the impact of the missing emissions from oil and gas platforms in the NSR on the global and regional methane budget and which methods are appropriate to adjust those gaps in well-established emission inventories? We therefore evaluate simulations B1 EDGAR, B2 EDGAR+ and B3 WALLACE, that represent the adjustment methods which were developed within this work and were introduced in Chapter 4.

First we want to take a look at the methane time series that show the annual cycle of the adjustment methods EDGAR, EDGAR+ and WALLACE as displayed in Figure 5.11 on a global and European scale, respectively.
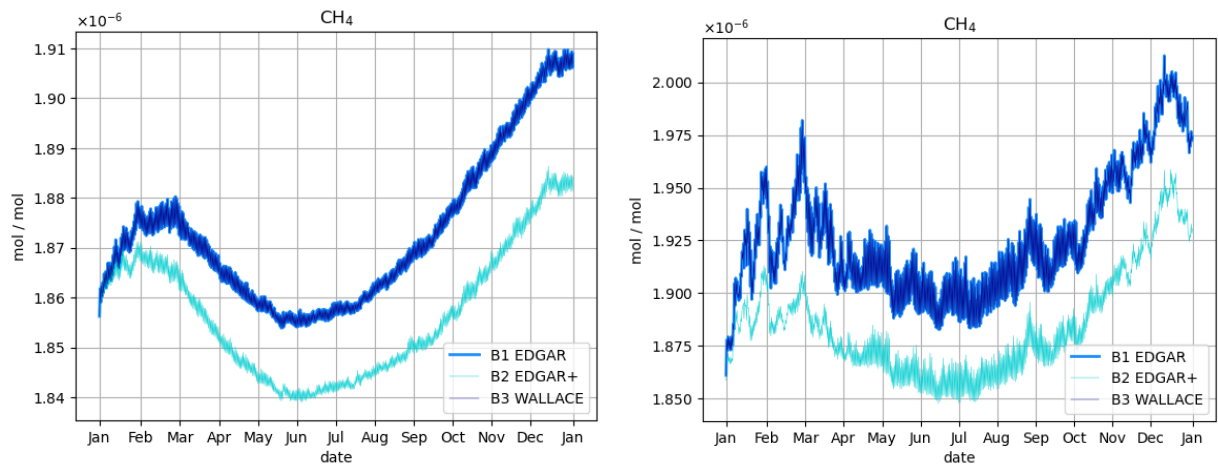
(a)   (b)

Figure 5.11: Time series of mean methane VMR from simulations B1 EDGAR, B2 EDGAR+ and B3 WALLACE on a global (a) and European scale (b).

First of all we recognize, that the annual cycle of all three simulations is similar to the references A1 GRIDDED and A2 PNTSRC. While the two methods using the pointsource module B1 EDGAR and B3 WALLACE are indistinguishable to the naked eye, B2 EDGAR+ shows much lower values of methane VMR during the year leading to a gap of about 25 ppbv on a global scale. A similar picture arises for the European continent with a gap between B2 EDGAR+ and the two others of about 50 ppbv.

For the evaluation of the impact of the adjusted emissions on the global and regional methane budget, we consult the difference of B1 EDGAR, B2 EDGAR+ and B3 WALLACE to the reference simulations A1 GRIDDED and A2 PNTSRC. To be consistent with the emission modules that are implemented, we compare the two pointsource methods B1 EDGAR and B3 WALLACE to the reference simulation A2 PNTSRC. Meanwhile, the new gridded product B2 EDGAR+ is compared to the original gridded EDGAR simulation A1 GRIDDED. The Deltas are displayed in Figure 5.12.
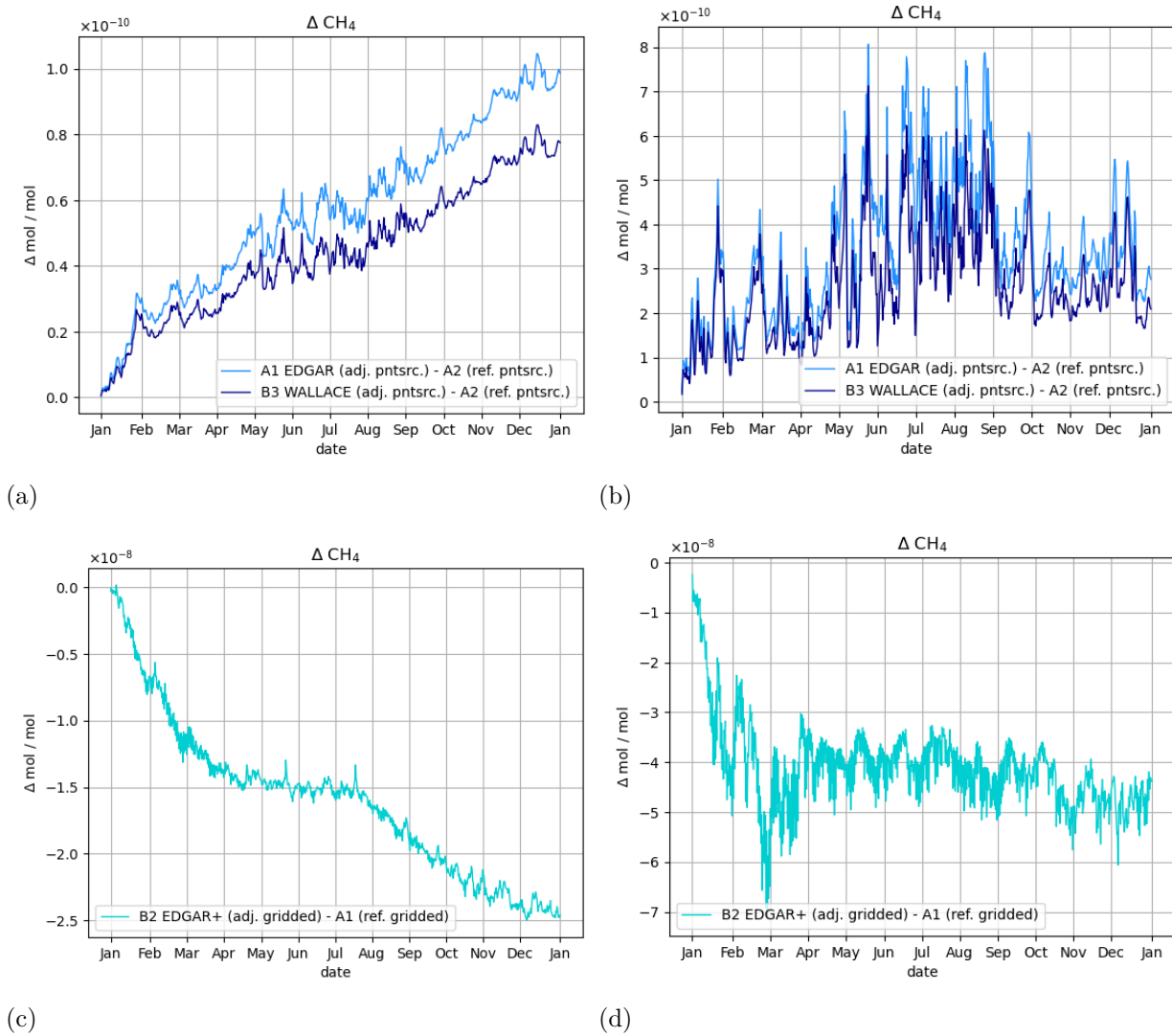
Figure 5.12: Comparison of $\Delta\,CH_4$ time series from simulations B1 EDGAR, B2 EDGAR+ and B3 WALLACE with reference simulations A1 GRIDDED and A2 PNTSRC on a global (a)+(c) and European scale (b)+(d).

We notice the difference between B1 EDGAR and B3 WALLACE on a global and European scale (see 5.12 (a) and (b)), which reveals, that B1 EDGAR is globally higher by about 0.021 ppbv than B3 WALLACE after one year of simulation. On a European

scale the difference between B1 EDGAR and B3 WALLACE is 0.067 ppbv. When looking at the difference of simulations B2 EDGAR+ and A1 GRIDDED (see Figure 5.12 (c) and (d)) we obtain a negative Delta of about -25 ppbv on a global scale and -50 ppbv for the European continent. The new gridded product, which is based on reported data due to OSPAR (2019), underestimates the simulation based on the well-established EDGAR product. This difference of about 25-50 ppbv leads to two conclusions: First, the reported emissions from OSPAR (2019) are too low compared to the EDGAR emission inventory and the resulting values from the WALLACE workflow. Second, without an appropriate set of proxy data, the construction of gridded emission products is error-prone and leads to results that are not comparable to the adjustments based on pointsources.

From the time series of $\Delta \, CH_4$ in Figure 5.12 (a) and (b) we receive the answer to the question about the impact of the missing emissions on the global and regional methane budget. For simulation B1 EDGAR we recognize a global Delta of 0.1 ppbv, simulation B3 WALLACE shows a gap of 0.078 ppbv. If we consider the values for the European continent, we recognize a global Delta of 0.276 ppbv for simulation B1 EDGAR and of 0.21 ppbv for simulation B3 WALLACE. This constitutes an impact of about 0.005 % on the global and 0.01 % on the European methane budget over a year.

If we take a look at all North Sea platforms (considering B1 EDGAR - Z ZERO and B3 WALLACE - Z ZERO) we receive an amount of 0.2053 ppbv globally and 1.249 ppbv regionally for B1 EDGAR. Furthermore we obtain 0.1926 ppbv globally and 1.17 ppbv regionally for simulation B3 WALLACE. This, in turn, constitutes an impact of about 0.01 % on the global and 0.06 % on the European methane budget.

Time series with analogous evaluations for the species CO, C_2H_6, C_3H_8 and OH are shown in the Appendix Figures E.1, E.2, E.3 and E.4, respectively. For the VMR of CO we recognize that the annual cycle is different to the one of CH_4, as the chemical reaction with OH (producing CO_2) is much weaker and therefore it is much more dominated by emissions. C_2H_6 and C_3H_8 are also taking part in the simplified OH-chemistry and their annual cycles are similar to the one of methane. For all substances we achieve small Deltas between the simulations A1 GRIDDED and A2 PNTSRC in the same way as for methane. Also the adjusted emissions in B1 EDGAR, B2 EDGAR+ and B3 WALLACE show accurate results.

Following we show maps as well as zonal and meridional means of the Delta, that is caused by the missing emissions in the NSR as adjusted by WALLACE. In Figure 5.13 four maps are shown, that display the distribution of $\Delta \, CH_4$ from B3 WALLACE - A2 PNTSRC on the globe after one day (a), one month (b), six months (c) and one year (d) of simulation.
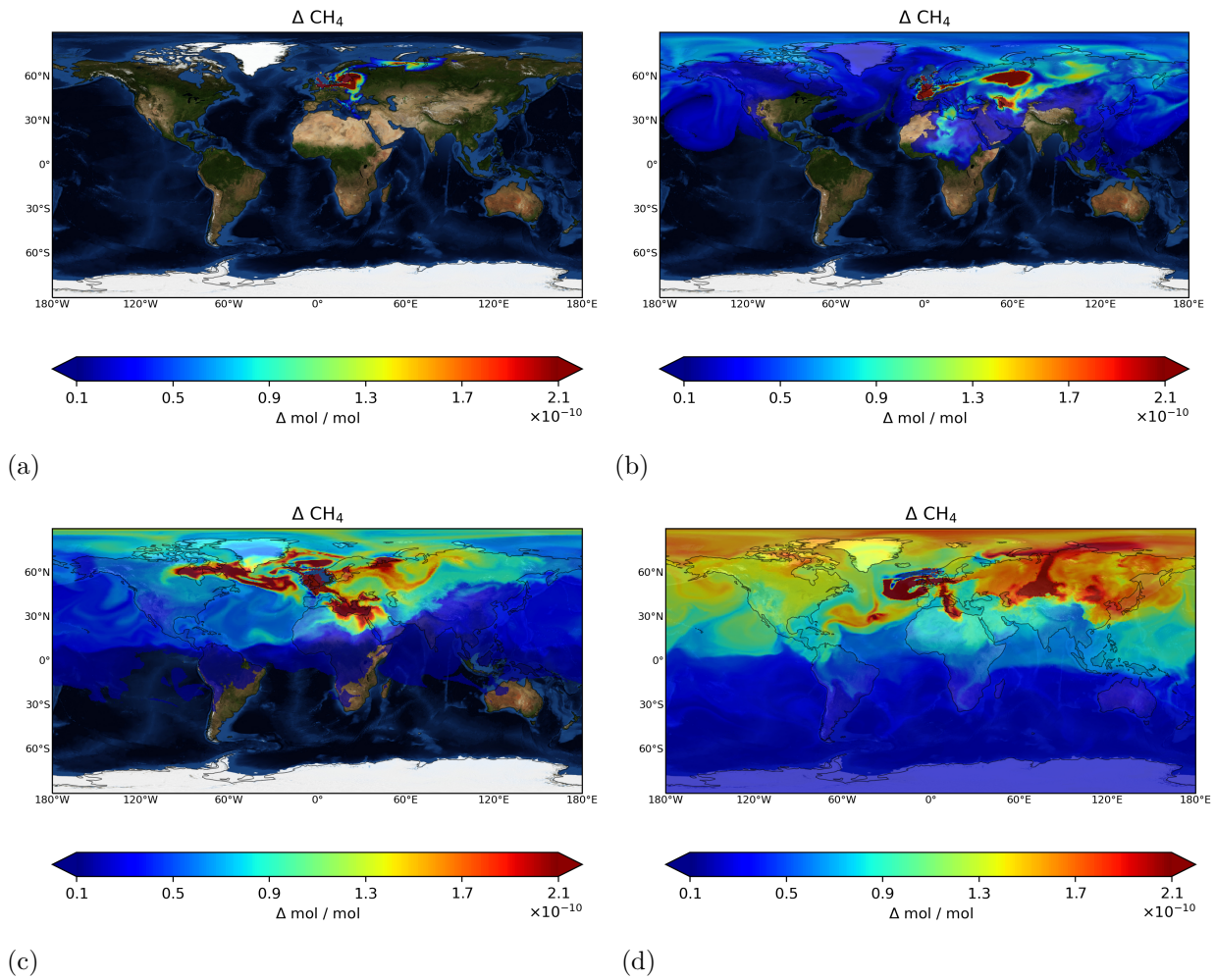
Figure 5.13: Comparison of the $\Delta\,CH_4$ distribution from B3 WALLACE - A2 PNTSRC after one day (a), one month (b), six months (c) and one year (d).
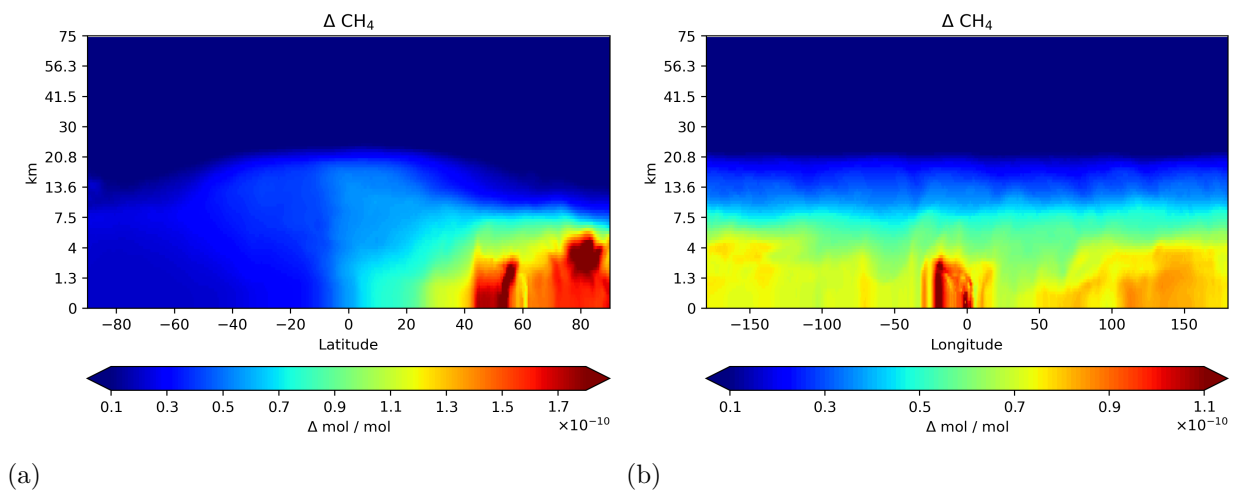
Figure 5.14: Zonal (a) and meridional mean (b) of $\Delta\,CH_4$ from B3 WALLACE - A2 PNTSRC after one year of simulation.

The two vertical sections in Figure 5.14 show a zonal (a) and a meridional mean (b) of the distribution of $\Delta\,CH_4$ for the same simulation.

Figure 5.13 impressively shows the influence of the adjusted emissions on the European continent after one day (a) and one month (b). Within half a year, the VMRs in the northern hemisphere are impacted by the methane sources from oil and gas platforms in the NSR and after one year of simulation we can see that methane is transported all over the globe. Although the VMR differences between B3 WALLACE and A2 PNTSRC are relatively small in the southern hemisphere (about 0.01 ppbv), we detect a measurable impact on the European continent and the whole northern hemisphere (see Figure 5.13 (c) and (d)), as also shown in the time series above.

The vertical sections in Figure 5.14 underline these impressions. Additionally to the impact on the northern hemisphere, we recognize the hotspot of the emissions around 50-55 °N (see zonal mean (a)) and around 0 ° (see meridional mean (b)). Furthermore, we can see that the emissions are transported up to a height of about 21 km.

Within this section we evaluated the impact of the adjusted emissions on the spatiotemporal distribution and the global and regional budget. We have found that the emissions from platforms in the NSR contribute to the European methane budget by about 1.2 ppbv or 0.06 %. Globally we recognize a minor effect on the southern hemisphere of 0.01 ppbv but a main impact on the northern hemisphere and the European continent in particular as visible in the zonal and meridional means.

5.5 Influence on radiative forcing

Radiative forcing denotes "an externally imposed perturbation in the radiative energy budget of the Earth's climate system", mainly by human-induced changes in the VMRs of gases like CO_2 or CH_4 (Ramaswamy et al., 2001). Due to IPCC's AR6, the human-caused radiative forcing in 2019 relative to 1750 was $2.72\,\mathrm{W\,m^{-2}}$, where carbon dioxide contributed about $2.16\,\mathrm{W\,m^{-2}}$ and methane $0.54\,\mathrm{W\,m^{-2}}$ (Forster et al., 2021). Compared to 2011, radiative forcing has increased by $0.43\,\mathrm{W\,m^{-2}}$ of which $0.34\,\mathrm{W\,m^{-2}}$ are caused by higher GHG VMRs (IPCC, 2021).

Ramaswamy et al. (2001) introduced a simplified expression for the determination of radiative forcing due to GHGs like CO_2, CH_4 or N_2O. Here, the radiative forcing ΔF for methane is calculated as

$$\Delta F \quad = \quad \alpha \cdot \left(\sqrt{M} - \sqrt{M_0}\right) - \left(f(M, N_0) - f(M_0, N_0)\right) \tag{5.2}$$

where M denotes the actual methane VMR in ppbv, M_0 and N_0 denote the methane and nitrous oxide VMR of the reference year, also in ppbv. Furthermore, the constant $\alpha = 0.036$ is used and the term f(M,N) is defined as

$$f(M, N) \quad = \quad 0.47 \cdot ln\left[1 + 2.01 \times 10^{-5} \cdot (MN)^{0.75} + 5.31 \times 10^{-15} \cdot M(MN)^{1.52}\right].$$

For the calculation of ΔF for the simulation A2 PNTSRC we use $M = 1908.78\,\mathrm{ppbv}$ as the final methane VMR in the simulation year 2018. Furthermore, we assume the reference values for the year 1750 of methane and nitrous oxide as $M_0 = 700\,\mathrm{ppbv}$ and $N_0 = 270\,\mathrm{ppbv}$, respectively (Ramaswamy et al., 2001). This leads to a CH_4-induced radiative forcing of $0.544076\,\mathrm{W\,m^{-2}}$ for simulation A2 PNTSRC, a value that matches perfectly the assumption of IPCC's AR6. Analogously, we calculate ΔF for simulation B3 WALLACE and take $M = 1908.86\,\mathrm{ppbv}$. Here, the radiative forcing is $0.544104\,\mathrm{W\,m^{-2}}$, indicating an enhancement of $0.028\,\mathrm{mW\,m^{-2}}$ caused by the missing emissions in the NSR. As the adjusted emissions of the North Sea platforms are very small compared to the global methane budget, they make a minor contribution to radiative forcing, as expected. Nevertheless, there are many small contributions that end up having a large impact on global radiative forcing and this showcase demonstrates that with the help of methods like WALLACE and models like ICON-ART, it is possible to quantify the driving forces.

5.6 Simulations with higher spatial resolution

Within this section we evaluate the effect of changes in the global grid resolution in the ICON-ART model on the variability and the spatial distribution of methane. For this reason the three simulations Z ZERO, A2 PNTSRC and B3 WALLACE were performed on an ICON R2B6 grid consisting of 327 680 triangular cells and a meshsize of $\overline{\Delta x} = 39.4\,\mathrm{km}$. The simulations with higher resolution are denoted as Zh ZERO, A2h PNTSRC and B3h WALLACE.

As visible in Figure 5.15 (a) and (b), the annual cycle starting at the initialisation value of 1854.5 ppbv is represented in a similar way as in the R2B5 simulation but with a much higher amplitude of about 30-35 ppbv compared to 3-5 ppbv globally. This effect is also visible, although much weaker, in the European mean. Both time series show methane VMR which are about 20 ppbv lower globally and about 5 ppbv lower on a European scale at the end of the year than in the R2B5 simulations.

(a)   (b)
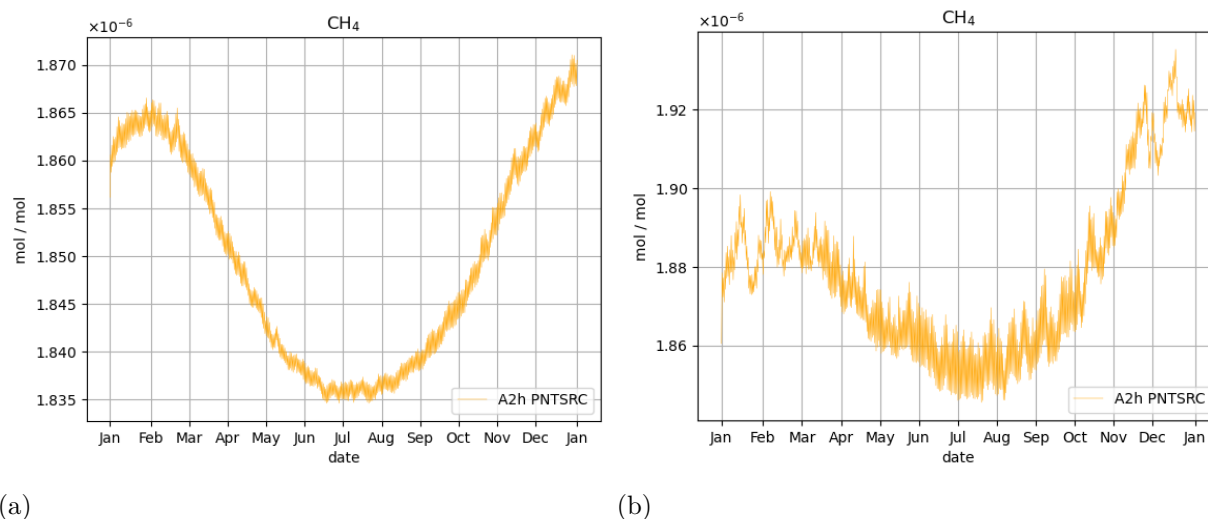
Figure 5.15: Time series of mean methane VMR from simulation A2h PNTSRC on a global (a) and European scale (b).

An overview of the maximum, minimum and mean methane VMR for the R2B5 and R2B6 simulations is presented in Table 5.1. We recognize lower methane VMR in the higher resolved simulations A2h PNTSRC and B3h WALLACE compared to the R2B5 grid, whereas the differences in the minimum, maximum and mean methane VMR of B3(h) WALLACE and A2(h) PNTSRC are quite similar in both resolutions. The mean impact of all adjusted NSR emissions (B3(h) WALLACE - Z ZERO) is also similar on a global (0.1926 ppbv for R2B5 and 0.1871 ppbv for R2B6) and European scale (1.17 ppbv for R2B5 and 1.083 ppbv for R2B6) with slightly lower values for the higher resolved R2B6 grid.

Table 5.1: Overview of the minimum, maximum and mean methane VMR in ppbv in the R2B5 and R2B6 simulations.

	R2B5 global	R2B6 global	R2B5 Europe	R2B6 Europe
A2(h) min	1853.8	1834.56	1861.04	1845.47
A2(h) max	1909.69	1871.06	2012.35	1935.4
A2(h) mean	1872.79	1849.74	1925.64	1877.86
B3(h) min	1853.84	1834.6	1861.06	1845.72
B3(h) max	1909.77	1871.13	2012.62	1935.62
B3(h) mean	1872.83	1849.78	1925.9	1878.07
B3(h) - A2(h) min	0.0008	0.0059	0.0169	0.0459
B3(h) - A2(h) max	0.0829	0.0754	0.7127	0.637
B3(h) - A2(h) mean	0.0442	0.0415	0.2633	0.2164
B3(h) - Z(h) min	0.0023	0.0057	0.0819	0.1942
B3(h) - Z(h) max	0.3315	0.3222	3.497	3.681
B3(h) - Z(h) mean	0.1926	0.1871	1.17	1.083

As visible in Figure 5.16, the spatial accuracy of the pointsource emissions on the R2B6 grid is much higher than on the R2B5 grid. Although, higher resolved grids would improve the quantification of emissions with the WALLACE workflow, as the highlighting of hotspot areas, which is done by the Pattern Algorithm, would be much more accurate, it is associated with computational costs that are about three times higher. The nesting abilities of ICON-ART can be an appropriate solution to this problem.

(a) (b)
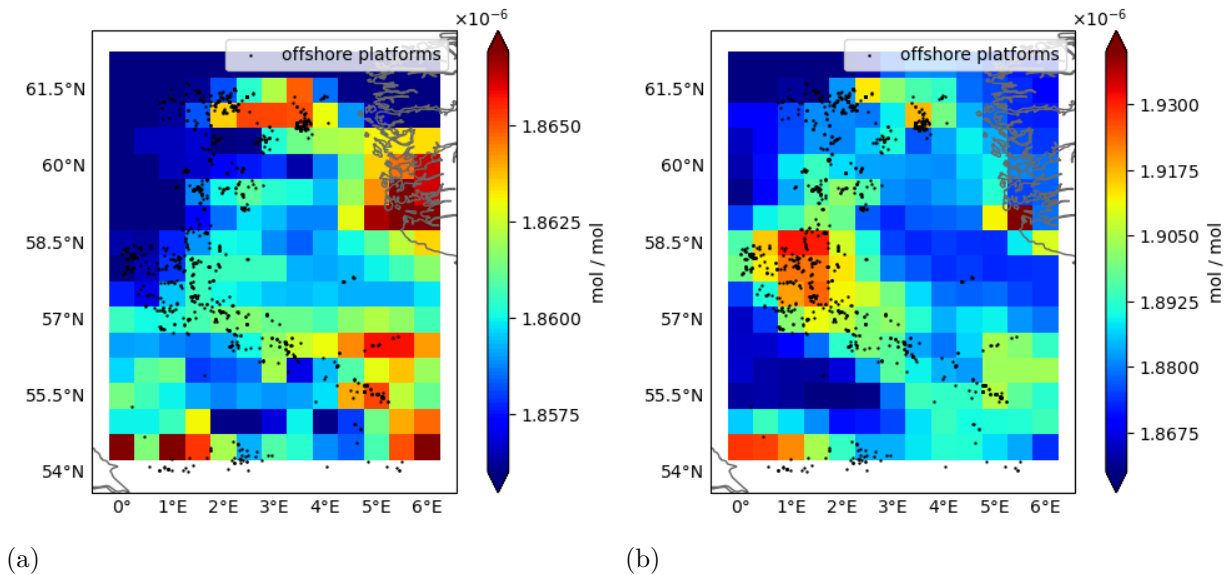
Figure 5.16: Comparison of spatial accuracy of pointsource emissions in R2B5 (a) and R2B6 grid (b).

Finally, we take a look at the simple OH-chemistry on the R2B6 grid. As displayed in Figure 5.17, the anti-correlation of $\Delta\,CH_4$ and $\Delta\,OH$ from A2h PNTSRC - Zh ZERO is clearly visible with r = -0.88. Compared to the R2B5 grid this is a very similar result where we achieved a Pearson correlation coefficient of r = -0.87, leading to the conclusion that the aforementioned factors like vertical and horizontal transport of trace gases play an important role within the OH-chemistry mechanism, independent from the spatial resolution of the grid.
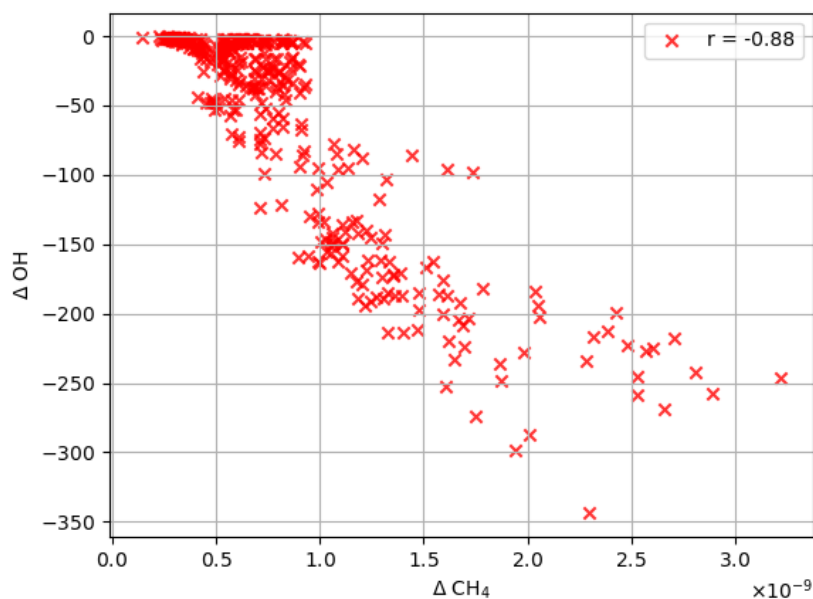
Figure 5.17: Correlation of $\Delta\,CH_4$ and $\Delta\,OH$ on R2B6 grid.

5.7 Computing time analysis

In this section we analyse the simulations that were made on the HPC system HoreKa of SCC at KIT from a technical point of view. Before that, we take a look at scaling tests on HoreKa and compare simulations that were performed on both, HoreKa and its predecessor cluster, the ForHLR II. Additionally, we evaluate the energy consumption and carbon footprint of this work.

We performed scaling tests on the HoreKa HPC system to evaluate the speed and the efficiency of parallel processing within ICON-ART simulations on the cluster. As visible in Figure 5.18 (a) the mean time between two output time steps decreases with an increasing number of nodes being used. For all simulations the total number of 76 cores per node were allocated. We recognize a speed-up of factor 2 while doubling the number of nodes up to sixteen. As mentioned before we use a total number of 20 nodes for the simulations that were performed within this work.

Figure 5.18 (b) displays the runtime of simulations Z ZERO, A1 GRIDDED and A2 PNTSRC as performed on ForHLR II and HoreKa. Due to different setups (additional loop for removing emissions in the NSR and usage of pointsource module) their total runtimes show small differences. A remarkable fact is the speed-up of factor 3 between the two HPC systems.

(a)   (b)
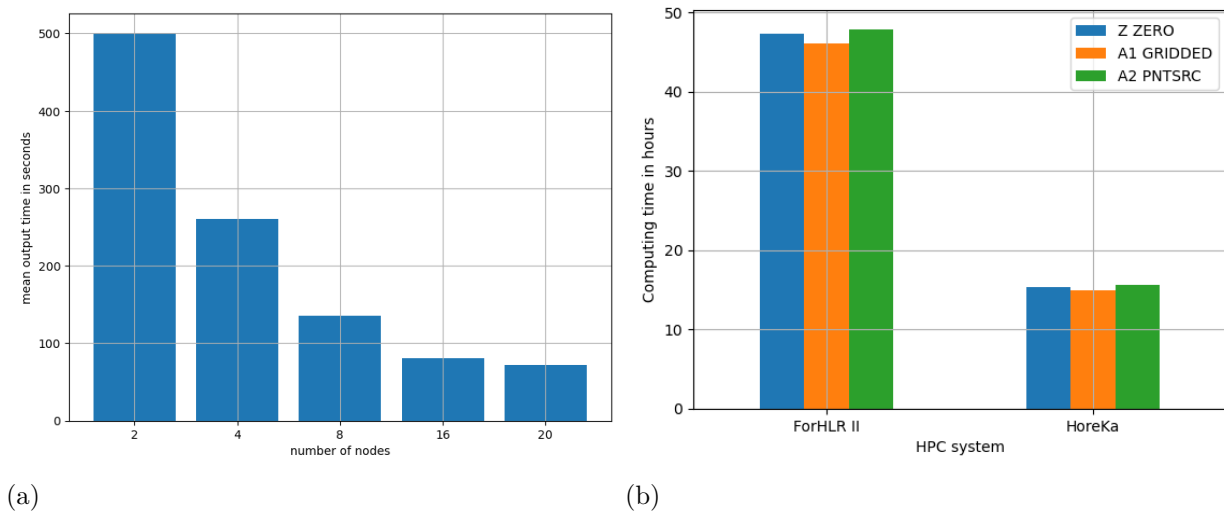
Figure 5.18: Scaling tests on the HoreKa system show a decrease in the mean output timestep with an increasing number of nodes (a). Compared to the ForHLR II simulations on HoreKa are about 3 times faster (b).

As outlined previously in this thesis, the simulations mainly differ in the type of emissions used (gridded or pointsource) and the extra loop that was implemented into the source code to remove gridded emissions in the NSR. The results including the runtime in hours, the HPC resources in CPUh and the energy consumption in kWh are listed in Table 5.2.

Table 5.2: ICON-ART 2.6.3 computing time on the HoreKa HPC system. Displayed are the number of pointsources included, if an extra loop for the removal of NSR emissions is used, the runtime in hours, the resources in CPUh and the energy consumption in kWh for the R2B5 simulations Z ZERO, A1 GRIDDED, A2 PNTSRC, B1 EDGAR, B2 EDGAR+ and B3 WALLACE such as the R2B6 simulations Zh ZERO, A2h PNTSRC and B3h WALLACE.

simulation	#PntSrc	loop	time [h]	resources [CPUh]	energy [kWh]
Z ZERO	0	y	15.37	46694.4	248
A1 GRIDDED	0	n	14.96	45478.4	242
A2 PNTSRC	2604	y	15.6	47424	252
B1 EDGAR	3656	y	16.48	50099.2	266
B2 EDGAR+	0	n	15.12	45964.8	244
B3 WALLACE	3656	y	16.15	49096	261
Zh ZERO	0	y	46.63	141755.2	718
A2h PNTSRC	2604	y	47.48	144339.2	731
B3h WALLACE	3656	y	47.26	143670.4	728
		sum	**235.06**	**714521.6**	**3690**

The runtimes for the R2B5 simulations on HoreKa vary from 14.96 h for simulation A1 GRIDDED, which neither used the pointsource module nor the extra loop, to 16.48 h for simulation B1 EDGAR, where both extras were implemented. It is recognizable that, due to differences in the communication between the nodes, simulation B3 WALLACE is about 20 minutes faster than simulation B1 EDGAR, which has the same setup with just a different source strength of the pointsources. The runtime of all six R2B5 simulations together is 93.69 h using a total amount of 284756.8 CPUh of process time. If we add up the additionally performed simulations Zh ZERO, A2h PNTSRC and B3h WALLACE on the higher resolved R2B6 grid, we end up with a total runtime of 235.06 h or 9.8 days and a total amount of 714521.6 CPUh of process time. This underlines the significantly high computational costs of modeling on high resolved global grids.

The calculation of the energy consumption depends on a couple of factors like the concrete type of computational tasks which are performed, the number of nodes and cores, the parallel interactions, the usage of memory such as the in- and output processes. For a

simulation time of one hour with 20 nodes and the maximum of 76 cores per node a ICON-ART simulation on HoreKa consumes a total of about 15.4 kWh (Raffeiner, 2021). For cooling purposes the SCC estimates an additional 5 % of the total amount of consumed energy per simulation which leads to the values in Table 5.2. For the R2B5 simulations they vary from 242 kWh for simulation A1 GRIDDED up to 266 kWh for simulation B1 EDGAR what leads to a total amount of consumed energy of 1513 kWh, as much as an average one-person household in Germany in 2019 needed for its electrical devices (destatis, 2021). Adding up the R2B6 simulations again, all model runs consumed a total amount of 3690 kWh. With these results and the Greenhouse Gas Equivalent Calculator provided by the United States Environmental Protection Agency (EPA) we derived a carbon footprint for the simulations performed within this work of 2.6 t CO_2eq, what equals the CO_2 emissions from over 1113 liters of gasoline being consumed, 107 propane cylinders being used for home barbeques or almost 318 000 smartphones being charged (EPA, 2021).

6 Conclusion and Outlook

Within this work three methods for the adjustment of anthropogenic GHG emissions were introduced. Beside a straight-forward upscaling method and a regridding based on reported emission data (EDGAR+), we presented the WALLACE workflow, a new and innovative method to quantify GHG emissions based on TROPOMI measurements from the S5P satellite. WALLACE contains several new workflows such as an interpolation routine to remap unstructured Level 2 data and create a new regular Level 3 product (Sentinel-5P Level 3 processor). Moreover, the Pattern Algorithm, a selection algorithm that aims in highlighting emission hotspots, was developed and tested. We additionally implemented workflows to make WALLACE a highly flexible pre-processing tool for atmospheric models. Furthermore, an idealized setup for the ICON-ART model was designed and simulations with different emission inputs were performed to compare the adjustment methods and evaluate the impact of oil and gas platform emissions on the global and regional GHG budget. Moreover, we performed simulations on a higher resolved grid to evaluate differences in the resulting VMR and the spatial accuracy of the output. Our results show that the emission fluxes quantified by WALLACE have a high degree of spatial and temporal accuracy. Additionally, WALLACE reveals an impact of the missing emissions on the spatial distribution of methane and its global and regional budget.

The EDGAR+ regridding approach led to much lower GHG VMRs and even underestimated the actual emissions which are included in EDGAR. This leads to the conclusion, that the reported emissions from OSPAR (2019) are too low compared to the EDGAR emission inventory and the resulting values from the WALLACE workflow. Nevertheless, the EDGAR inventory also assesses too less emissions for methane, ethane, propane and carbon monoxide in the NSR. In addition to that, some of the sources are completely missing due to incomplete proxy data and inconsistencies in the emission reporting process. Many recent studies like Saunois et al. (2016a), Hoesly et al. (2018), Liu et al. (2021) and Solazzo et al. (2021) address these uncertainties of EDGAR. The study of van Damme et al. (2018) reveals, that many industrial hotspots within EDGAR are displaced up to

two pixels or 20 km from their actual location and, in addition to that, are largely underestimated compared to IASI data. Globally, Solazzo et al. (2021) find that the EDGAR emissions for the three main GHGs are accurate within an interval of -15 % to +20 % but depending on the region of interest and the emission sector, these uncertainties can be much higher (up to ±100 %). For the oil and gas platforms in the NSR these uncertainties are mainly caused by leakage as shown by Riddick et al. (2019).

As emission inventories like EDGAR are important tools for policymakers it is very important to include missing emissions properly and reduce the uncertainty that is caused by incomplete proxy data and the inconsistencies in the reporting processes. One possibility would be the combination of global GHG databases like EDGAR with sector-specific and regional inventories (e.g. Scarpelli et al., 2020). Concerning the reporting obligations of GHG emissions on a national level, the expert council on climate issues in Germany draws the conclusion, that a minority of the data is based on real measurements, most of them being still provisional. A much larger proportion is based on estimates from different institutions with various additional assumptions that have to be taken (Expertenrat für Klimafragen, 2021). This inevitably leads to errors in the datasets of well-established inventories like EDGAR. For these reasons, the WALLACE workflow will be applied to different showcases, especially on the land surface, in the future. Since the TROPOMI data offer a much higher spacial resolution, up to $0.1° \times 0.1°$ (see e.g. Tu et al. (2021)), WALLACE will also be tested on a more regional level to derive emissions from factories, megacities or other emission hotspots. In these cases, accompanying measurement campaigns would be optimal to validate the results of WALLACE.

Concerning the ICON-ART model, the implementation of a full gas phase chemistry mechanism as explained in Weimer (2019) would guarantee a higher informative value on the interaction of chemical species in the troposphere. In addition to that, the highly flexible nesting abilities of ICON-ART can be used to investigate GHG budgets on a regional level more precisely with relatively low computational costs, compared to high resolved global simulations.

This work makes a new and innovative contribution to achieve an accurate quantification of GHG emissions and thus the reduction of environmentally harmful gases that drive man-made climate change.

Appendices

A EDGAR sector-specific emission fluxes

In this Appendix we present the sector-specific emission fluxes of the EDGAR 4.3.2 monthly inventory (Janssens-Maenhout et al., 2019) for the species CO (see Figure A.1), C_2H_6 (see Figure A.2) and C_3H_8 (see Figure A.3) in the same way as shown for CH_4 in Figure 4.2.
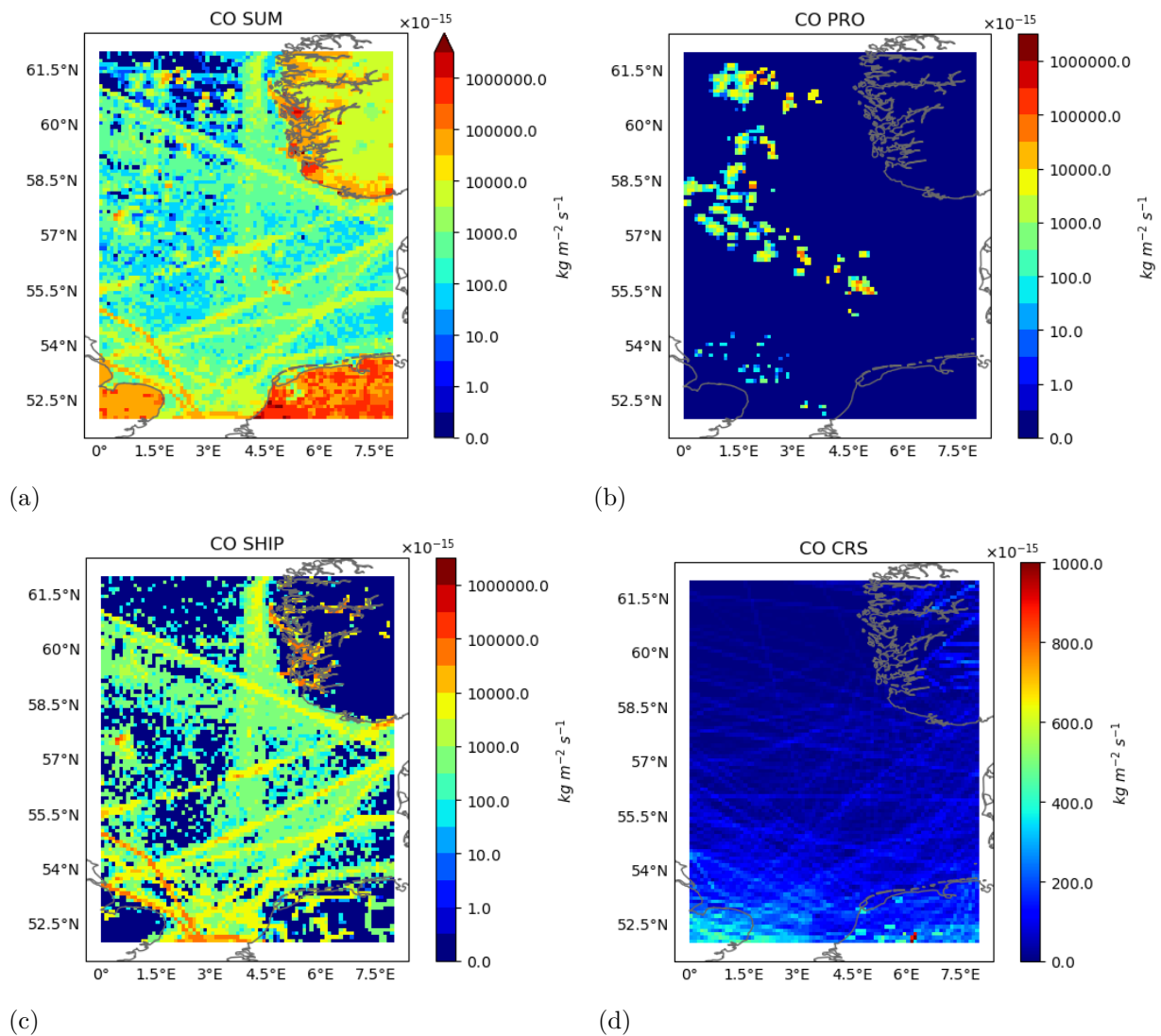
Figure A.1: Collection of EDGAR sectors with carbon monoxide emissions over water in the NSR. Displayed are SUM (a) and the sectors PRO (b), SHIP (c) and CRS (d). Note the smaller scale of the CRS sector.
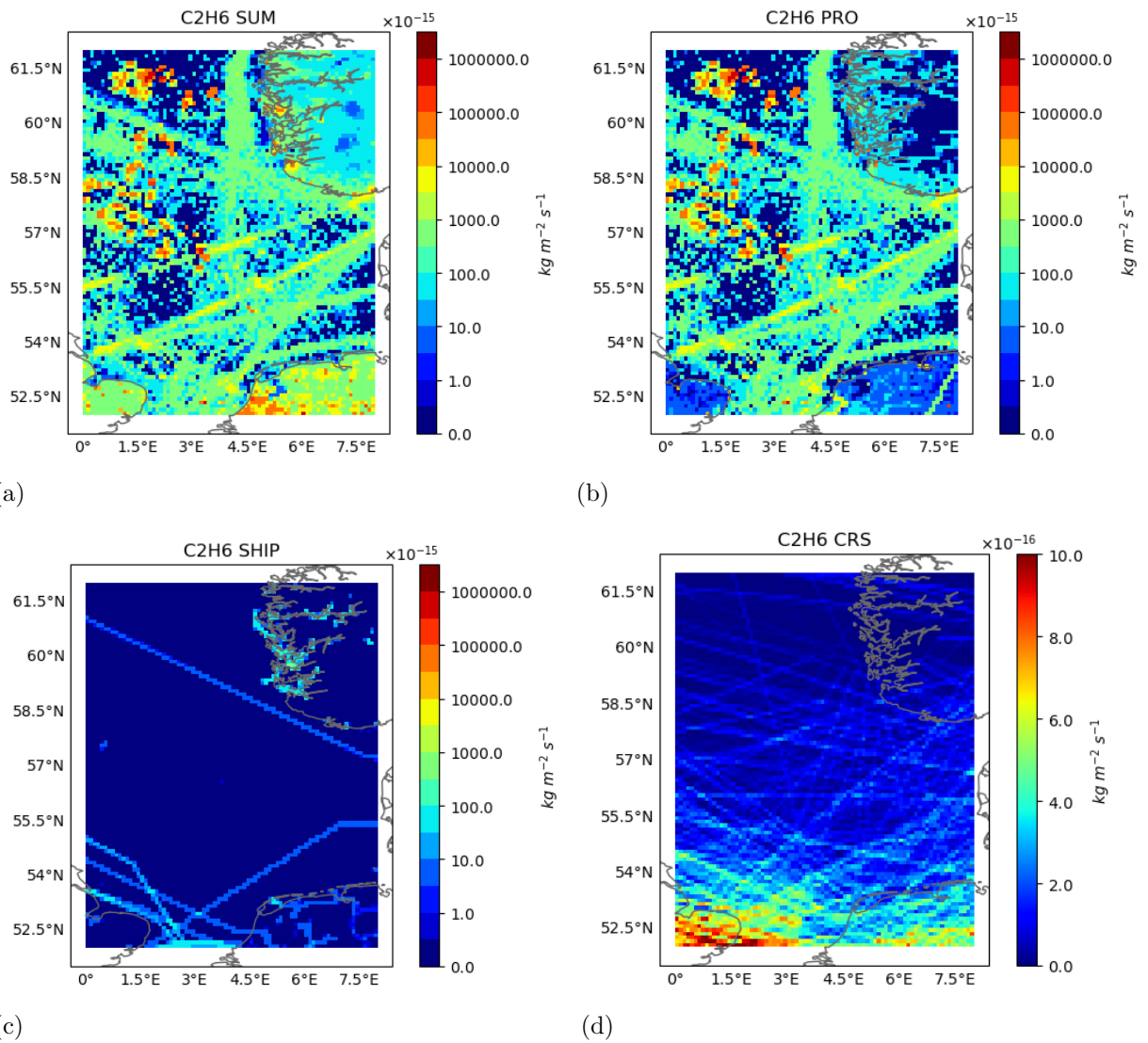
Figure A.2: Collection of EDGAR sectors with ethane emissions over water in the NSR. Displayed are SUM (a) and the sectors PRO (b), SHIP (c) and CRS (d). Note the smaller scale of the CRS sector.

(a)

(b)

(c)

(d)
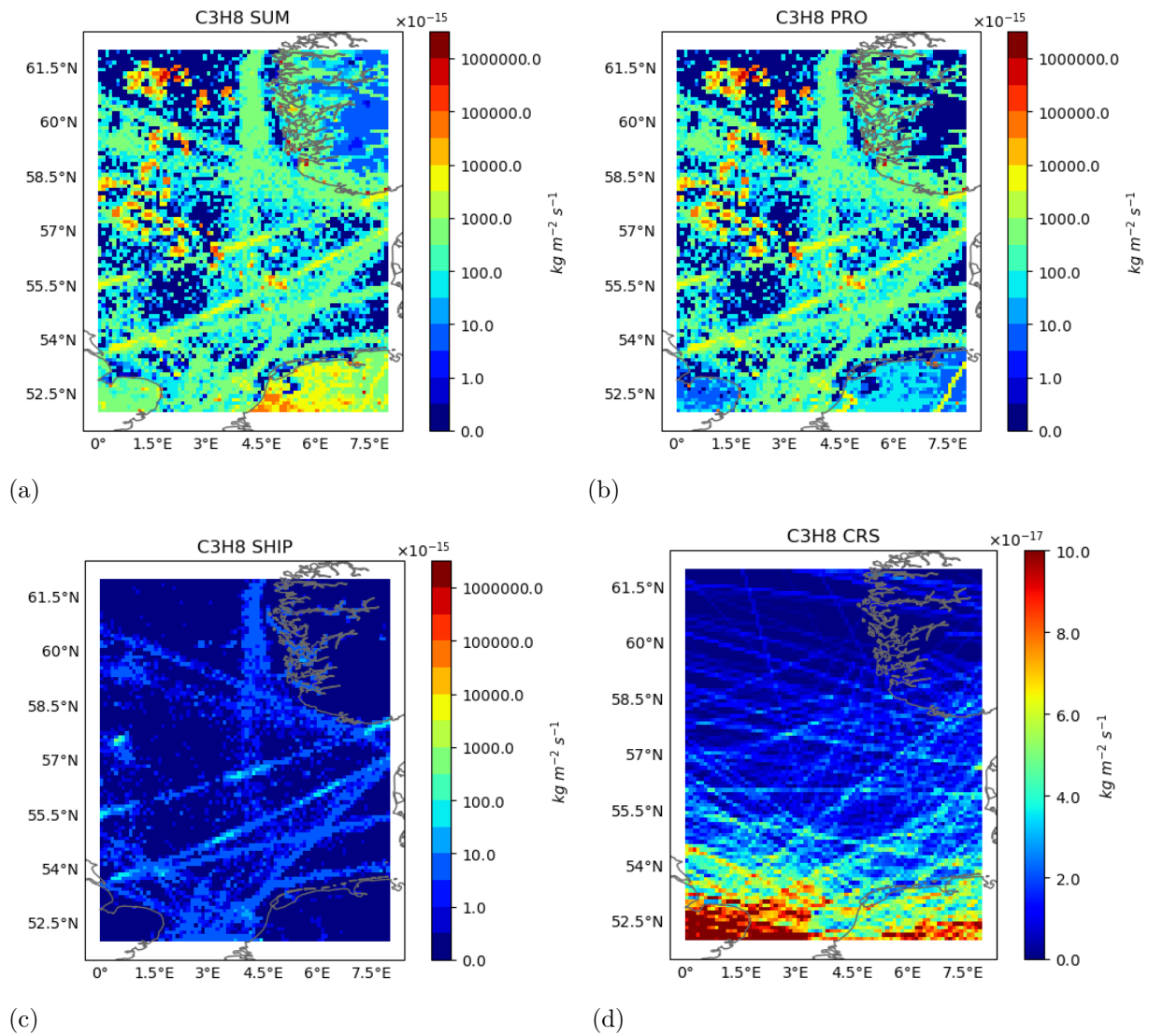
Figure A.3: Collection of EDGAR sectors with propane emissions over water in the NSR. Displayed are SUM (a) and the sectors PRO (b), SHIP (c) and CRS (d). Note the smaller scale of the CRS sector.

B EDGAR+ emission fluxes

This Appendix gives an overview of the new EDGAR+ emission fluxes for all four species: CH_4 (see Figure B.1), CO (see Figure B.2), C_2H_6 (see Figure B.3) and C_3H_8 (see Figure B.4). For a better comparison the original EDGAR fluxes with and without the emissions at platform locations are displayed. Additionally these graphics illustrate the workflow of the processing of the new gridded emission product EDGAR+.
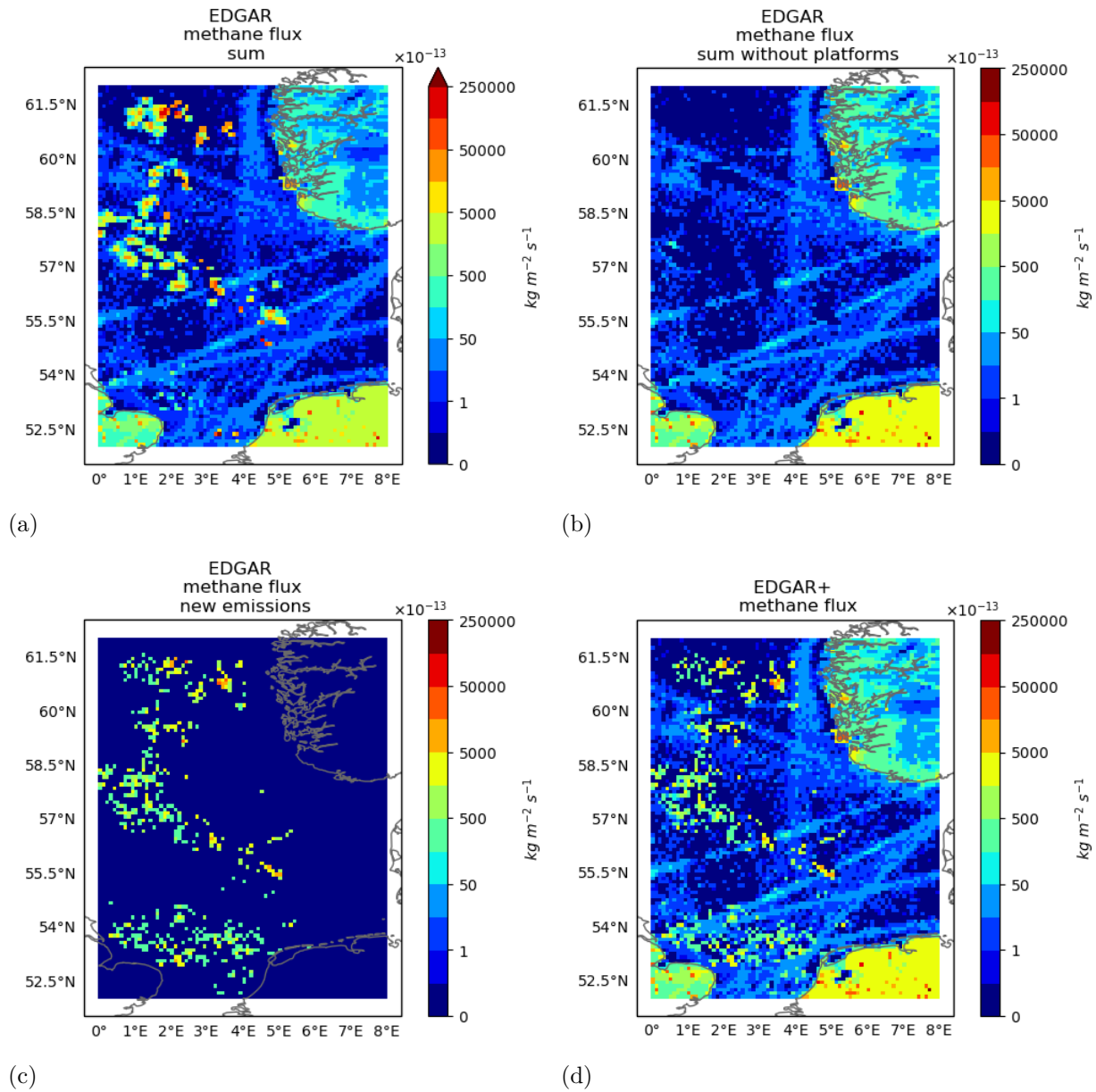
Figure B.1: Comparison of methane in EDGAR and EDGAR+. Displayed are the total sum in EDGAR with (a) and without platforms (b), the new platform emissions of EDGAR+ (c) and the final gridded product EDGAR+ (d).
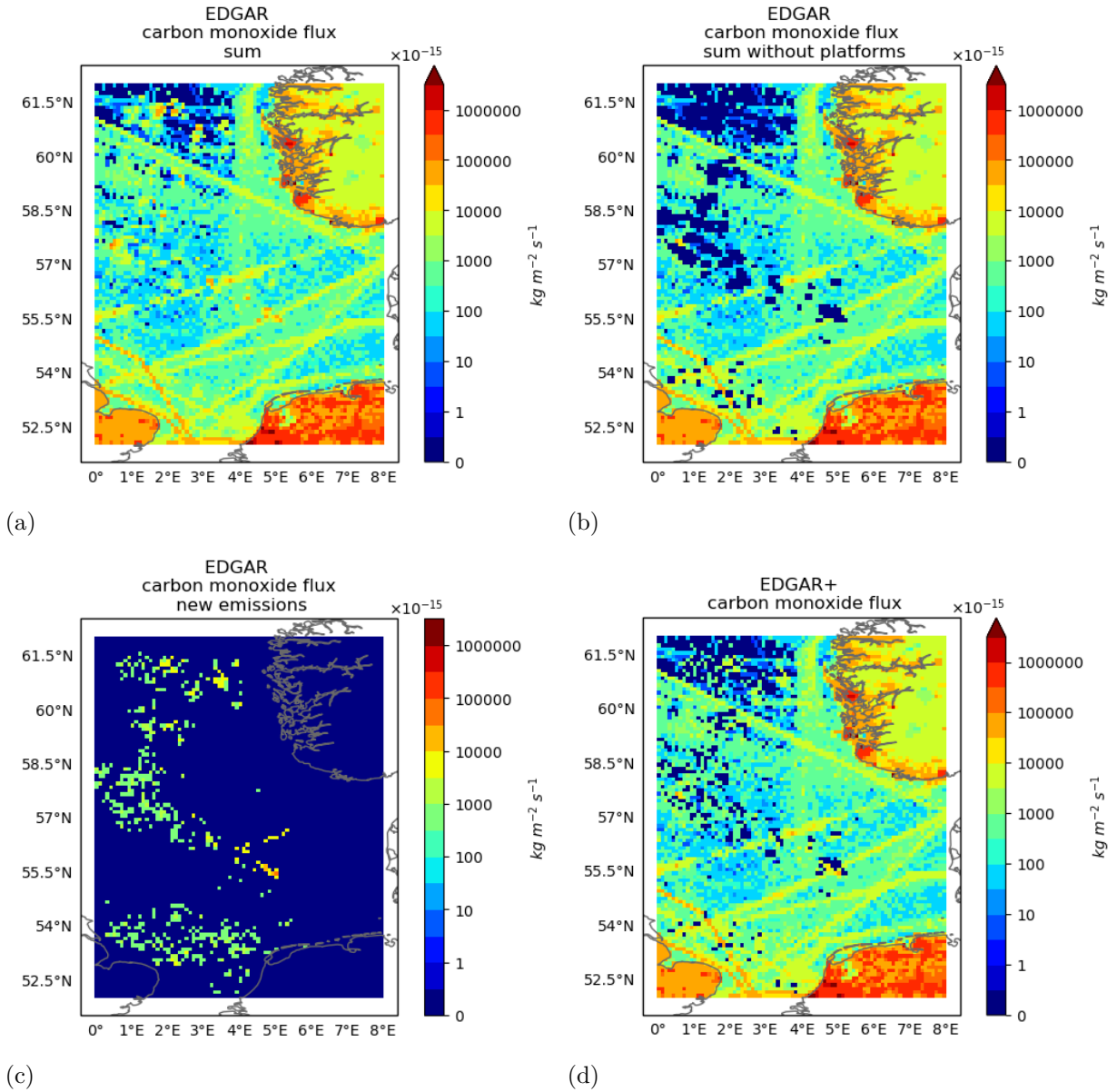
Figure B.2: Comparison of carbon monoxide in EDGAR and EDGAR+. Displayed are the total sum in EDGAR with (a) and without platforms (b), the new platform emissions of EDGAR+ (c) and the final gridded product EDGAR+ (d).
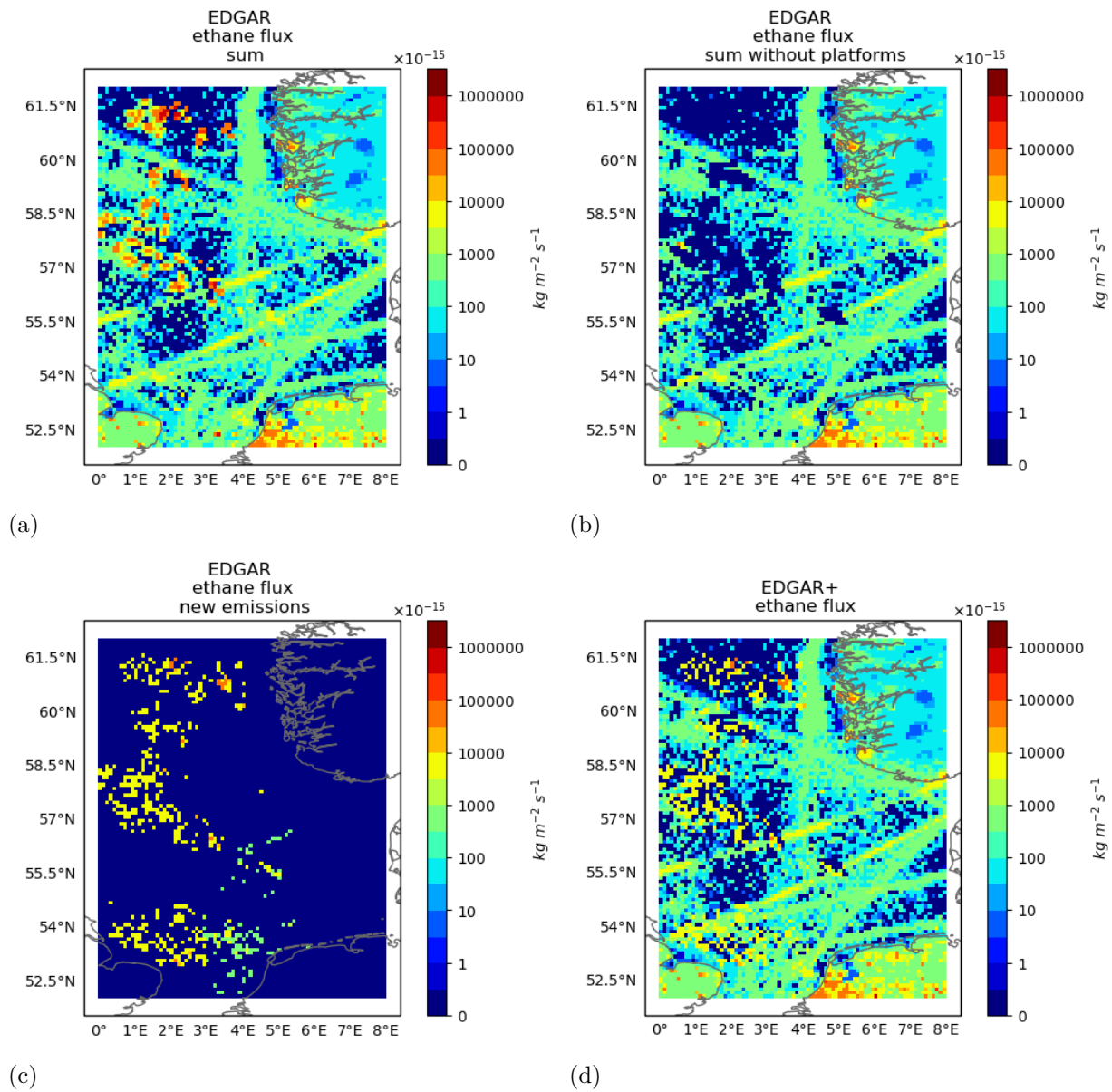
Figure B.3: Comparison of ethane in EDGAR and EDGAR+. Displayed are the total sum in EDGAR with (a) and without platforms (b), the new platform emissions of EDGAR+ (c) and the final gridded product EDGAR+ (d).
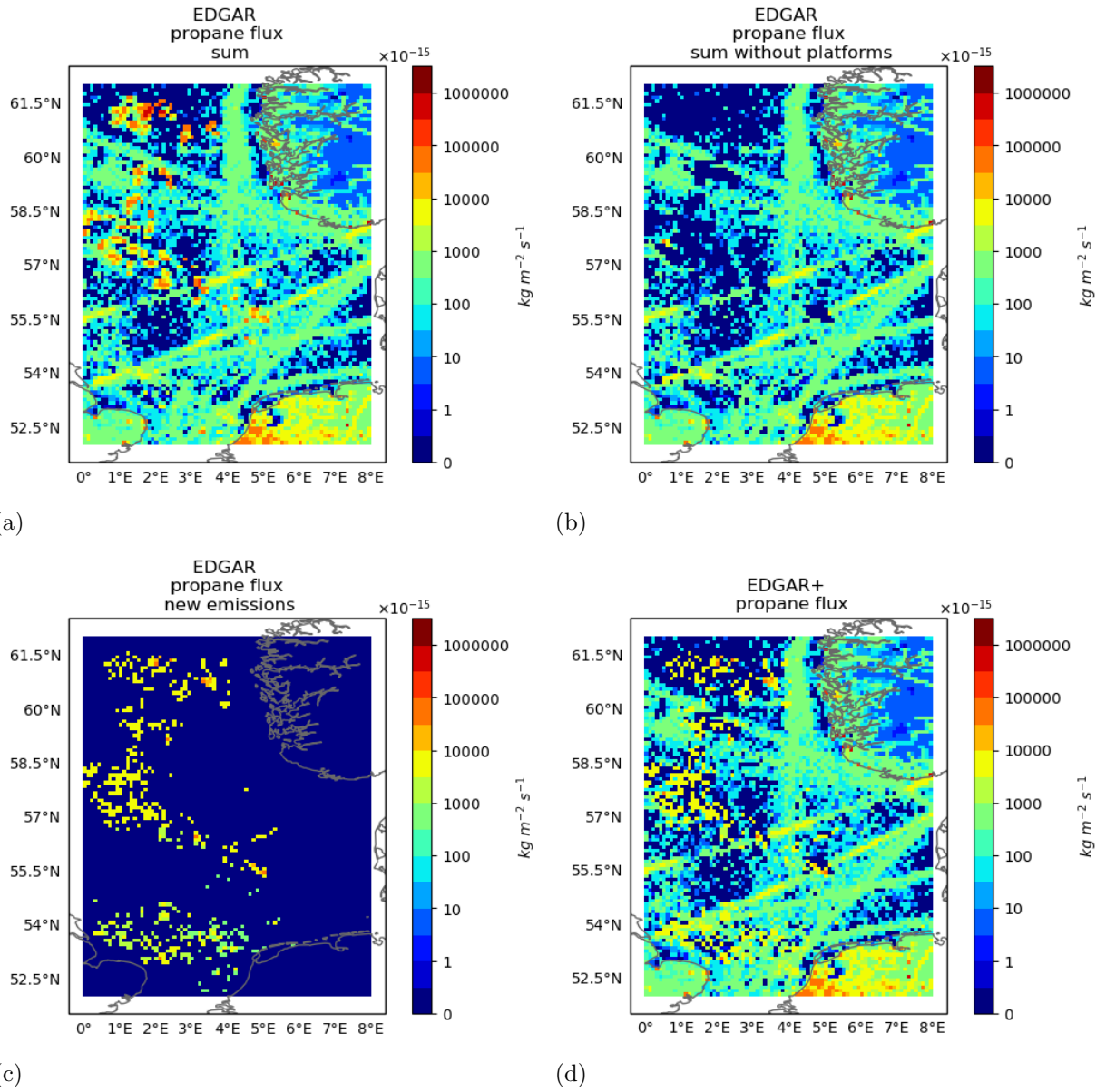
Figure B.4: Comparison of propane in EDGAR and EDGAR+. Displayed are the total
sum in EDGAR with (a) and without platforms (b), the new platform
emissions of EDGAR+ (c) and the final gridded product EDGAR+ (d).

C Pattern Algorithm - Random pattern

Nine random patterns were created and used as input for the Pattern Algorithm. The random pattern and their mean methane VMR together with component-wise mean wind after applying the Pattern Algorithm are displayed in this Appendix. The results show that the Pattern Algorithm works appropriately selecting time steps with high methane VMR in each corresponding P1. But decisively the usage of patterns different to the platform pattern shown in Figure 4.10 (b) lead to wind that obviously caused the high values in the random patterns. This shows, that with random patterns no hotspots are highlighted but the Pattern Algorithm just selects time steps with certain wind conditions.
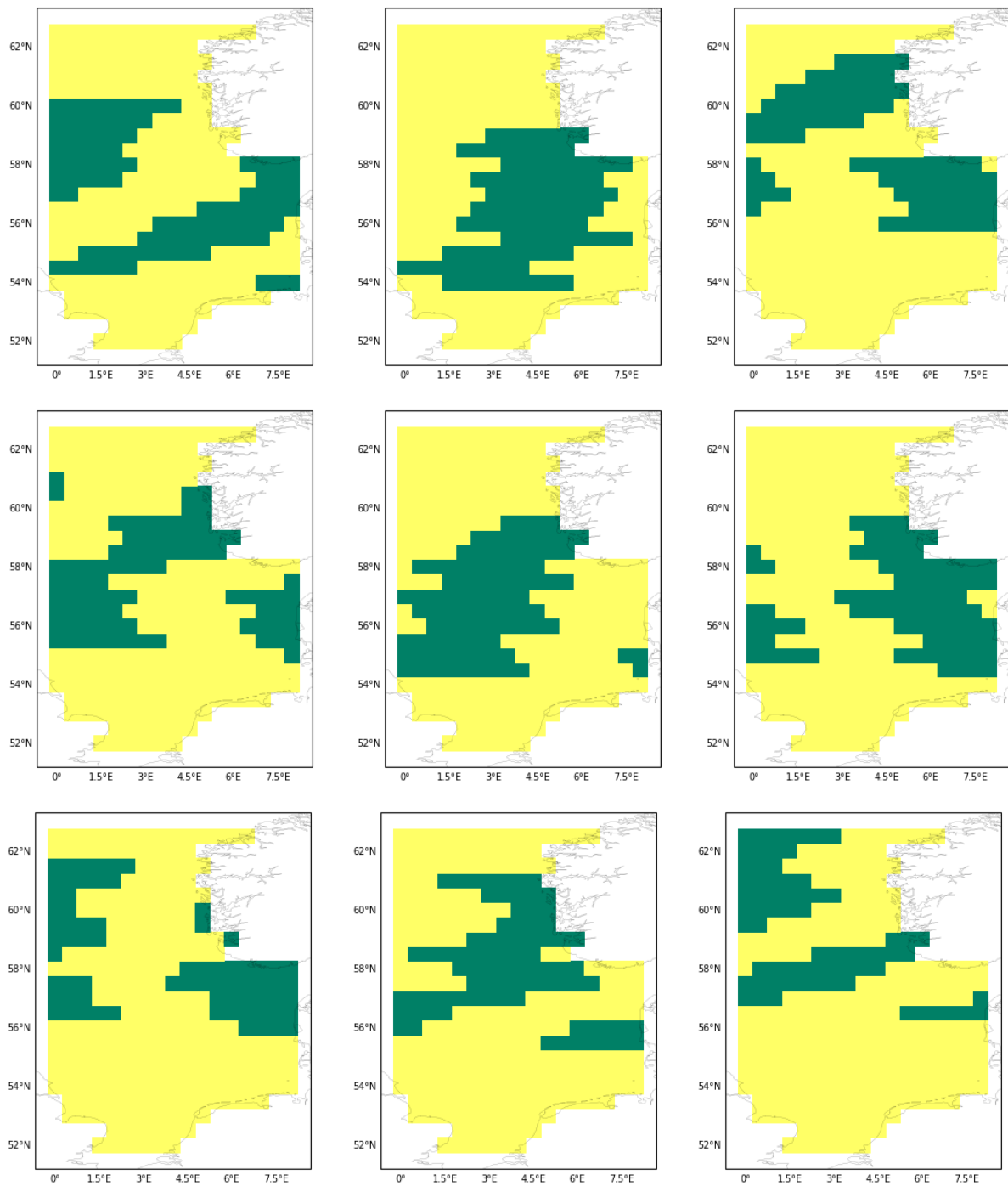
Figure C.1: The nine randomly created pattern to evaluate the wind dependency of the results from the algorithm. Land masking was activated here as in the reference pattern, too.
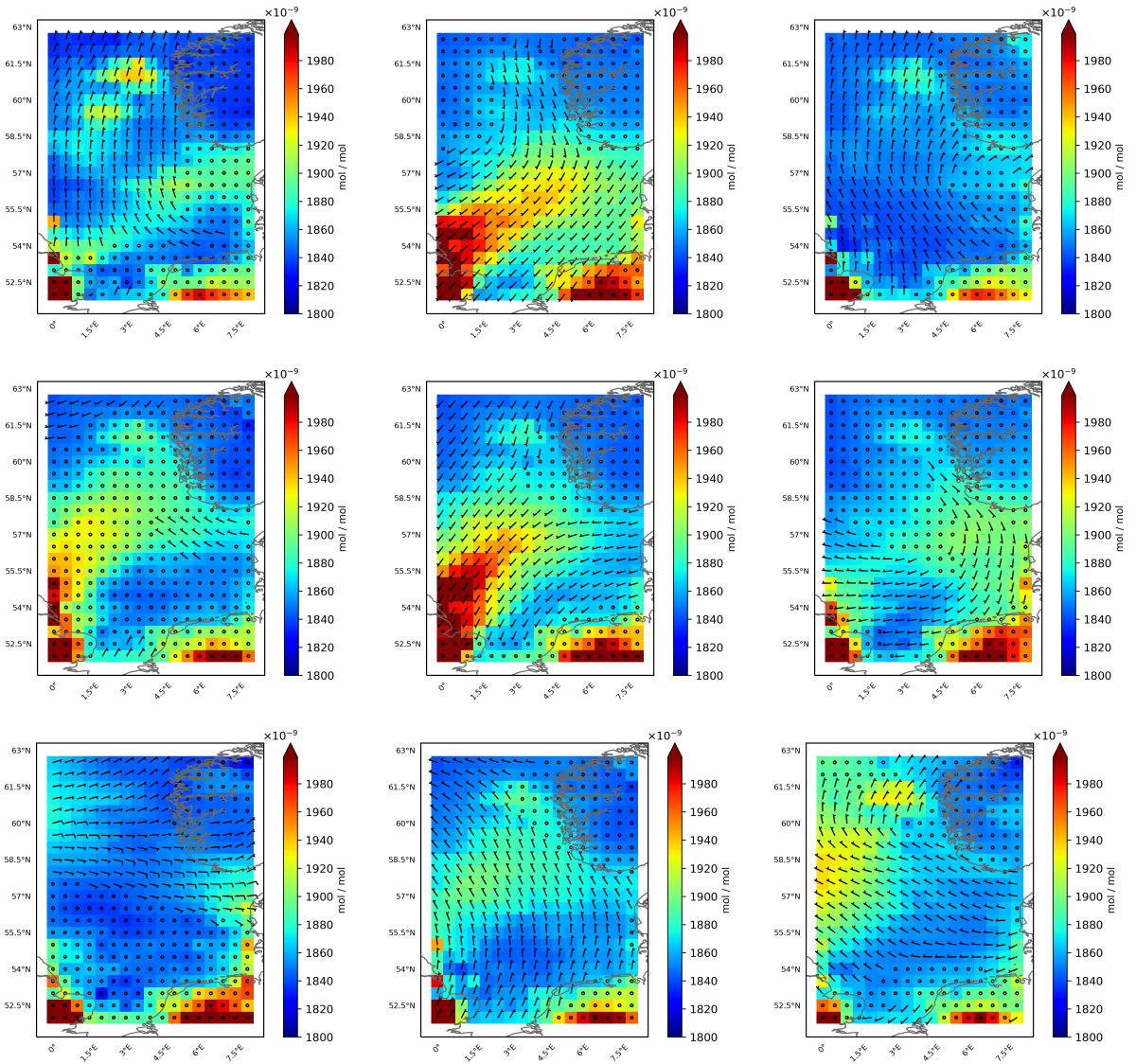
Figure C.2: The nine arithmetic means of the selections made by the algorithm for the randomly created pattern. The component-wise mean of the wind shows that the relatively high values inside P1 are wind dependent (transported from the land surface) and therefore not caused by emission hotspots in the presented area.

D Statistical methods

In this section we introduce the methodology of statistical correlation and we use Henze (2017) as a basis for the content and notation. The examination of a statistical relation between quantitative properties X and Y is a very important method in statistical data analysis. We consider the values at the j-th of n positions of a variable X as x_j and at the j-th of n positions of a variable Y as y_j. Displayed in a scatter plot our goal is to find a regression line $y = a^* + b^*x$ fulfilling the condition of equation D.1.

$$\sum_{j=1}^{n}(y_j - a^* - b^*x_j)^2 \quad = \quad \min_{a,b}\left(\sum_{j=1}^{n}(y_j - a - bx_j)^2\right) \tag{D.1}$$

This *method of least squares* targets the minimization of the squares by an appropriate choise of a and b as shown in Figure D.1.
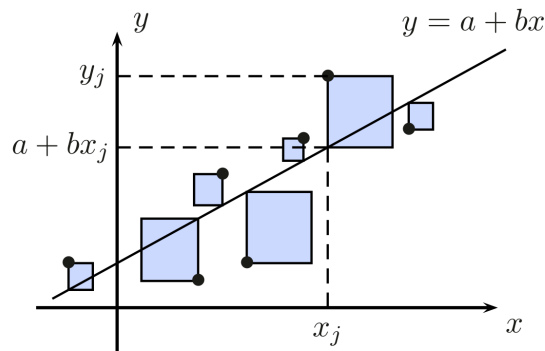
Figure D.1: Method of Least Squares: The sum of all the squares needs to be minimal by an appropriate choice of a and b. Figure is taken from Henze (2017).

We consider (X, Y) to be a two-dimensional random vector being each pair (x_j, y_j) with the same probability $\frac{1}{n}$.

Let

$$\bar{x} \quad := \quad \frac{1}{n}\sum_{j=1}^{n}x_j \qquad \bar{y} \quad := \quad \frac{1}{n}\sum_{j=1}^{n}y_j \tag{D.2}$$

be the arithmetic means of all x_j and y_j,

$$\sigma_x^2 \quad := \quad \frac{1}{n}\sum_{j=1}^{n}(x_j - \bar{x})^2 \qquad \sigma_y^2 \quad := \quad \frac{1}{n}\sum_{j=1}^{n}(y_j - \bar{y})^2 \tag{D.3}$$

the variances of X and Y such as

$$\sigma_{xy} \quad := \quad \frac{1}{n}\sum_{j=1}^{n}(x_j - \bar{x})(y_j - \bar{y}) \tag{D.4}$$

the covariance of X and Y.

Hence with the method of least squares as shown in Figure D.1 and the optimisation proposition in Henze (2017) the best choise of (a^*, b^*) in equation D.1 is

$$b^* \quad = \quad \frac{\sigma_{xy}}{\sigma_x^2} \qquad a^* = \bar{y} - b^* \cdot \bar{x}. \tag{D.5}$$

With this preparatory work and the equations D.2, D.3, D.4 and D.5 we can define the *empirical correlation coefficient from Pearson* as

$$r(X,Y) \quad = \quad \frac{\sigma_{xy}}{\sqrt{\sigma_x^2 \cdot \sigma_y^2}} \quad = \quad \frac{\sum_{j=1}^{n}(x_j - \bar{x})(y_j - \bar{y})}{\sqrt{\sum_{j=1}^{n}(x_j - \bar{x})^2 \cdot \sum_{j=1}^{n}(y_j - \bar{y})^2}}. \tag{D.6}$$

Correlation coefficients are of a high importance for statements about the values of variable Y just because of the knowledge about the values of variable X. The result of $r(X,Y)$ is in the interval $[-1, 1]$ where $r(X,Y) < 0$ means the two random vectors are negative correlated and $r(X,Y) > 0$ indicates a positive correlation. For a better readability we write r for $r(X,Y)$. Further details concerning the statistical methods and the mathematical background can be found in Henze (2017).

E Time series of CO, C_2H_6, C_3H_8 and OH

In this Appendix we present the time series of the species CO, C_2H_6, C_3H_8 and OH. They are shown in Figures E.1, E.2, E.3 and E.4, respectively. For each of the species twelve time series are displayed that correspond to the results shown for CH_4 in Chapter 5. The following list gives an overview of the content of subfigures (a) - (l):

(a) A1 and A2, global mean VMR

(b) A1 and A2, European mean VMR

(c) A1 and A2, Δ of global mean VMR

(d) A1 and A2, Δ of European mean VMR

(e) B1 EDGAR, B2 EDGAR+ and B3 WALLACE, global mean VMR

(f) B1 EDGAR, B2 EDGAR+ and B3 WALLACE, European mean VMR

(g) B1 EDGAR and B3 WALLACE, Δ to simulation A2 of global mean VMR

(h) B1 EDGAR and B3 WALLACE, Δ to simulation A2 of European mean VMR

(i) B2 EDGAR+, Δ to simulation A1 of global mean VMR

(j) B2 EDGAR+, Δ to simulation A1 of European mean VMR

(k) B1 EDGAR and B3 WALLACE, Δ to simulation Z of global mean VMR

(l) B1 EDGAR and B3 WALLACE, Δ to simulation Z of European mean VMR

(a)

(b)

(c)

(d)

(e)

(f)
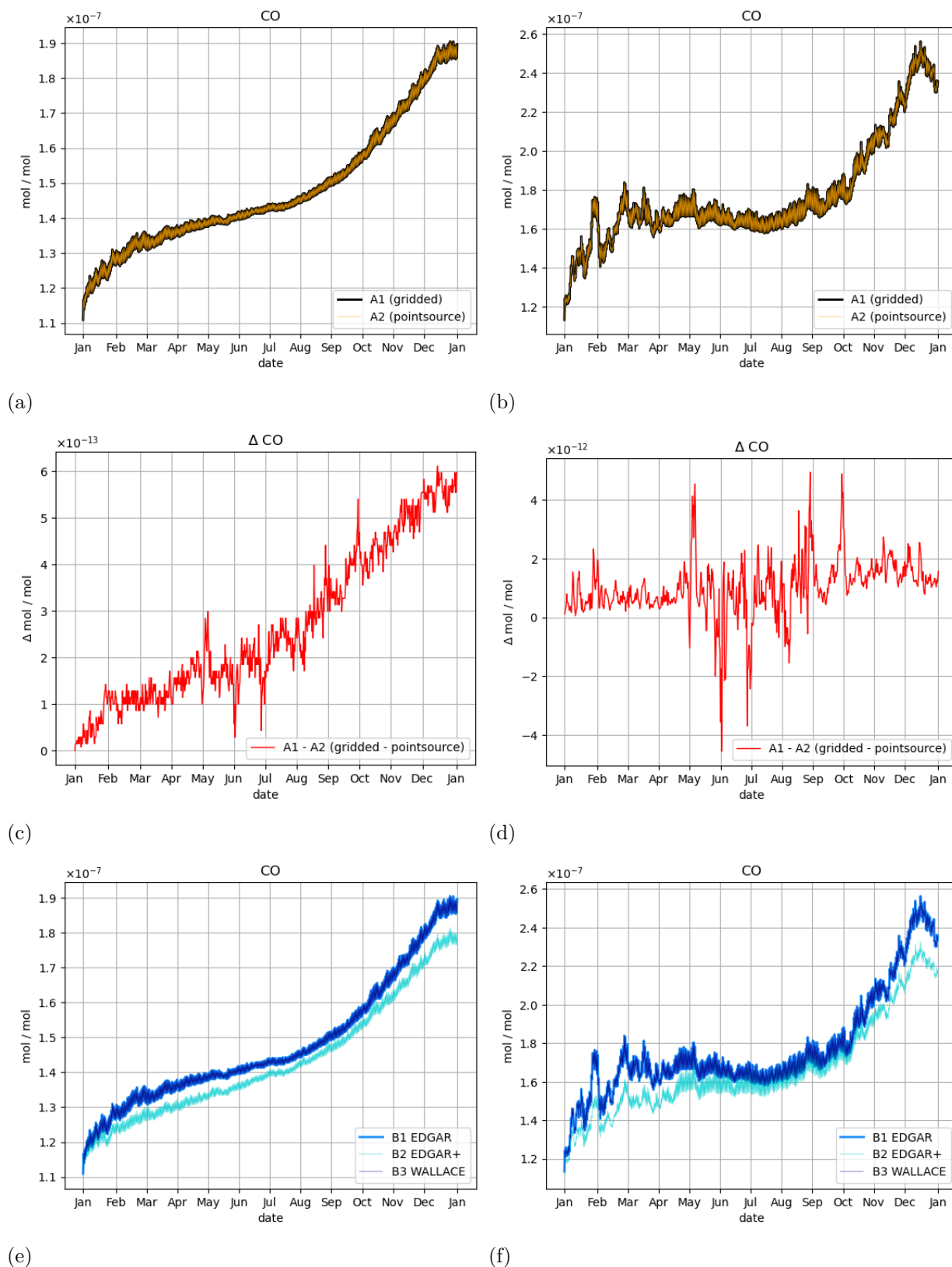
Figure E.1: Time series of CO.
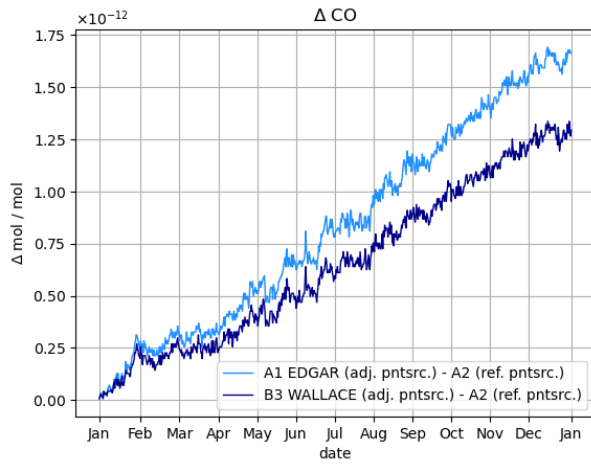
(g)
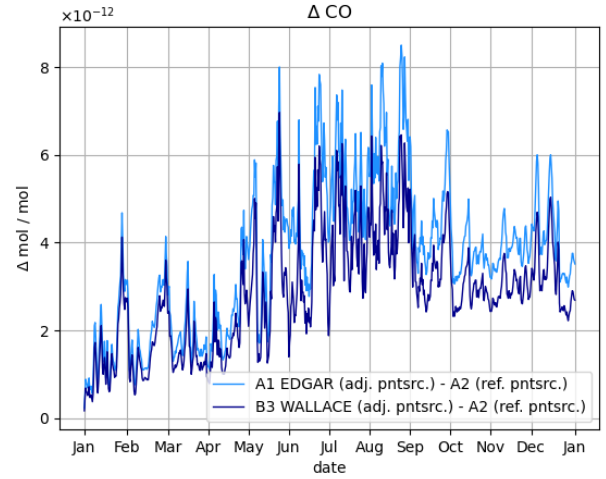
(h)
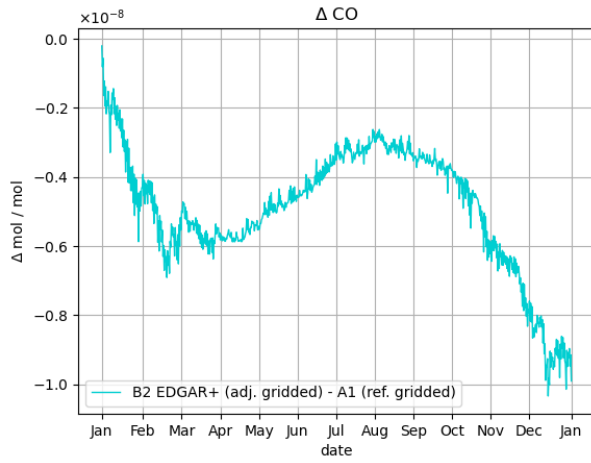
(i)
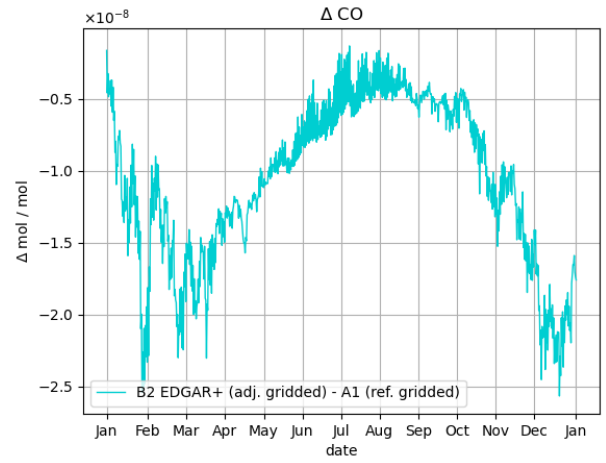
(j)
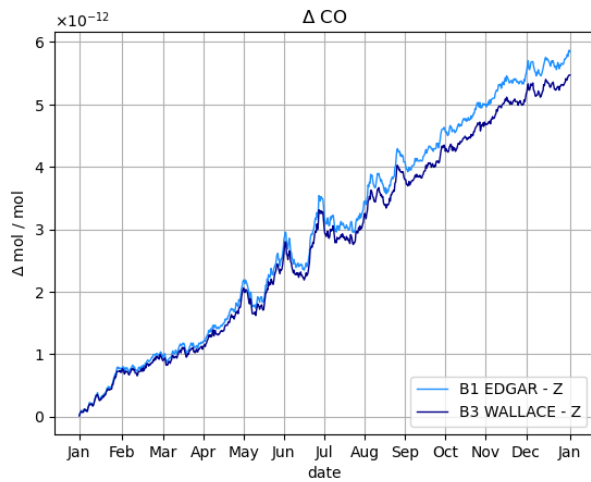
(k)
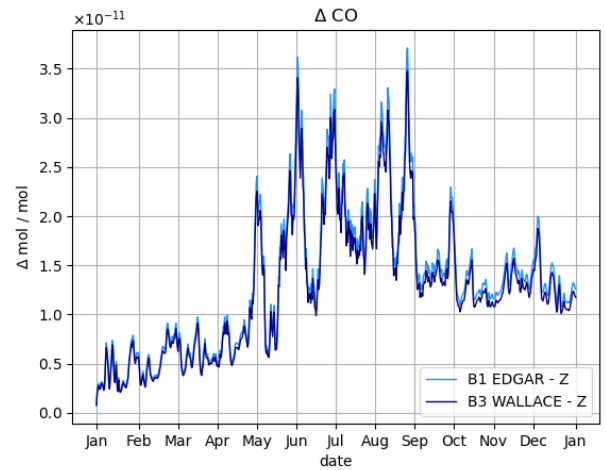
(l)

Figure E.1: Time series of CO (... continued).

(a)

(b)

(c)

(d)

(e)

(f)
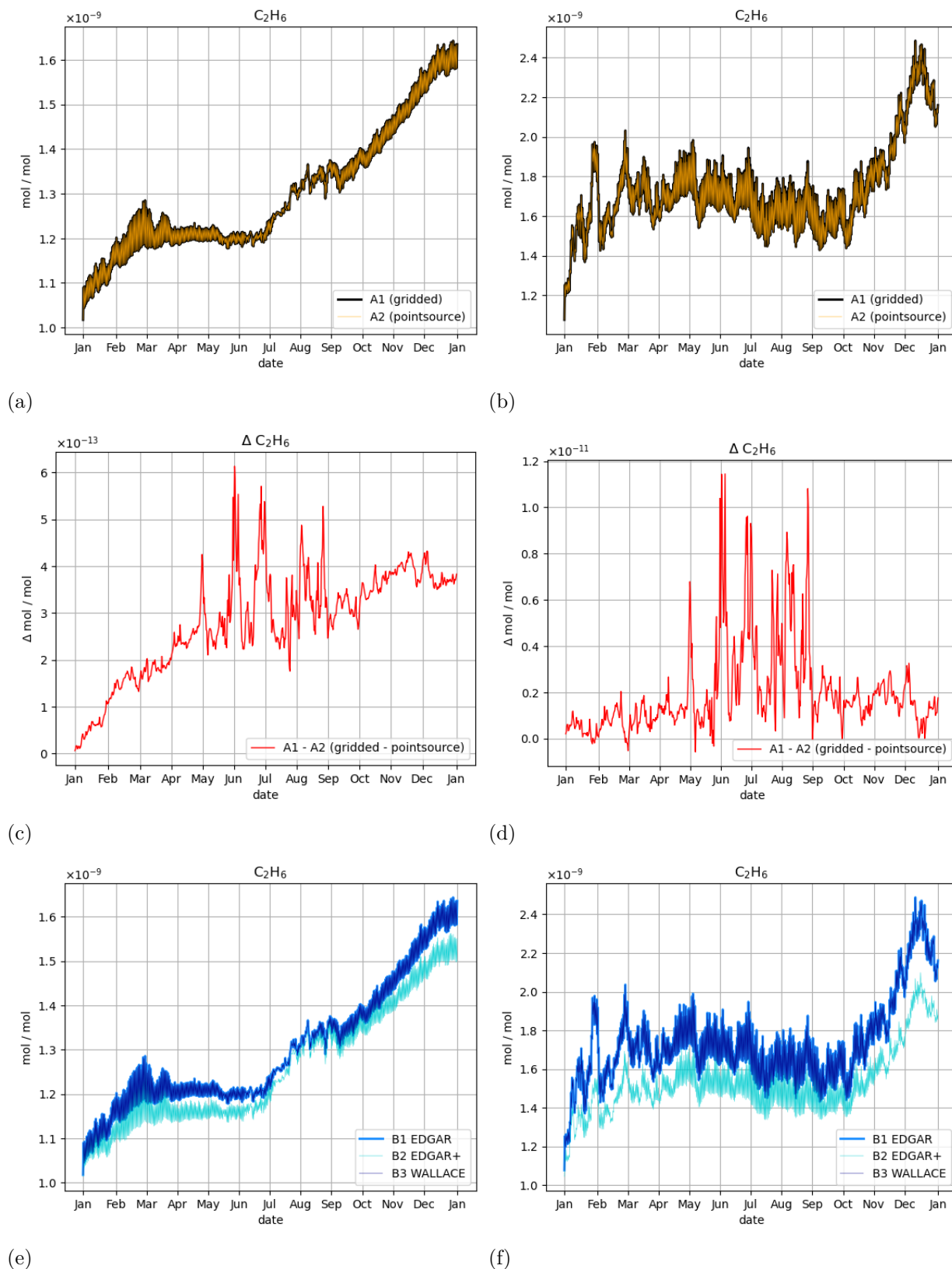
Figure E.2: Time series of C$_2$H$_6$.
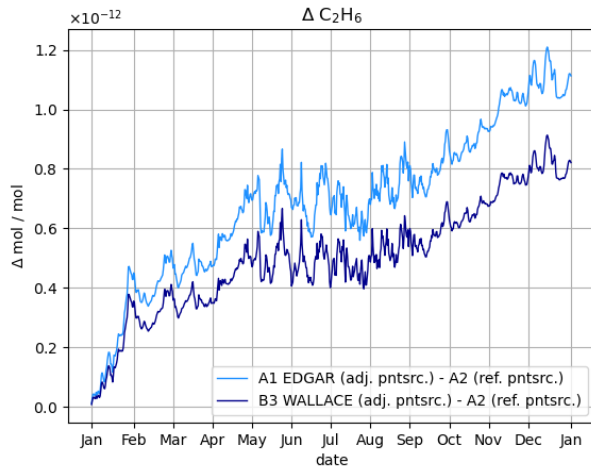
(g)
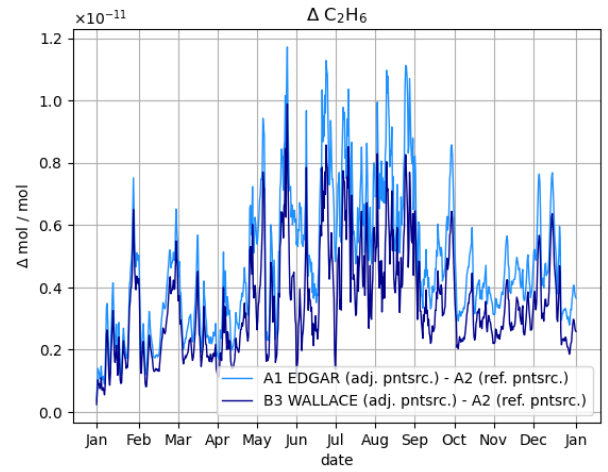
(h)
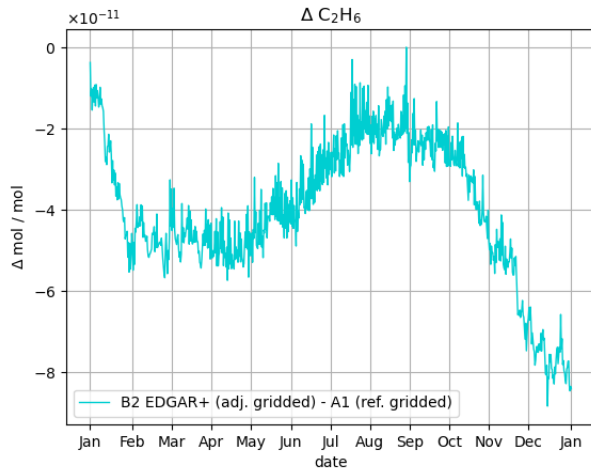
(i)
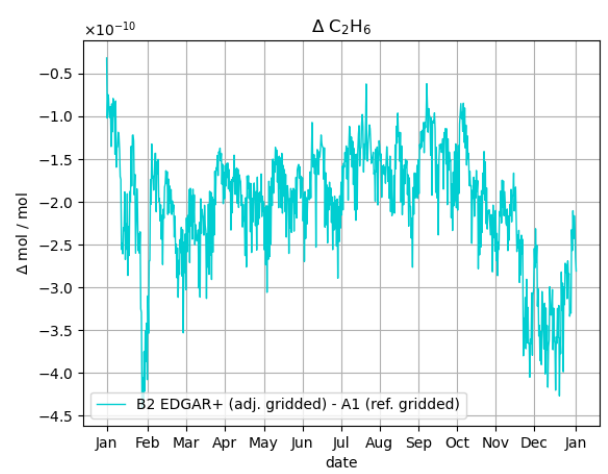
(j)
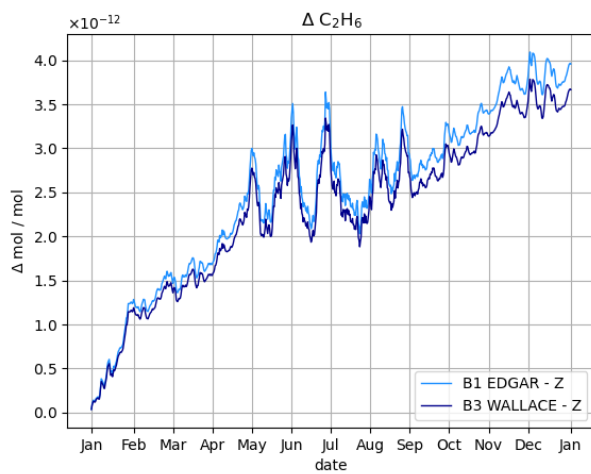
(k)
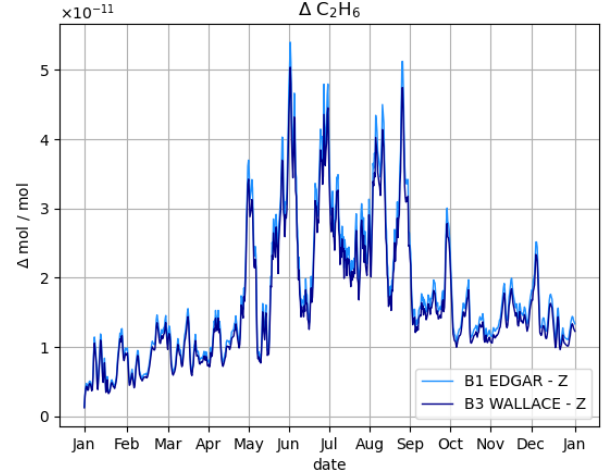
(l)

Figure E.2: Time series of C_2H_6 (... continued).

(a)

(b)

(c)

(d)

(e)

(f)
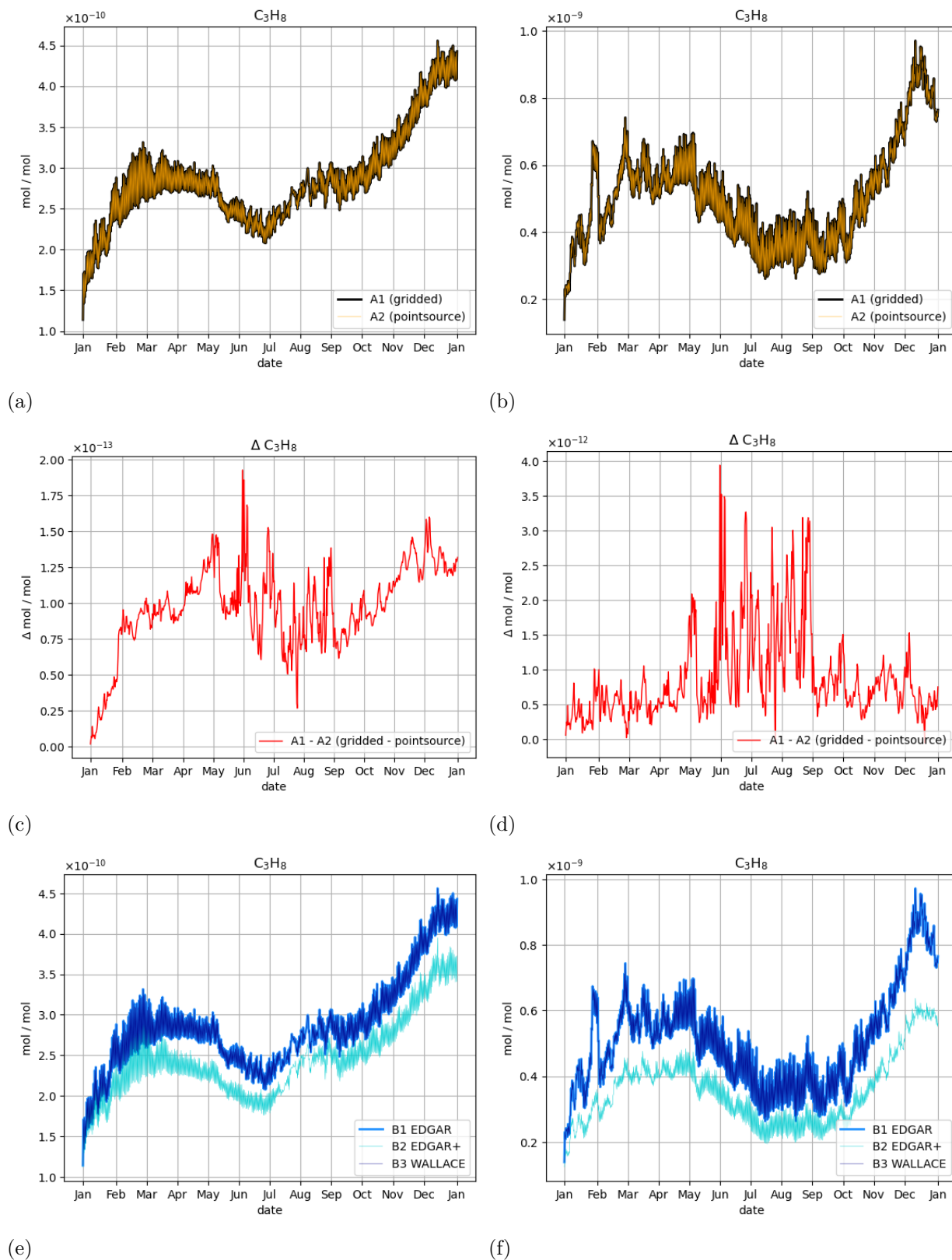
Figure E.3: Time series of C$_3$H$_8$.
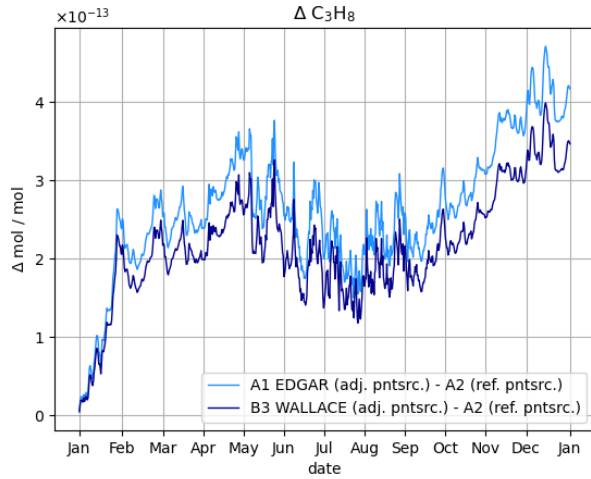
(g)
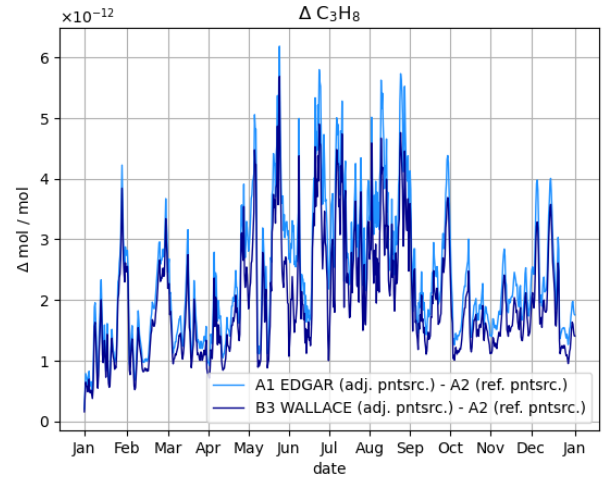
(h)
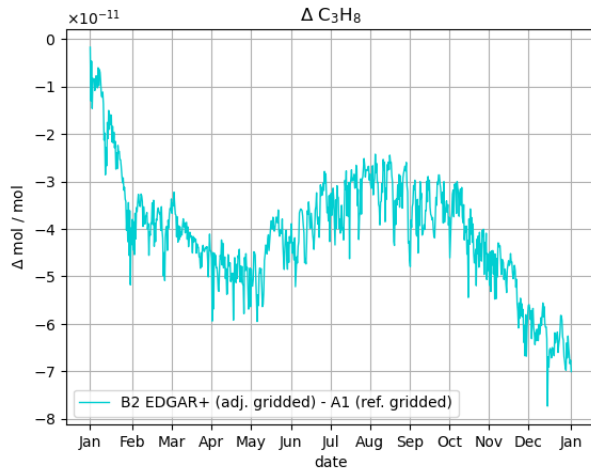
(i)
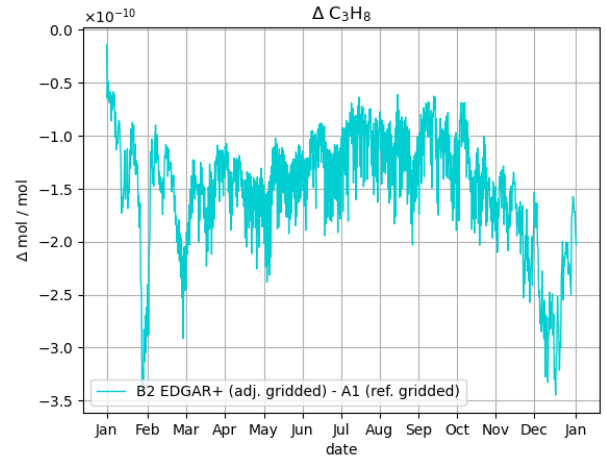
(j)
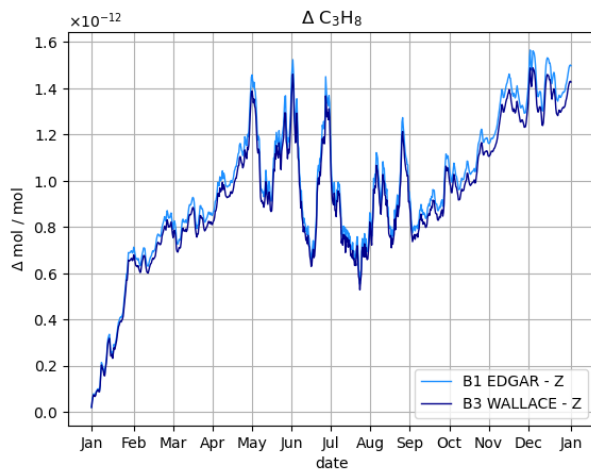
(k)
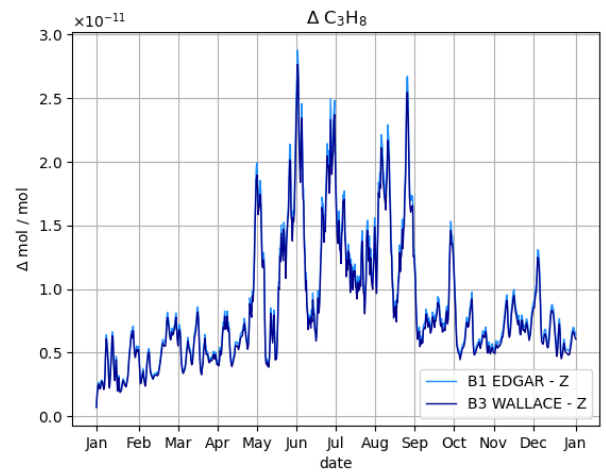
(l)

Figure E.3: Time series of C_3H_8 (... continued).

(a)

(b)

(c)

(d)

(e)

(f)
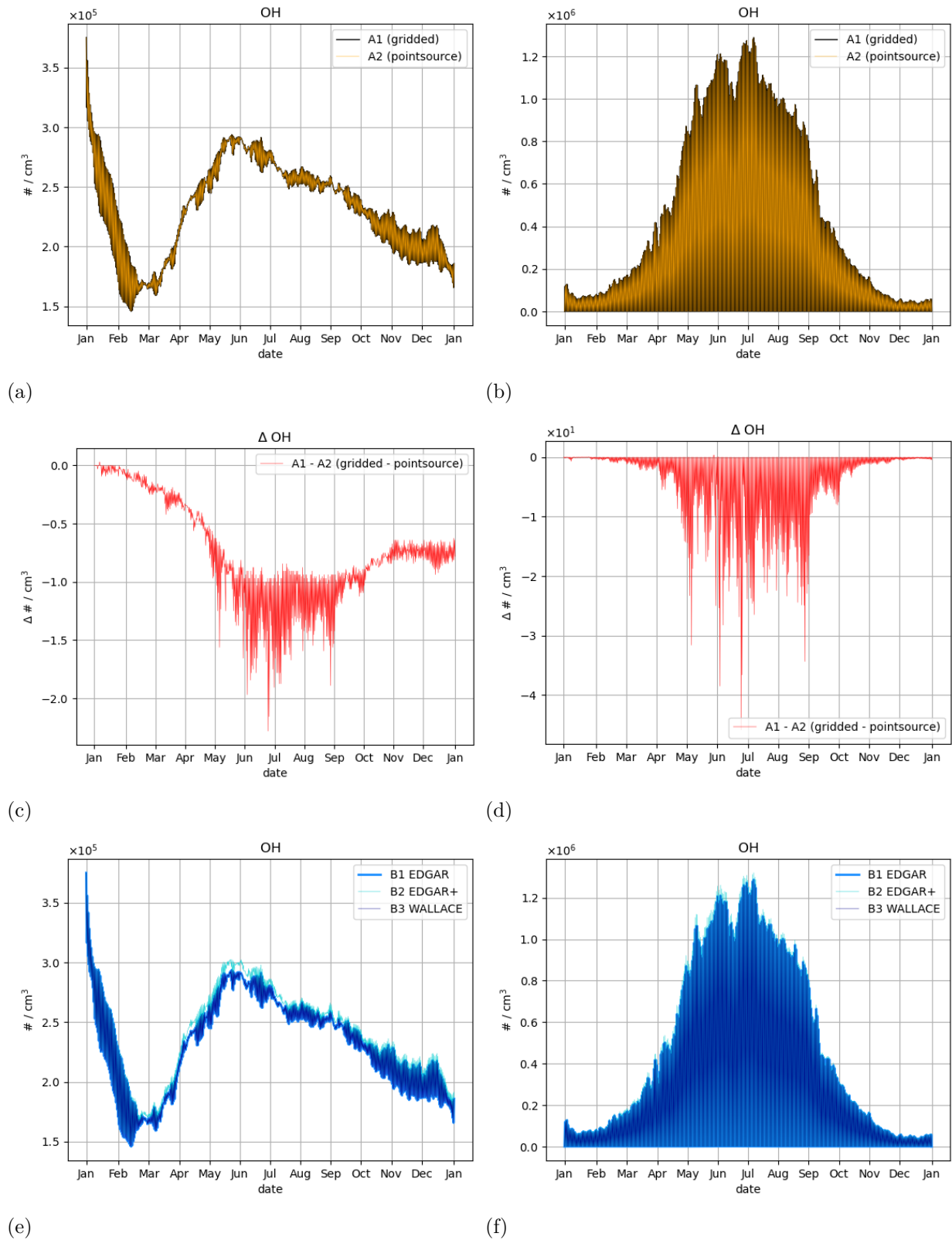
Figure E.4: Time series of OH.
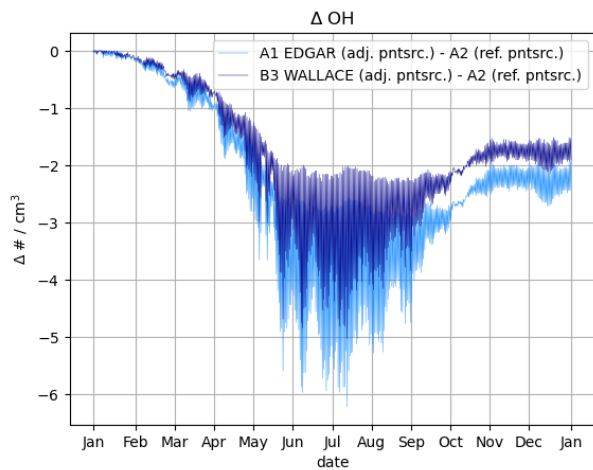
(g)
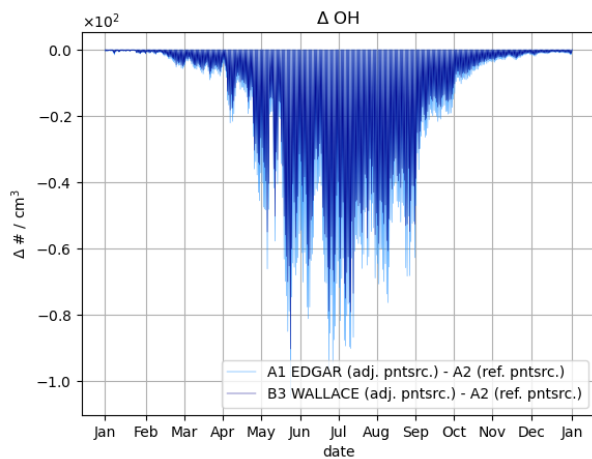
(h)
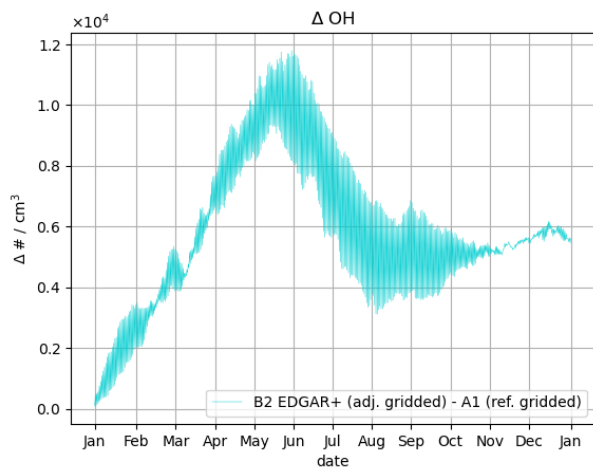
(i)
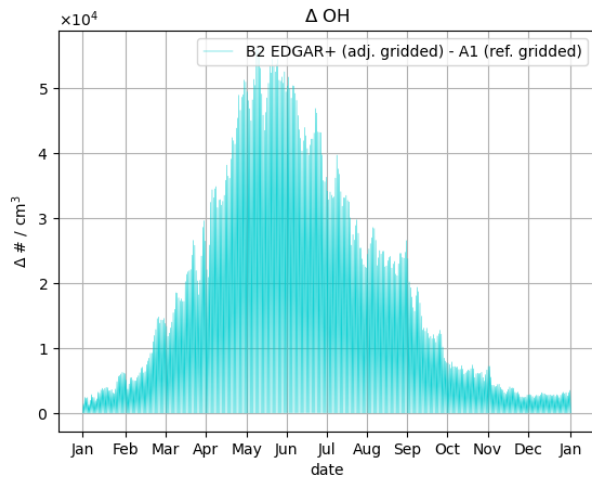
(j)
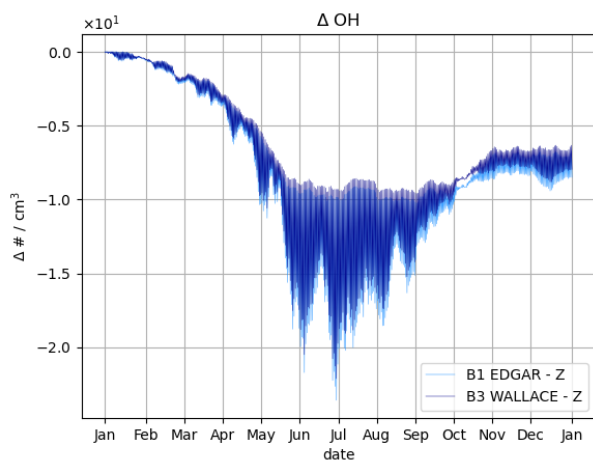
(k)
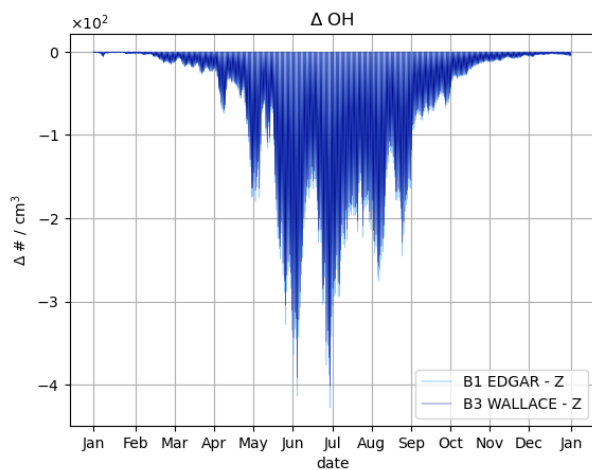
(l)

Figure E.4: Time series of OH (... continued).

Bibliography

D. L. Albritton, L. G. Meira Filho, U. Cubasch, X. Dai, Y. Ding, D. J. Griggs, B. Hewitson, J. T. Houghton, I. Isaksen, T. Karl, M. McFarland, V. P. Meleshko, J. F. B. Mitchell, M. Noguer, B. S. Nyenzi, M. Oppenheimer, J. E. Penner, S. Pollonais, T. Stocker, and K. E. Trenberth. *Climate Change 2001: The Scientific Basis. Contribution of Working Group I to the Third Assessment Report of the Intergovernmental Panel on Climate Change.* Cambridge University Press, Cambridge, United Kingdom and New York, NY, USA, 2001.

M. Alexe, P. Bergamaschi, A. Segers, R. Detmers, A. Butz, O. Hasekamp, S. Guerlet, R. Parker, H. Boesch, C. Frankenberg, R. A. Scheepmaker, E. Dlugokencky, C. Sweeney, S. C. Wofsy, and E. A. Kort. Inverse modelling of CH4 emissions for 2010–2011 using different satellite retrieval products from GOSAT and SCIAMACHY. *Atmospheric Chemistry and Physics*, 15(1):113–133, 2015. doi: 10.5194/acp-15-113-2015.

S. Arrhenius. On the influence of carbonic acid in the air upon the temperature of the ground. *Philosophical Magazine and Journal of Science*, 41(5):237–276, 1896.

A. M. P. Baede, E. Ahlonsou, Y. Ding, and D. Schimel. *Climate Change 2001: The Scientific Basis. Contribution of Working Group I to the Third Assessment Report of the Intergovernmental Panel on Climate Change*, chapter The Climate System: an Overview, pages 87–98. Cambridge University Press, Cambridge, United Kingdom and New York, NY, USA, 2001.

P. Bergamaschi, S. Houweling, A. Segers, M. Krol, C. Frankenberg, R. A. Scheepmaker, E. Dlugokencky, S. C. Wofsy, E. A. Kort, C. Sweeney, T. Schuck, C. Brenninkmeijer, H. Chen, V. Beck, and C. Gerbig. Atmospheric CH_4 in the first decade of the 21st century: Inverse modeling analysis using SCIAMACHY satellite retrievals and NOAA surface measurements. *Journal of Geophysical Research: Atmospheres*, 118(13):7350–7369, 2013. doi: 10.1002/jgrd.50480.

L. Bruhwiler, E. Dlugokencky, K. Masarie, M. Ishizawa, A. Andrews, J. Miller, C. Sweeney, P. Tans, and D. Worthy. CarbonTracker-CH_4: an assimilation system

for estimating emissions of atmospheric methane. *Atmospheric Chemistry and Physics*, 14(16):8269–8293, 2014. doi: 10.5194/acp-14-8269-2014.

C. Buchal and C.-D. Schönwiese. *Klima. Die Erde und ihre Atmosphäre im Wandel der Zeiten.* Wilhelm und Else Heraeus-Stiftung, 2016.

BVEG. Bundesverband Erdgas, Erdöl, Geoenergie - Statistischer Bericht, 2019.

J. G. Canadell, P. M. S. Monteiro, M. H. Costa, L. Cotrim da Cunha, P. M. Cox, A. V. Eliseev, S. Henson, M. Ishii, S. Jaccard, C. Koven, A. Lohila, P. K. Patra, S. Piao, J. Rogelj, S. Syampungani, S. Zaehle, and K. Zickfeld. Global Carbon and other Biogeochemical Cycles and Feedbacks. In: Climate Change 2021: The Physical Science Basis. Contribution of Working Group I to the Sixth Assessment Report of the Intergovernmental Panel on Climate Change [Masson-Delmotte, V., P. Zhai, A. Pirani, S. L. Connors, C. Péan, S. Berger, N. Caud, Y. Chen, L. Goldfarb, M. I. Gomis, M. Huang, K. Leitzell, E. Lonnoy, J. B. R. Matthews, T. K. Maycock, T. Waterfield, O. Yelekçi, R. Yu and B. Zhou (eds.)]. Technical report, Cambridge University Press. In Press., 2021.

CDIAC. Carbon Dioxide Information Analysis Center - Worldwide ethane (C_2H_6) concentrations. https://cdiac.ess-dive.lbl.gov/trends/otheratg/blake/otherhydrocarbons/ethane.html, Accessed: 2021-10-21, 2012.

D. A. Day, P. J. Wooldridge, and R. C. Cohen. Observations of the effects of temperature on atmospheric HNO_3, ANs, PNs, and NO_x: evidence for a temperature-dependent HO_x source. *Atmospheric Chemistry and Physics*, 8(6):1867–1879, 2008. doi: 10.5194/acp-8-1867-2008.

destatis. Statistisches Bundesamt - Stromverbrauch der privaten Haushalte nach Haushaltsgrößenklassen. https://www.destatis.de/DE/Themen/Gesellschaft-Umwelt/Umwelt/UGR/private-haushalte/Tabellen/stromverbrauch-haushalte.html, 07 2021. Accessed: 2021-09-30.

E. J. Dlugokencky, L. P. Steele, P. M. Lang, and K. A. Masarie. The Growth-Rate and Distribution of Atmospheric Methane. *Journal of Geophysical Research-Atmospheres, 99, 17,021-017,043*, 1994. doi: 10.1029/94JD01245.

E. J. Dlugokencky, E. G. Nisbet, R. Fisher, and D. Lowry. Global atmospheric methane: budget, changes and dangers. *Philosophical transactions of the royal society A. Mathematical, physical and engineering sciences*, 369:2058–72, 2011. doi: 10.1098/rsta.2010.0341.

E. J. Dlugokencky, P. M. Lang, A. M. Crotwell, J. W. Mund, M. J. Crotwell, and K. W. Thoning. Atmospheric Methane Dry Air Mole Fractions from the NOAA ESRL Carbon Cycle Cooperative Global Air Sampling Network, 1983-2017. ftp://aftp.cmdl.noaa.gov/data/trace_gases/ch4/flask/surface/ Accessed: 2019-06-04, 2018.

E-PRTR. REGULATION (EC) No 166/2006 OF THE EUROPEAN PARLIAMENT AND OF THE COUNCIL of 18 January 2006 concerning the establishment of a European Pollutant Release and Transfer Register and amending Council Directives 91/689/EEC and 96/61/EC. Official Journal of the European Union, 2006.

E-PRTR. European pollutant release and transfer register. https://prtr.eea.europa.eu, Accessed: 2020-06-19, 2020.

EC-JRC. European Commission - Joint Research Centre. Global Greenhouse Gases Emissions EDGAR v4.3.2. https://edgar.jrc.ec.europa.eu/overview.php?v=432_GHG, Accessed: 2020-06-19, 2020a.

EC-JRC. European Commission - Joint Research Centre. Global Greenhouse Gas Emissions EDGAR v5.0. https://edgar.jrc.ec.europa.eu/overview.php?v=50_GHG, Accessed: 2020-06-19, 2020b.

ECCAD. Emission of atmospheric Compounds and Compilation of Ancillary Data. http://eccad.aeris-data.fr, Accessed: 2018-10-17, 2018.

D. Ehhalt, M. Prather, F. Dentener, R. Derwent, E. Dlugokencky, E. Holland, I. Isaksen, J. Katima, V. Kirchhoff, P. Matson, P. Midgley, and M. Wang. *Climate Change 2001: The Scientific Basis. Contribution of Working Group I to the Third Assessment Report of the Intergovernmental Panel on Climate Change*, chapter Atmospheric Chemistry and Greenhouse Gases, pages 239–288. Cambridge University Press, Cambridge, United Kingdom and New York, NY, USA, 2001.

EPA. United States Environmental Protection Agency - Greenhouse Gas Equivalencies Calculator. https://www.epa.gov/energy/greenhouse-gas-equivalencies-calculator, 2021. Accessed: 2021-09-30.

ESA. European Space Agency - Sentinel-5P. https://sentinel.esa.int/web/sentinel/missions/sentinel-5p, Accessed: 2020-04-28, 2020.

ESA. European Space Agency - Earth observation mission logotypes. https://www.esa.int/eologos/sentinel-5p.html, 2021. Accessed: 2021-09-15.

Bibliography

Expertenrat für Klimafragen. Bericht zur Vorjahresschätzung der deutschen Treibhausgasemissionen für das Jahr 2020. https://www.expertenrat-klima.de/publikationen/, Accessed: 2021-10-04, 2021.

V. Fiedler, M. Dal Maso, M. Boy, H. Aufmhoff, J. Hoffmann, T. Schuck, W. Birmili, M. Hanke, J. Uecker, F. Arnold, and M. Kulmala. The contribution of sulphuric acid to atmospheric particle formation and growth: a comparison between boundary layers in northern and central europe. *Atmospheric Chemistry and Physics*, 5(7):1773–1785, 2005. doi: 10.5194/acp-5-1773-2005.

P. Forster, T. Strorelvmo, K. Armour, W. Collins, J.-L. Dufresne, D. Frame, D. J. Lunt, T. Mauritsen, M. D. Palmer, M. Watanabe, M. Wild, and H. Zhang. The Earth's energy budget, climate feedbacks, and climate sensitivity. In: Climate Change 2021: The Physical Science Basis. Contribution of Working Group I to the Sixth Assessment Report of the Intergovernmental Panel on Climate Change [Masson-Delmotte, V., P. Zhai, A. Pirani, S. L. Connors, C. Péan, S. Berger, N. Caud, Y. Chen, L. Goldfarb, M. I. Gomis, M. Huang, K. Leitzell, E. Lonnoy, J. B. R. Matthews, T. K. Maycock, T. Waterfield, O. Yelekçi, R. Yu and B. Zhou (eds.)]. Technical report, Cambridge University Press. In Press., 2021.

A. Gassmann and H.-J. Herzog. Towards a consistent numerical compressible non-hydrostatic model using generalized hamiltonian tools. *Quarterly Journal of the Royal Meteorological Society*, 134:1597 – 1613, 2008. doi: 10.1002/qj.297.

GCP. Global Carbon Project. http://www.globalcarbonproject.org/, Accessed: 2018-10-18, 2016.

E. Glueckauf. *The Composition of Atmospheric Air*, chapter Compendium of Meteorology. American Meteorological Society, Boston., 1951.

S. Grimm. Umweltbundesamt, personal communication, 2020.

G. D. Hayman, F. M. O'Connor, M. Dalvi, D. B. Clark, N. Gedney, C. Huntingford, C. Prigent, M. Buchwitz, O. Schneising, J. P. Burrows, C. Wilson, N. Richards, and M. Chipperfield. Comparison of the HadGEM2 climate-chemistry model against in situ and SCIAMACHY atmospheric methane data. *Atmospheric Chemistry and Physics*, 14(23):13257–13280, 2014. doi: 10.5194/acp-14-13257-2014.

N. Henze. *Stochastik für Einsteiger. Eine Einführung in die faszinierende Welt des Zufalls.* Springer, 11. auflage edition, 2017. doi: 10.1007/978-3-658-14739-6.

B. Hmiel, V. V. Petrenko, M. N. Dyonisius, C. Buizert, A. M. Smith, P. F. Place, C. Harth, R. Beaudette, Q. Hua, B. Yang, I. Vimont, S. E. Michel, J. P. Severinghaus, D. Etheridge, T. Bromley, J. Schmitt, X. Faïn, R. F. Weiss, and E. Dlugokencky.

Preindustrial $^{14}CH_4$ indicates greater anthropogenic fossil CH_4 emissions. *Nature*, 578 (7795):409 – 412, 2020. ISSN 1476 - 4687. doi: 10.1038/s41586-020-1991-8.

Ø. Hodnebrog, S. B. Dalsøren, and G. Myhre. Lifetimes, direct and indirect radiative forcing, and global warming potentials of ethane (C_2H_6), propane (C_3H_8), and butane (C_4H_{10}). *Atmospheric Science Letters*, 19(2):e804, 2018. doi: 10.1002/asl.804.

R. M. Hoesly, S. J. Smith, L. Feng, Z. Klimont, G. Janssens-Maenhout, T. Pitkanen, J. J. Seibert, L. Vu, R. J. Andres, R. M. Bolt, T. C. Bond, L. Dawidowski, N. Kholod, J.-I. Kurokawa, M. Li, L. Liu, Z. Lu, M. C. P. Moura, P. R. O'Rourke, and Q. Zhang. Historical (1750-2014) anthropogenic emissions of reactive gases and aerosols from the Community Emissions Data System (CEDS). *Geoscientific Model Development*, 11(1): 369–408, 2018. doi: 10.5194/gmd-11-369-2018.

L. Höglund-Isaksson. Global anthropogenic methane emissions 2005-2030: technical mitigation potentials and costs. *Atmospheric Chemistry and Physics*, 12(19):9079–9096, 2012. doi: 10.5194/acp-12-9079-2012.

S. Houweling, M. Krol, P. Bergamaschi, C. Frankenberg, E. J. Dlugokencky, I. Morino, J. Notholt, V. Sherlock, D. Wunch, V. Beck, C. Gerbig, H. Chen, E. A. Kort, T. Röckmann, and I. Aben. A multi-year methane inversion using SCIAMACHY, accounting for systematic errors using TCCON measurements. *Atmospheric Chemistry and Physics*, 14(8):3991–4012, 2014. doi: 10.5194/acp-14-3991-2014.

IPCC. Intergovernmental Panel on Climate Change - Climate Change: The IPCC Scientific Assessment 1990. Report prepared for Intergovernmental Panel on Climate Change by Working Group I – First Assessment Report, edited by J. T. Houghton, G. J. Jenkins and J. J. Ephraums. Technical report, Cambridge, 1990.

IPCC. Intergovernmental Panel on Climate Change - Climate Change 2014: Synthesis Report. Contribution of Working Groups I, II and III to the Fifth Assessment Report of the Intergovernmental Panel on Climate Change [Core Writing Team, R.K. Pachauri and L.A. Meyer (eds.)]. Technical report, IPCC, Geneva, Switzerland, 151 pp., 2014.

IPCC. Intergovernmental Panel on Climate Change - Summary for Policymakers. In: Climate Change 2021: The Physical Science Basis. Contribution of Working Group I to the Sixth Assessment Report of the Intergovernmental Panel on Climate Change [Masson-Delmotte, V., P. Zhai, A. Pirani, S. L. Connors, C. Péan, S. Berger, N. Caud, Y. Chen, L. Goldfarb, M. I. Gomis, M. Huang, K. Leitzell, E. Lonnoy, J. B. R. Matthews, T. K. Maycock, T. Waterfield, O. Yelekçi, R. Yu and B. Zhou (eds.)]. Technical report, Cambridge University Press. In Press., 2021.

M. Ishizawa, K. Mabuchi, T. Shirai, M. Inoue, I. Morino, O. Uchino, Y. Yoshida, D. Belikov, and S. Maksyutov. Inter-annual variability of summertime CO_2 exchange in Northern Eurasia inferred from GOSAT XCO_2. *Environmental Research Letters*, 11 (10):105001, 2016. doi: 10.1088/1748-9326/11/10/105001.

D. J. Jacob. *Introduction to atmospheric chemistry, 1st edn.* Princeton University Press, Priceton, NJ, USA, 1999.

M. Z. Jacobson. *Fundamentals of Atmospheric Modeling. Second Edition.* Cambridge University Press, 2005.

G. Janssens-Maenhout, V. Pagliari, D. Guizzardi, and M. Muntean. *Global emission inventories in the Emission Database for Global Atmospheric Research (EDGAR) Manual (I) Gridding: EDGAR emissions distribution on global gridmaps.* European Commission - Joint Research Centre - Institute for Environment and Sustainability, 2012.

G. Janssens-Maenhout, M. Crippa, D. Guizzardi, M. Muntean, E. Schaaf, F. Dentener, P. Bergamaschi, V. Pagliari, J. G. J. Olivier, J. A. H. W. Peters, J. A. van Aardenne, S. Monni, U. Doering, A. M. R. Petrescu, E. Solazzo, and G. D. Oreggioni. EDGAR v4.3.2 Global Atlas of the three major greenhouse gas emissions for the period 1970–2012. *Earth System Science Data*, 11(3):959 – 1002, 2019. doi: 10.5194/essd-11-959-2019.

C. A. Keller, M. S. Long, R. M. Yantosca, A. M. Da Silva, S. Pawson, and D. J. Jacob. Hemco v1.0: a versatile, esmf-compliant component for calculating emissions in atmospheric models. *Geoscientific Model Development*, 7(4):1409 – 1417, 2014. doi: 10.5194/gmd-7-1409-2014.

M. A. K. Khalil. *Atmospheric Methane - Its Role in the Global Environment.* Springer, 2000.

S. Kirschke, P. Bousquet, P. Ciais, M. Saunois, J. G. Canadell, E. J. Dlugokencky, P. Bergamaschi, D. Bergmann, D. R. Blake, L. Bruhwiler, P. Cameron-Smith, S. Castaldi, F. Chevallier, L. Feng, A. Fraser, M. Heimann, E. L. Hodson, S. Houweling, B. Josse, P. J. Fraser, P. B. Krummel, J.-F. Lamarque, R. L. Langenfelds, C. Le Quéré, V. Naik, S. O'Doherty, P. I. Palmer, I. Pison, D. Plummer, B. Poulter, R. G. Prinn, M. Rigby, B. Ringeval, M. Santini, M. Schmidt, D. T. Shindell, I. J. Simpson, R. Spahni, L. P. Steele, S. A. Strode, K. Sudo, S. Szopa, G. R. van der Werf, A. Voulgarakis, M. van Weele, R. F. Weiss, J. E. Williams, and G. Zeng. Three decades of global methane sources and sinks. *Nature Geoscience*, 6:813–823, 2013. doi: 10.1038/NGEO1955.

H. J. Kramer. Copernicus: Sentinel-5P (Precursor - Atmospheric Monitoring Mission). https://directory.eoportal.org/web/eoportal/satellite-missions/c-missions/copernicus-sentinel-5p, Accessed: 2020-04-28, 2020.

M. Liu, R. van der A, M. van Weele, H. Eskes, X. Lu, P. Veefkind, J. de Laat, H. Kong, J. Wang, J. Sun, J. Ding, Y. Zhao, and H. Weng. A new divergence method to quantify methane emissions using observations of Sentinel-5P TROPOMI. *Geophysical Research Letters*, 48, 2021. doi: 10.1029/2021GL094151.

S. A. McKeen, E.-Y. Hsie, M. Trainer, R. Tallamraju, and S. C. Liu. A regional model study of the ozone budget in the eastern United States. *Journal of Geophysical Research Atmospheres*, 96(D6):10809 − 10845, 1991.

C. A. McLinden, S. C. Olsen, B. Hannegan, O. Wild, M. J. Prather, and J. Sundet. Stratospheric ozone in 3-D models: A simple chemistry and the cross-tropopause flux. *Journal of Geophysical Research Atmospheres*, 105(D11):14653 − 14665, 2000.

M. V. Migeotte. Spectroscopic Evidence of Methane in the Earth's Atmosphere. *Phys. Rev.*, 73:519–520, 1948. doi: 10.1103/PhysRev.73.519.2.

M. Muser, D. Rieger, and B. Vogel. *ICON-ART User Guide*. Karlsruhe Institute of Technology, Institute for Meteorology and Climate Research (IMK-TRO), 2018.

D. Nicholls, F. Barnes, F. Acrea, C. Chen, L. Y. Buluc, and M. M. Parker. Top-down and bottom-up approaches to greenhouse gas inventory methods. Technical report, United States Department of Agriculture, 2015.

E. G. Nisbet, M. R. Manning, E. J. Dlugokencky, R. E. Fisher, D. Lowry, S. E. Michel, C. Lund Myhre, S. M. Platt, G. Allen, P. Bousquet, R. Brownlow, M. Cain, J. L. France, O. Hermansen, R. Hossaini, A. E. Jones, I. Levin, A. C. Manning, G. Myhre, J. A. Pyle, B. H. Vaughn, N. J. Warwick, and J. W. C. White. Very Strong Atmospheric Methane Growth in the 4 Years 2014–2017: Implications for the Paris Agreement. *Global Biochemical Cycles*, 33:318–342, 2019. doi: https://doi.org/10.1029/2018GB006009.

NOAA. National Oceanic and Atmospheric Administration - Earth System Research Laboratory - Global Monitoring Division - Observation Sites. https://www.esrl.noaa.gov/gmd/dv/site/, Accessed: 2019-07-16, 2019.

OSPAR. Inventory of Offshore Installations 2017. https://odims.ospar.org, Accessed: 2019-01-24, 2017.

OSPAR. Discharges, Spills and Emissions from Offshore Oil and Gas Installations. https://odims.ospar.org, Accessed: 2021-07-29, 2019.

P. K. Patra, T. Saeki, E J. Dlugokencky, K. Ishijimai, T. Umezawa, A. Ito, S. Aoki, S. Morimoto, E. A. Kort, A. Crotwell, K. Ravi Kumar, and T. Nakazawa. Regional Methane Emission Estimation Based on Observed Atmospheric Concentrations (2002-2012). *Journal of the Meteorological Society of Japan. Ser. II*, 94(1):91–113, 2016. doi: 10.2151/jmsj.2016-006.

V. V. Petrenko, A. M. Smith, H. Schaefer, K. Riedel, E. Brook, D. Baggenstos, C. Harth, Q. Hua, C. Buizert, A. Schilt, X. Fain, L. Mitchell, T. Bauska, A. Orsi, R. F. Weiss, and J. P. Severinghaus. Minimal geological methane emissions during the younger dryas-preboreal abrupt warming event. *Nature*, 548(7668):443 – 446, 2017. ISSN 1476 - 4687. doi: 10.1038/nature23316.

R. W. Pinder, A. B. Gilliland, and R. L. Dennis. Environmental impact of atmospheric NH_3 emissions under present and future conditions in the eastern United States. *Geophysical Research Letters*, 35, 2008. doi: 10.1029/2008GL033732.

I. Pison, B. Ringeval, P. Bousquet, C. Prigent, and F. Papa. Stable atmospheric methane in the 2000s: key-role of emissions from natural wetlands. *Atmospheric Chemistry and Physics*, 13(23):11609–11623, 2013. doi: 10.5194/acp-13-11609-2013.

M. Ponater, S. Dietmüller, and R. Sausen. *Atmospheric Physics. Background - Method - Trends*, chapter Greenhouse Effect, Radiative Forcing and Climate Sensitivity, pages 85–99. Springer, Berlin, Heidelberg, 2012.

A. Pozzer, J. Pollmann, D. Taraborrelli, P. Jöckel, D. Helmig, P. Tans, J. Hueber, and J. Lelieveld. Observed and simulated global distribution and budget of atmospheric C_2-C_5 alkanes. *Atmospheric Chemistry and Physics*, 10(9):4403–4422, 2010. doi: 10.5194/acp-10-4403-2010.

M. J. Prather. Photolysis rates in correlated overlapping cloud fields: Cloud-J 7.3c. *Geoscientific Model Development*, 8(8):2587 – 2595, 2015. doi: 10.5194/gmd-8-2587-2015.

F. Prill, D. Reiner, D. Rieger, G. Zängl, J. Schröter, J. Förstner, S. Werchner, M. Weimer, R. Ruhnke, and B. Vogel. *ICON Model Tutorial. Working with the ICON Model, Practical Exercises for NWP Mode and ICON-ART*. Deutscher Wetterdienst, Karlsruhe Institute of Technology, Max-Planck-Institut für Meteorologie, 2019.

S. Raffeiner. Steinbuch Centre for Computing, personal communication, 2021.

V. Ramaswamy, O. Boucher, J. Haigh, D. Hauglustaine, J. Haywood, G. Myhre, T. Nakajima, G. Y. Shi, and S. Solomon. *Climate Change 2001: The Scientific Basis. Contribution of Working Group I to the Third Assessment Report of the Intergovernmental*

Panel on Climate Change, chapter Radiative Forcing of Climate Change, pages 349–416. Cambridge University Press, Cambridge, United Kingdom and New York, NY, USA, 2001.

S. N. Riddick, D. L. Mauzerall, M. Celia, N. R. P. Harris, G. Allen, J. Pitt, J. Staunton-Sykes, G. L. Forster, M. Kang, D. Lowry, E. G. Nisbet, and A. J. Manning. Methane emissions from oil and gas platforms in the North Sea. *Atmospheric Chemistry and Physics*, 19(15):9787–9796, 2019. doi: 10.5194/acp-19-9787-2019.

D. Rieger, M. Bangert, I. Bischoff-Gauss, J. Förstner, K. Lundgren, D. Reinert, J. Schröter, H. Vogel, G. Zängl, R. Ruhnke, and B. Vogel. ICON–ART 1.0 – a new online-coupled model system from the global to regional scale. *Geoscientific Model Development*, 8(6):1659–1676, 2015. doi: 10.5194/gmd-8-1659-2015.

W. Roedel. *Physik unserer Umwelt. Die Atmosphäre*. Springer, Berlin, Heidelberg, 1992.

R. Sadourny, A. Arakawa, and Y. Mintz. Integration of the nondivergent barotropic vorticity equation with an icosahedral-hexagonal grid for the sphere. *Monthly Weather Review*, 96(6):351 – 356, 1968.

S. P. Sander, J. Abbatt, J. Barker, J. B. Burkholder, R. R. Friedl, D. M. Golden, R. Huie, M. Kurylo, G. Moortgat, V. Orkin, and P. Wine. Chemical Kinetics and Photochemical Data for Use in Atmospheric Studies, Evaluation No. 17. Technical report, National Aeronautics and Space Administration, Jet Propulsion Laboratory, 2011.

M. Saunois, P. Bousquet, B. Poulter, A. Peregon, P. Ciais, J. G. Canadell, E. J. Dlugokencky, G. Etiope, D. Bastviken, S. Houweling, G. Janssens-Maenhout, F. N. Tubiello, S. Castaldi, R. B. Jackson, M. Alexe, V. K. Arora, D. J. Beerling, P. Bergamaschi, D. R. Blake, G. Brailsford, V. Brovkin, L. Bruhwiler, C. Crevoisier, P. Crill, K. Covey, C. Curry, C. Frankenberg, N. Gedney, L. Höglund-Isaksson, M. Ishizawa, A. Ito, F. Joos, H.-S. Kim, T. Kleinen, P. Krummel, J.-F. Lamarque, R. Langenfelds, R. Locatelli, T. Machida, S. Maksyutov, K. C. McDonald, J. Marshall, J. R. Melton, I. Morino, V. Naik, S. O'Doherty, F.-J. W. Parmentier, P. K. Patra, C. Peng, S. Peng, G. P. Peters, I. Pison, C. Prigent, R. Prinn, M. Ramonet, W. J. Riley, M. Saito, M. Santini, R. Schroeder, I. J. Simpson, R. Spahni, P. Steele, A. Takizawa, B. F. Thornton, H. Tian, Y. Tohjima, N. Viovy, A. Voulgarakis, M. van Weele, G. R. van der Werf, R. Weiss, C. Wiedinmyer, D. J. Wilton, A. Wiltshire, D. Worthy, D. Wunch, X. Xu, Y. Yoshida, B. Zhang, Z. Zhang, and Q. Zhu. The global methane budget 2000–2012. *Earth System Science Data, 8, 697–751*, 2016a. doi: 10.5194/essd-8-697-2016.

M. Saunois, R. B. Jackson, P. Bousquet, B. Poulter, and J. G. Canadell. The growing role of methane in anthropogenic climate change. *Environmental Research Letters 11 120207*, b 2016b. doi: 10.1088/1748-9326/11/12/120207.

M. Saunois, A. R. Stavert, B. Poulter, P. Bousquet, J. G. Canadell, R. B. Jackson, P. A. Raymond, E. J. Dlugokencky, S. Houweling, P. K. Patra, P. Ciais, V. K. Arora, D. Bastviken, P. Bergamaschi, D. R. Blake, G. Brailsford, L. Bruhwiler, K. M. Carlson, M. Carrol, S. Castaldi, N. Chandra, C. Crevoisier, P. M. Crill, K. Covey, C. L. Curry, G. Etiope, C. Frankenberg, N. Gedney, M. I. Hegglin, L. Höglund-Isaksson, G. Hugelius, M. Ishizawa, A. Ito, G. Janssens-Maenhout, K. M. Jensen, F. Joos, T. Kleinen, P. B. Krummel, R. L. Langenfelds, G. G. Laruelle, L. Liu, T. Machida, S. Maksyutov, K. C. McDonald, J. McNorton, P. A. Miller, J. R. Melton, I. Morino, J. Müller, F. Murguia-Flores, V. Naik, Y. Niwa, S. Noce, S. O'Doherty, R. J. Parker, C. Peng, S. Peng, G. P. Peters, C. Prigent, R. Prinn, M. Ramonet, P. Regnier, W. J. Riley, J. A. Rosentreter, A. Segers, I. J. Simpson, H. Shi, S. J. Smith, L. P. Steele, B. F. Thornton, H. Tian, Y. Tohjima, F. N. Tubiello, A. Tsuruta, N. Viovy, A. Voulgarakis, T. S. Weber, M. van Weele, G. R. van der Werf, R. F. Weiss, D. Worthy, D. Wunch, Y. Yin, Y. Yoshida, W. Zhang, Z. Zhang, Y. Zhao, B. Zheng, Q. Zhu, Q. Zhu, and Q. Zhuang. The global methane budget 2000–2017. *Earth System Science Data*, 12(3):1561 – 1623, 2020. doi: 10.5194/essd-12-1561-2020.

T. R. Scarpelli, D. J. Jacob, J. D. Maasakkers, M. P. Sulprizio, J.-X. Sheng, K. Rose, L. Romeo, J. R. Worden, and G. Janssens-Maenhout. A global gridded (0.1° × 0.1°) inventory of methane emissions from oil, gas, and coal exploitation based on national reports to the United Nations Framework Convention on Climate Change. *Earth System Science Data*, 12(1):563–575, 2020. doi: 10.5194/essd-12-563-2020.

J. Schröter, D. Rieger, C. Stassen, H. Vogel, M. Weimer, S. Werchner, J. Förstner, F. Prill, D. Reinert, G. Zängl, M. Giorgetta, R. Ruhnke, B. Vogel, and P. Braesicke. ICON-ART 2.1: a flexible tracer framework and its application for composition studies in numerical weather forecasting and climate simulations. *Geoscientific Model Development*, 11(10): 4043 – 4068, 2018. doi: 10.5194/gmd-11-4043-2018.

U. Schulzweida. CDO User Guide (Version 1.9.8). 10.5281/zenodo.3539275, 2019.

S. Schwietzke, O. A. Sherwood, L. M. P. Bruhwiler, J. B. Miller, G. Etiope, E. J. Dlugokencky, S. E. Michel, V. A. Arling, B. H. Vaughn, J. W. C. White, and P. P. Tans. Upward revision of global fossil fuel methane emissions based on isotope database. *Nature*, 538(7623):88 – 91, 2016. ISSN 1476 - 4687. doi: 10.1038/nature19797.

C.-D. Schönwiese. *Klimatologie. Grundlagen, Entwicklungen und Perspektiven.* Verlag Eurgen Ulmer, Stuttgart, 2020.

J. H. Seinfeld and S. N. Pandis. *Atmospheric Chemistry and Physics: From Air Pollution to Climate Change.* Wiley, 2006.

E. Solazzo, M. Crippa, D. Guizzardi, M. Muntean, M. Choulga, and G. Janssens-Maenhout. Uncertainties in the Emissions Database for Global Atmospheric Research (EDGAR) emission inventory of greenhouse gases. *Atmospheric Chemistry and Physics*, 21(7):5655–5683, 2021. doi: 10.5194/acp-21-5655-2021.

Serco Italia SPA. *Air Quality Monitoring with Sentinel-5p (version 1.1).* Research and User Support for Sentinel Core Products, 2019.

A. Staniforth and J. Thuburn. Horizontal grids for global weather and climate prediction models: a review. *Quarterly Journal of the Royal Meteorological Society*, 138(662):1 – 26, 2012. doi: https://doi.org/10.1002/qj.958.

M. Strogies and P. Gniffke. Nationaler Inventarbericht zum Deutschen Treibhausgasinventar 1990–2016. *Berichterstattung unter der Klimarahmenkonvention der Vereinten Nationen und dem Kyoto-Protokoll 2018*, 2018.

M. Strogies and P. Gniffke. National Inventory Report for the German Greenhouse Gas Inventory 1990–2018. *Submission under the United Nations Framework Convention on Climate Change and the Kyoto Protocol 2020*, 2020.

P. Tans, J. Shakun, G. Dutton, and E. Dlugokencky. Methanelevels. https://www.methanelevels.org/, 2021. Accessed: 2021-09-30.

The Nobel Prize. https://www.nobelprize.org/prizes/physics/2021/summary/, Accessed: 2021-10-05, 2021.

THRU. Deutsches Pollutant Release and Transfer Register. https://www.thru.de, Accessed: 2020-06-19, 2020.

K. Todd. Global Land Mask. https://github.com/toddkarin/global-land-mask, Accessed: 2021-04-14, 2020.

Q. Tu, F. Hase, M. Schneider, O. García, T. Blumenstock, T. Borsdorff, M. Frey, F. Khosrawi, A. Lorente, C. Alberti, J. J. Bustos, A. Butz, V. Carreño, E. Cuevas, R. Curcoll, C. J. Diekmann, D. Dubravica, B. Ertl, C. Estruch, S. F. León-Luis, C. Marrero, J.-A. Morgui, R. Ramos, C. Scharun, C. Schneider, E. Sepúlveda, C. Toledano, and C. Torres. Quantification of CH_4 emissions from waste disposal sites near the city of Madrid using ground- and space-based observations of COCCON, TROPOMI and IASI. *Atmospheric Chemistry and Physics Discussions*, 2021:1–36, 2021. doi: 10.5194/acp-2021-437.

Bibliography

UBA. Umweltbundesamt - Wie funktioniert die Berichterstattung? https://www.umweltbundesamt.de/themen/klima-energie/klimaschutz-energiepolitik-in-deutschland/treibhausgas-emissionen/wie-funktioniert-die-berichterstattung Accessed: 2020-01-11, 2019.

UNFCCC. United Nations Framework Convention on Climate Change. http://unfccc.int/files/essential_background/background_publications_htmlpdf /application/pdf/conveng.pdf, Accessed: 09.10.2021, 1992.

UNFCCC. United Nations Framework Convention on Climate Change - National Inventory Submissions 2020. https://unfccc.int/ghg-inventories-annex-i-parties/2020, Accessed: 2020-06-17, 2020.

USEPA. Global anthropogenic non-CO_2 greenhouse gas emissions: 1990-2020. *United States Environmental Protection Agency, Washington, D.C., USA*, 2006.

M. van Damme, L. Clarisse, S. Whitburn, J. Hadji-Lazaro, D. Hurtmans, C. Clerbaux, and P.-F. Coheur. Industrial and agricultural ammonia point sources exposed. *Nature*, 564(7734):99–103, 2018. doi: 10.1038/s41586-018-0747-1.

R. Van Dingenen, M. Crippa, G. Maenhout, D. Guizzardi, and F. Dentener. Global trends of methane emissions and their impacts on ozone concentrations. Technical report, Publications Office of the European Union, Luxembourg, 2018.

R. von Glasow, N Bobrowski, and C. Kern. The effects of volcanic eruptions on atmospheric chemistry. *Chemical Geology*, 263(1):131 – 142, 2009. ISSN 0009-2541. doi: https://doi.org/10.1016/j.chemgeo.2008.08.020.

W3C. Extensible Markup Language (XML) 1.0 (Fifth Edition). https://www.w3.org/TR/2008/REC-xml-20081126/. Accessed: 2021-08-10.

J. Wegner. Dataprocessing. Manipulation & visualisation of NetCDF files. https://www.dkrz.de/mms/pdf/klimaforschung/cmip5/Processing_Joerg_Wegner.pdf, 2012. Accessed: 2021-09-15.

M. Weimer. Simulation of volatile organic compounds with ICON-ART. Master's thesis, Karlsruhe Institute of Technology, 2015.

M. Weimer. *Towards Seamless Simulation of Polar Stratospheric Clouds and Ozone in the Polar Stratosphere with ICON-ART*. PhD thesis, Karlsruhe Institute of Technology, 2019.

M. Weimer, J. Schröter, J. Eckstein, K. Deetz, M. Neumaier, G. Fischbeck, L. Hu, D. B. Millet, D. Rieger, H. Vogel, B. Vogel, T. Reddmann, O. Kirner, R. Ruhnke,

and P. Braesicke. An emission module for ICON-ART 2.0: implementation and simulations of acetone. *Geoscientific Model Development*, 10(6):2471–2494, 2017. doi: 10.5194/gmd-10-2471-2017.

WHO. *World Health Organization. Regional Office for Europe - Air quality guidelines for Europe, 2nd ed.* 2000.

G. Wypych. Microscopic mechanisms of demage caused by degradants. In George Wypych, editor, *Atlas of Material Damage (Second Edition)*, pages 113 – 305. ChemTec Publishing, second edition edition, 2017. doi: https://doi.org/10.1016/B978-1-927885-25-3.50007-0.

R. V. Zhuravlev, A. V. Ganshin, Sh. Sh. Maksyutov, S. L. Oshchepkov, and B. V. Khattatov. Estimation of global CO_2 fluxes using ground-based and satellite (GOSAT) observation data with empirical orthogonal functions. *Atmospheric and Oceanic Optics*, 26(6):507–516, Nov 2013. ISSN 2070-0393. doi: 10.1134/S1024856013060158.

G. Zängl, D. Reinert, P. Ripodas, and M. Baldauf. The ICON (ICOsahedral Nonhydrostatic) modelling framework of DWD and MPI-M: Description of the nonhydrostatic dynamical core. *Quarterly Journal of the Royal Meteorological Society*, 141(687):563–579, 2015. doi: https://doi.org/10.1002/qj.2378.

List of Figures

List of Tables

List of Acronyms

ANT	Anthropogenic Emissions
AR6	Sixth Assessment Report of the Intergovernmental Panel on Climate Change
BBE	Biomass Burning Emissions
BIO	Biogenic Emissions
BMEL	Bundesministerium für Ernährung und Landwirtschaft
BMF	Bundesministerium der Finanzen
BMI	Bundesministerium des Inneren, für Bau und Heimat
BMU	Bundesministerium für Umwelt, Naturschutz und nukleare Sicherheit
BMVg	Bundesministerium der Verteidigung
BMVI	Bundesministerium für Verkehr und digitale Infrastruktur
BMWi	Bundesministerium für Wirtschaft und Energie
BU	Bottom-Up approach
BVEG	Bundesverband Erdgas, Erdöl und Geoenergie e.V.
CDO	Climate Data Operators
CRS	Sector for aviation cruise
ECCAD	Emissions of atmospheric Compounds and Compilation of Ancillary Data
EDGAR	Emission Database for Global Atmospheric Research

EPA	United States Environmental Protection Agency
ESA	European Space Agency
EC-JRC	European Commision - Joint Research Centre
ForHLR II	Forschungshochleistungsrechner II
GAINS	Greenhose gas and Air pollutant Interactions and Synergies
GCP	Global Carbon Project
GHG	Greenhouse gas
HorKa	Hochleistungsrechner Karlsruhe
HPC	High Performance Computing
ICON-ART	Icosahedral Non-hydrostatic model - Aerosols and Reactive Trace gases
IIASA	International Institute for Applied System Analysis
IFS	Integrated Forecast System
IPCC	Intergovernmental Panel on Climate Change
KIT	Karlsruhe Institute of Technology
LINOZ	Linearized ozone
MMR	Mass Mixing Ratio
NOAA	National Oceanic and Atmospheric Administration
NSC	Nation-specific coefficients
NSO	Netherlands Space Office
NSR	North Sea Region
OECD	Organisation for Economic Co-operation and Development
OSPAR	Oslo-Paris commission
PRO	Sector for fuel exploitation

PRTR	Pollutant Release and Transfer Register
RCP	Representative Concentration Pathways
S5P	Sentinel-5 Precursor
SCC	Steinbuch Centre for Computing
SCIAMACHY	Scanning Imaging Absorption Spectrometer for Atmospheric Chartography
SHIP	Sector for shipping
TD	Top-Down approach
TROPOMI	Tropospheric measurement instrument
UBA	Umweltbundesamt
UN	United Nations
UNFCCC	United Nations Framework Convention on Climate Change
USEPA	United States Environmental Protection Agency
UTLS	Upper Troposphere Lower Stratosphere
VMR	Volume Mixing Ratio
WALLACE	Workflow for the Adjustment of Low Level Atmospheric Compounds and Emissions

Acknowledgements